Theoretical Analysis of the Interaction between Semiconductor Nanostructures and Quantum Light: From Single Pulses to Four-Wave Mixing

Dissertation

zur
Erlangung des Doktorgrades
der Naturwissenschaften
(Dr. rer. nat.)

der

Naturwissenschaftlichen Fakultät
der Universität Paderborn
vorgelegt von

Hendrik Rose

Paderborn, July 28, 2022

Erklärung der Selbstständigkeit

Hiermit versichere ich, die vorliegende Arbeit selbstständig verfasst und keine anderen als die angegebenen Quellen und Hilfsmittel benutzt sowie die Zitate deutlich kenntlich gemacht zu haben.

Ort, Datum	Unterschrift

Vorsitzender der Promotionskommission:	Prof. Dr. Tim Bartley
Erstgutachter:	Prof. Dr. Torsten Meier
Zweitgutachterin:	J.-Prof. Dr. Polina Sharapova
Drittgutachter:	Prof. Dr. Stefan Schumacher
Mitglied der Promotionskommission:	Dr. Uwe Gerstmann

Zusammenfassung

In dieser Arbeit werden theoretische Modelle für die Beschreibung der Wechselwirkung zwischen Halbleiternanostrukturen und Quantenlicht in Mikrokavitäten formuliert und analysiert. Das Ziel dieser Arbeit ist das Ergründen und Verstehen von Eigenschaften die exklusiv für eine quantenoptische Behandlung sind und ein hohes Anwendungspotential für Quanten-Anwendungen bieten, um solche zu entwerfen oder zu verbessern. Zunächst werden Systeme behandelt, deren Materie sich anfangs im elektronischen Grundzustand befindet und durch ein quantenoptisches Lichtfeld angeregt wird. Für Λ-Typ Drei-Niveau-Systeme lässt sich zeigen dass Verluste im quantenoptischen Regime vorteilhaft genutzt werden können, etwa beim Präperieren von speziellen stationären Zuständen. Darüberhinaus wird gezeigt dass elektromagnetisch-induzierte Transparenz durch eine nichtklassische Anregung verstärkt wird. Für Zwei-Band-Modelle wird die Besetzungsdynamik mit analytischen und numerischen Methoden untersucht und spezielle stationäre Zustände werden demonstriert. Nachfolgend werden Messdaten von Vier-Wellen-Mischen-Experimenten an Ensemblen von Halbleiter-Quantenpunkten mit einem semiklassischen Modell analysiert. Hier wird die zeitliche Kontrolle von Photonen-Echos simuliert und die Hauptdämpfungsprozesse werden diskutiert. Anschließend wird ein Ausblick auf die Beschreibung von Vier-Wellen-Mischen-Prozessen mit quantenoptischer Anregung gegeben und genäherte Ergebnisse präsentiert. Die Arbeit endet mit einer Zusammenfassung und einem Ausblick für zukünftige Forschungsprojekte.

Summary

In this thesis, we formulate and analyze theoretical models to describe the interaction between semiconductor nanostructures and quantum light in microcavities. The aim is to explore and understand properties that are exclusive for a quantum-optical treatment and have a high potential in application to create new or to improve existing quantum devices. We begin with systems whose material system is initially in its electronic ground state and is excited by a quantum-optical light field. For Λ-type three-level systems, we show that losses can be used as an advantage in order to create special steady states. Furthermore, we show that electromagnetically induced transparency can be enhanced by using non-classical light. For two-band models, we investigate the population dynamics with analytical and numerical methods and demonstrate the formation of special steady states. Hereinafter, we analyze data obtained from four-wave-mixing experiments performed on ensembles of semiconductor quantum dots, where the theoretical description is based on a semiclassical model. In particular, the temporal control of photon echoes is simulated and the main damping mechanisms are discussed. Subsequent, we provide an outlook towards four-wave-mixing processes with quantum-optical excitations and present a number of approximate results. We close with a summary and an outlook of possible future research projects.

List of Scientific Contributions

Doctorate-Related Publications and Presentations

Peer-Reviewed Publications

(1) **H. Rose**, O. V. Tikhonova, T. Meier, and P. R. Sharapova, Steady states of Λ-type three level systems excited by quantum light with various photon statistics in lossy cavities, New J. Phys. **24**, 063020 (2022).

(2) **H. Rose**, D. V. Popolitova, O. V. Tikhonova, T. Meier, and P. R. Sharapova, Dark-state and loss-induced phenomena in the quantum-optical regime of Λ-type three-level systems, Phys. Rev. A **103**, 013702 (2021).

(3) A. N. Kosarev, **H. Rose**, S. V. Poltavtsev, M. Reichelt, C. Schneider, M. Kamp, S. Höfling, M. Bayer, T. Meier, and I. A. Akimov, Accurate photon echo timing by optical freezing of exciton dephasing and rephasing in quantum dots, Commun. Phys. **3**, 228 (2020).

Conference Proceedings

(4) **H. Rose**, O. V. Tikhonova, T. Meier, and P. R. Sharapova, Theoretical analysis of correlations between two quantum fields exciting a three-level system using the cluster-expansion approach, Proc. SPIE **11999**, 1199905 (2022).

(5) M. Reichelt, **H. Rose**, A. N. Kosarev, S. V. Poltavtsev, M. Bayer, I. A. Akimov, C. Schneider, M. Kamp, S. Höfling, and T. Meier, Controlling the emission time of photon echoes by optical freezing of exciton dephasing and rephasing in quantum-dot ensembles, Proc. SPIE **11684**, 116840X (2021).

Preprints and Reports

(6) S. Grisard, **H. Rose**, A. V. Trifonov, R. Reichhardt, D. E. Reiter, M. Reichelt, C. Schneider, M. Kamp, S. Höfling, M. Bayer, T. Meier, and I. A. Akimov, Multiple Rabi rotations of trions in InGaAs quantum dots observed by photon echo spectroscopy with spatially shaped laser pulses, arXiv:2205.07771 (submitted to Phys. Rev. B)

(7) **H. Rose**, A. N. Vasil'ev, O. V. Tikhonova, T. Meier, and P. R. Sharapova, Excitation of an electronic band structure by a single-photon Fock state, Zenodo (2021). https://doi.org/10.5281/zenodo.5774986

(8) **H. Rose**, A. N. Vasil'ev, O. V. Tikhonova, T. Meier, and P. R. Sharapova, Quantum-optical excitations of semiconductor nanostructures in a microcavity using a two-band model and a single-mode quantum field (submitted to Phys. Rev. A)

Conference and Workshop Presentations

- **H. Rose**, "Exploring Semiconductor Quantum Optics", Humboldt meets Leibniz, Hannover, Germany, June 2022 (talk)
- S. Grisard, **H. Rose**, A. V. Trifonov, R. Reichhardt, D. E. Reiter, M. Reichelt, C. Schneider, M. Kamp, S. Höfling, M. Bayer, T. Meier, and I. A. Akimov, "Nonlinear spectroscopy of InGaAs semiconductor quantum dots with classical and quantum light", Kick Off-Workshop TRR 142-3, Bad Sassendorf, Germany, June 2022 (split talk)
- **H. Rose**, O. V. Tikhonova, T. Meier, and P. R. Sharapova, "Theoretical analysis of correlations between two quantum fields exciting a three-level system using the cluster-expansion approach", SPIE Photonics West 2022 On Demand, Ultrafast Phenomena and Nanophotonics XXVI, San Francisco (online), USA, February 2022 (talk)
- **H. Rose**, A. N. Kosarev, S. V. Poltavtsev, M. Reichelt, C. Schneider, M. Kamp, S. Höfling, M. Bayer, I. A. Akimov, and T. Meier, "Optical control of the emission time of photon echoes from quantum dot ensembles", 17th International Conference on Optics of Excitons in Confined Systems (OECS17), Dortmund (online), Germany, September 2021 (poster)
- **H. Rose**, A. N. Kosarev, S. V. Poltavtsev, M. Reichelt, C. Schneider, M. Kamp, S. Höfling, M. Bayer, I. A. Akimov, and T. Meier, "Accurate photon echo timing by optical freezing of exciton dephasing and rephasing in quantum dot ensembles", 7th SFB/TRR Workshop, (online), Germany, September 2020 (talk)
- **H. Rose**, A. N. Kosarev, S. V. Poltavtsev, M. Reichelt, C. Schneider, M. Kamp, S. Höfling, M. Bayer, I. A. Akimov, and T. Meier, "Temporal control of photon echoes from quantum dot ensembles", 15th International Conference on Nonlinear Optics and Excitation Kinetics in Semiconductors (NOEKS15), Münster (online), Germany, September 2020 (talk)
- **H. Rose**, D. V. Popolitova, O. V. Tikhonova, P. R. Sharapova, T. Meier, "The interaction of a three-level system with quantized light", 15th International Conference on Nonlinear Optics and Excitation Kinetics in Semiconductors (NOEKS15), Münster (online), Germany, September 2020 (poster)

Non-Doctorate-Related Publications and Presentations

- J. Paul, **H. Rose**, E. Swagel, T. Meier, J. K. Wahlstrand, and A. D. Bristow, Coherent Contributions to Population Dynamics in a Semiconductor Microcavity, Phys. Rev. B, **105**, 115307 (2022).
- **H. Rose**, J. Paul, J. K. Wahlstrand, A. D. Bristow, and T. Meier, Theoretical analysis and simulations of two-dimensional Fourier transform spectroscopy performed on exciton-polaritons of a quantum-well microcavity system, Proc. SPIE **11684**, 1168414 (2021), presented at SPIE Photonics West 2021, Ultrafast Phenomena and Nanophotonics XXV, San Francisco (online), USA, March 2021 (talk)

Contents

Introduction 1

Semiconductor quantum optics is a multi-faceted field that combines the electronic properties of semiconductor structures with quantum-optical excitations with the overarching goals to obtain novel fundamental insight and to create new quantum devices using quantum-optical functionalities [1]. From the viewpoint of semiconductor optics, the replacement of classical light with quantum light has obvious benefits, since the former is fully described by its amplitude and its phase, while the latter has more degrees of freedom, such as its photon statistics and quantum correlations, e.g, photon-number correlations [2–4]. So far, the field of quantum optics usually considers quite simple material models, such as few-level systems that suitably describe atoms [5], but often are not sufficient for solid state systems. Here, the steps to move from atomic systems to semiconductor systems allow for a richer dynamics in the more complex electronic system and, in turn, for more possibilities and advanced functionalities in quantum technologies, quantum simulations, and quantum communication. In contrast to Ref. [1], we do not consider many-body Coulomb interaction in this thesis, since we want to focus on the quantum light as the main complexity. A powerful method in the context of semiconductor quantum optics is quantum light spectroscopy [6–16], which is an extension of conventional optical spectroscopy methods that were successfully applied to study various types of systems [17–26]. A method of central importance is four-wave-mixing spectroscopy [27, 28], which is a nonlinear optical process [29–31] and has been widely applied to study fundamental properties of semiconductor nanostructures [32–50]. Extending conventional four-wave-mixing spectroscopy to a quantum description of light, resulting in quantum wave-mixing spectroscopy, is a highly promising candidate for the development of quantum memories on the basis of ensembles of semiconductor quantum dots, which can be used for the development of quantum devices.

In this thesis, we divide the complex problem of quantum wave mixing into two separate components, which is studying the systems' dynamics after exciting with a single quantum-optical pulse and studying four-wave mixing by a semiclassical model, which is finally combined to describe four-wave mixing with quantum pulses. We start by pointing out the fundamentals on quantum states of light and their interaction with material systems in Chapter 2. Afterwards, we move towards Λ-type three-level systems that are excited by a quantum field in optical microcavities in Chapter 3, where dark-state and loss-induced phenomena are studied. We demonstrate that electromagnetically induced transparency can be enhanced by using non-classical states of light and provide an alternate approach for the analysis of light-matter interaction based on the quantum polarization. We also show that lossy cavities may lead to the formation of special steady states, which has several benefits compared to other methods. Afterwards, we focus on two-band models in Chapter 4, where the population dynamics after an initial excitation with quantum

light is investigated by analytical and numerical methods. The analytical investigation is based on the eigenvalue problem of the Hamiltonian and provides novel insights and explicit expressions for the steady-state value of the ground-state probability are given. The numerical treatment demonstrates the formation of special steady states inside the band under non-resonant excitation conditions. Subsequent, we analyze data obtained from four-wave-mixing experiments in Chapter 5, where we simulate the temporal control of photon echoes with a semiclassical model. We identify the main damping mechanism as spatial averaging on the detector and demonstrate that it can be bypassed by shaping the incident pulses. The remaining main damping mechanism is the coupling to longitudinal acoustic phonons, as confirmed by an agreement between measured and simulated data. Finally, we give an outlook to quantum wave mixing in Chapter 6, where we present simulated four-wave-mixing signals for both, homogeneous and inhomogeneous systems, that are based on several approximations. This thesis ends in Chapter 7 by summarizing the results and giving an outlook towards further research.

Fundamentals 2

In this chapter, we give an overview about the fundamentals of this thesis. We start with the quantization of a classical multi-mode electromagnetic field in a given quantization volume, which leads to a Hamiltonian that describes quantized light fields. Subsequently, we will identify the eigenstates of this Hamiltonian as Fock states and discuss their properties. Then, we introduce coherent states and squeezed states and demonstrate and discuss their general properties including their photon statistics and Wigner functions. Lastly, we describe the light-matter interaction between material models with several discrete energy levels and a multi-mode quantum field. We start with the formulation of the Hamiltonian and present the equations of motion. This is followed by an analysis of the Jaynes-Cummings model, which allows us to point out central differences between a quantum theory and a semiclassical theory. The content in this chapter mainly follows standard procedures which can be found in textbooks [1, 5].

2.1 Quantization of the Electromagnetic Field

The quantization of the electromagnetic field is a problem that was firstly addressed a century ago [51, 52] and is nowadays a topic that is covered by a number of standard textbooks [1, 5, 53–56]. Here, we consider the quantization of the electromagnetic field that is free from any sources. The propagation and time-evolution of a classical electromagnetic field approach is fully described by Maxwell's equations which in absence of free charges and free currents read:

$$\nabla \times \boldsymbol{E} = -\frac{\partial \boldsymbol{B}}{\partial t}, \tag{2.1a}$$

$$\nabla \cdot \boldsymbol{D} = 0, \tag{2.1b}$$

$$\nabla \times \boldsymbol{H} = \frac{\partial \boldsymbol{D}}{\partial t}, \tag{2.1c}$$

$$\nabla \cdot \boldsymbol{B} = 0. \tag{2.1d}$$

Maxwell's equations state relations between the electric vector $\boldsymbol{E}$ and the inductive vector $\boldsymbol{B}$ as well as between the magnetic field vector $\boldsymbol{H}$ and displacement vector $\boldsymbol{D}$, where the constitutive relations apply:

$$\boldsymbol{B} = \mu_0 \boldsymbol{H}, \tag{2.2}$$

$$\boldsymbol{D} = \epsilon_0 \boldsymbol{E}, \tag{2.3}$$

where ϵ_0 is the vacuum permittivity and μ_0 is the vacuum permeability, which fulfill the relation $\frac{1}{\sqrt{\epsilon_0 \mu_0}} = c$, where c denotes the speed of light in vacuum.

With Eq. (2.1a), Eq. (2.1c), Eq. (2.2), and Eq. (2.3) one can show that the electric field vector $\boldsymbol{E}$ must satisfy the wave equation:

$$\nabla^2 \boldsymbol{E} - \frac{1}{c_0^2} \frac{\partial^2 \boldsymbol{E}}{\partial t^2} = 0. \tag{2.4}$$

Henceforth, we will consider the light being confined inside a one-dimensional cavity along the z-axis with length L, allowing for the formation of discretized modes of the electric field that are polarized along the x-direction. At the boundaries $z = 0$ and $z = L$, the x-component of the electric field must be zero, as shown in the schematical drawing Figure 2.1.

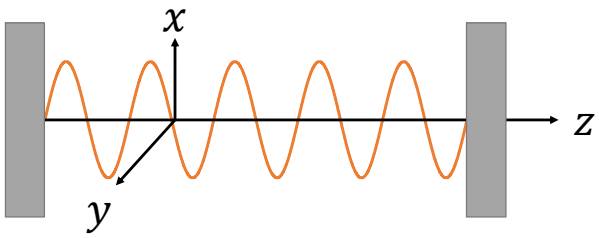

Figure 2.1: Schematical drawing of an electric field confined in a one-dimensional cavity. (After [5])

Therefore, an ansatz for the solution of Eq. (2.4) is a superpositon of standing waves, while a solution of the magnetic field can be referred from Eq. (2.1c):

$$E_x(z,t) = \sum_j A_j q_j(t) \sin\big(k_j z\big), \tag{2.5}$$

$$H_y(z,t) = \sum_j \frac{\varepsilon_0}{k_j} A_j \dot{q}_j(t) \cos\big(k_j z\big), \tag{2.6}$$

where q_j denotes the time-dependent amplitude of the cavity mode, and $k_j = \frac{j\pi}{L}$ are the allowed wave-vectors for standing waves, where j must be a non-negative integer greater than 0. The constant A_j is given by

$$A_j = \sqrt{\frac{2\nu_j^2 m_j}{V \epsilon_0}}, \tag{2.7}$$

where $V = LA$ is the quantization volume with A being the lateral surface area of the cavity mirrors, $\nu_j = ck_j$ is the eigenfrequency of the cavity mode, and m_j is a constant.

We continue by considering the classical field Hamiltonian and evaluate it with the above expressions:

$$H = \frac{1}{2}\int \mathrm{d}V(\epsilon_0 E_x^2 + \mu_0 H_y^2) = \sum_j \left(\frac{m_j \nu_j^2 q_j^2}{2} + \frac{p_j^2}{2m_j}\right), \tag{2.8}$$

where $p_j = m_j \dot{q}_j$. The total energy of each mode is equivalent to a harmonic oscillator, after identifying q_j as a Cartesian coordinate, m_j as a mass, and p_j as canonical momentum. The quantization is now performed by identifying the Cartesian coordinate q_j and the canonical momentum p_j as operators that obey the canonical commutation relations:

$$[q_j, p_{j'}]_- = i\hbar\delta_{j,j'}, \tag{2.9}$$

$$[q_j, q_{j'}]_- = [p_j, p_{j'}]_- = 0, \tag{2.10}$$

where $[A, B]_- = AB - BA$ is the commutator, $\hbar$ is the reduced Planck constant, and $\delta_{i,j}$ is the Kronecker delta. Next, we define the dimensionless variables Q_j and P_j as, which are called quadrature operators:

$$Q_j = \sqrt{\frac{m_j \nu_j}{2\hbar}} q_j, \tag{2.11}$$

$$P_j = \frac{1}{\sqrt{2m_j \nu_j \hbar}} p_j, \tag{2.12}$$

which we use to define another set of operators:

$$b_j = Q_j + iP_j, \tag{2.13}$$

$$b_j^\dagger = Q_j - iP_j, \tag{2.14}$$

which consequently obey the following commutation relations:

$$[b_j, b_{j'}^\dagger]_- = \delta_{j,j'}, \tag{2.15}$$

$$[b_j, b_{j'}]_- = [b_j^\dagger, b_{j'}^\dagger]_- = 0, \tag{2.16}$$

and allow us to rewrite the Hamiltonian from Eq. (2.8) as follow:

$$H = \sum_j \hbar\nu_j \left(b_j^\dagger b_j + \frac{1}{2}\right). \tag{2.17}$$

b_j is the photon annihilation operator and $b_j^\dagger$ the photon creation operator for a photon from the j-th mode. This designation becomes more clear when studying the eigenstates of the Hamiltonian, which is done in the next section.

2.2 Fock-State Representation

For simplicity, we continue the description for a single-mode field. Considering the eigenvalue problem of the Hamiltonian provides:

$$H\,|n\rangle = \hbar\nu\left(b^\dagger b + \frac{1}{2}\right)|n\rangle = E_n\,|n\rangle\,, \tag{2.18}$$

with eigenenergies E_n and eigenstates $|n\rangle$. The eigenenergies can be calculated as:

$$E_n = \hbar\nu\left(n + \frac{1}{2}\right), \quad n = 0, 1, 2, \ldots \tag{2.19}$$

Here, it was used that

$$b^\dagger b\,|n\rangle = n\,|n\rangle\,. \tag{2.20}$$

Thus, $b^\dagger b$ can be identified as photon number operator. The eigenstate $|n\rangle$ is called Fock state and contains exactly n photons. With algebraic manipulations (see, e.g., Ref. [5] for more details), one can show that:

$$b\,|n\rangle = \sqrt{n}\,|n-1\rangle\,, \tag{2.21}$$

$$b^\dagger\,|n\rangle = \sqrt{n+1}\,|n+1\rangle\,, \tag{2.22}$$

which means that the photon annihilation operator b removes a photon from the Fock state and the photon creation operator adds a photon to the Fock state. These equations allow to find a closed expressions for a Fock state $|n\rangle$:

$$|n\rangle = \frac{(b^\dagger)^n}{\sqrt{n!}}\,|0\rangle\,, \tag{2.23}$$

where the Fock state $|0\rangle$ is considered as vacuum state. Fig. 2.2 serves as an illustration by depicting wave functions $\Psi_n(q) = \langle q|n\rangle$ of the quantum harmonic oscillator, which are the real space representation of Fock states. The action of the photon creation and annihilation operators $b^\dagger$ and b is schematically shown with arrows that indicate a change in the photon number.

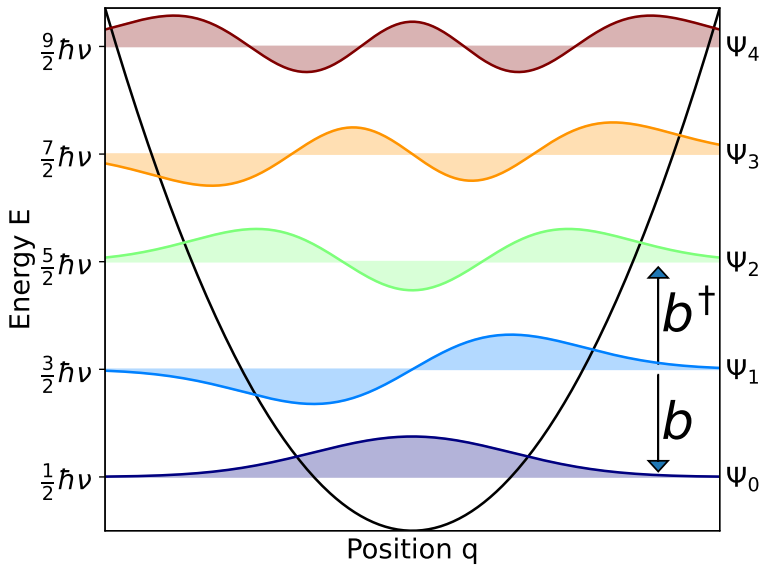

Figure 2.2: Wave functions Ψ_n of the quantum harmonic oscillator in real space for the energetically lowest five states. The x-axis for the respective wave function has an offset, which represents the energy that corresponds to the state, which is depicted on the y-axis.

Fock states furthermore are a complete set and thus can be used to represent an arbitrary quantum mode $|\Psi\rangle$ as:

$$|\Psi\rangle = \sum_{k=0}^{\infty} c_k \, |k\rangle \,, \tag{2.24}$$

where $c_k = \langle k|\Psi\rangle$ are complex expansion coefficients that can be physically interpreted as probability amplitudes, since $|c_k|^2$ is the probability for measuring k photons in the mode, also called photon statistics. Working in the Fock state basis is convenient for theoretical investigations, as it allows a consistent treatment of arbitrary quantum states.

2.3 Special Quantum States of Light

In the following subsections, we will introduce quantum states that are relevant throughout this thesis, by considering their definition, photon statistics, and phase-space representations.

2.3.1 Coherent States

The coherent state $|\alpha\rangle$ is defined as the eigenstate of the photon annhilation operator b [57]:

$$b\,|\alpha\rangle = \alpha\,|\alpha\rangle \tag{2.25}$$

where the eigenvalue α is its complex-valued amplitude. From this definition one can show that its Fock state representation reads:

$$|\alpha\rangle = \sum_{k=0}^{\infty} c_k\,|k\rangle = \sum_{k=0}^{\infty} e^{\frac{-|\alpha|^2}{2}} \frac{\alpha^k}{\sqrt{k!}}\,|k\rangle\,, \tag{2.26}$$

and subsequently the mean photon number N is:

$$N = \langle\alpha|\, b^\dagger b\,|\alpha\rangle = |\alpha|^2. \tag{2.27}$$

The photon statistics $|c_k|^2$ of a coherent state $|\alpha\rangle$ with a mean photon number of $N = 10$ is shown in Fig. 2.3.

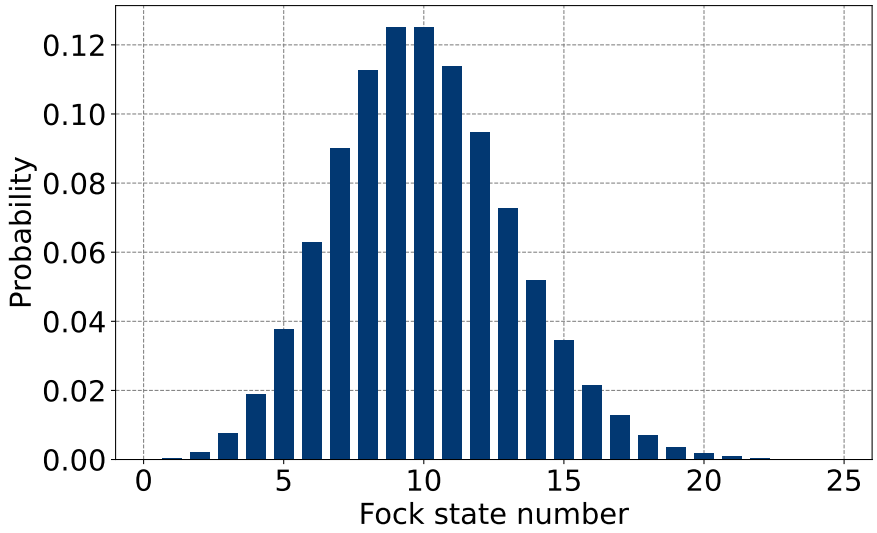

Figure 2.3: Photon statistics $|c_k|^2$ for a coherent state with a mean photon number of $N = 10$.

Coherent states are the states that show the most classical behavior. This can e.g. be demonstrated by considering normally-ordered expectation values:

$$\left\langle (b^\dagger)^J b^K \right\rangle = \langle\alpha|\, (b^\dagger)^J b^K\,|\alpha\rangle = (\alpha^*)^J \alpha^K, \tag{2.28}$$

where we see that the photon operators are just replaced by the complex-valued amplitude

α, which is equivalent to a factorization in a classical treatment where α would correspond to a classcial field amplitude [1]. Another approach to represent quantum states is defining an operator that creates the state when applied to the vacuum state $|0\rangle$, as we already did for the Fock state in Eq. (2.23). There coherent state can written as:

$$|\alpha\rangle = \exp\left(\alpha b^\dagger - \alpha^* b\right)|0\rangle = D(\alpha)\,|0\rangle\,, \tag{2.29}$$

where $D(\alpha)$ is the displacement operator. The word "displacement" becomes clearer when the phase-space representation is considered.

Phase-space functions are a helpful tool when studying quantum light. These functions are quasi-probability distributions that represent a quantum state in the quadrature space, i.e. in terms of Q and P. For this matter, we will consider the Wigner function, that was originally defined as [58]

$$W(q,p) = \frac{1}{2\pi\hbar}\int_{-\infty}^{\infty} \mathrm{d}x \left\langle q + \frac{1}{2}x\right| \rho \left|q - \frac{1}{2}x\right\rangle \exp(ipx/\hbar), \tag{2.30}$$

where ρ is the density matrix of the quantum state, which is given by $\rho = |\Psi\rangle\langle\Psi|$ for a pure state $|\Psi\rangle$. Nowadays, there are more modern, but equivalent expressions, that are based on coherent states [5]

$$W(\tilde{\alpha}) = \frac{1}{\pi^2}\int \mathrm{Tr}\left[\rho \exp\left(-\beta b^\dagger + \beta^* b\right)\right] \exp(\beta\tilde{\alpha}^* - \beta^*\tilde{\alpha})\mathrm{d}^2\beta. \tag{2.31}$$

With Eq. (2.31), the Wigner function of a coherent state $\rho = |\alpha\rangle\langle\alpha|$ reads

$$W_{\mathrm{coherent}}(\tilde{\alpha}) = \frac{2}{\pi}\exp\left(-2|\tilde{\alpha} - \alpha|^2\right). \tag{2.32}$$

Comparing this expression with the Wigner function of a vacuum state $\rho = |0\rangle\langle 0|$:

$$W_{\mathrm{vacuum}}(\tilde{\alpha}) = \frac{2}{\pi}\exp\left(-2|\tilde{\alpha}|^2\right), \tag{2.33}$$

reveals that the coherent state is a vacuum state that got displaced by its complex amplitude α, where the displacement is described by the displacement operator $D(\alpha)$. Fig. 2.4 shows the Wigner functions from Eq. (2.33) and Eq. (2.32) for $\alpha = 2 + 2i$ to visualize the displacement. We see that the phase-space functions are distributions, rather than single points, which is an expression of the Heisenberg uncertainty relation.

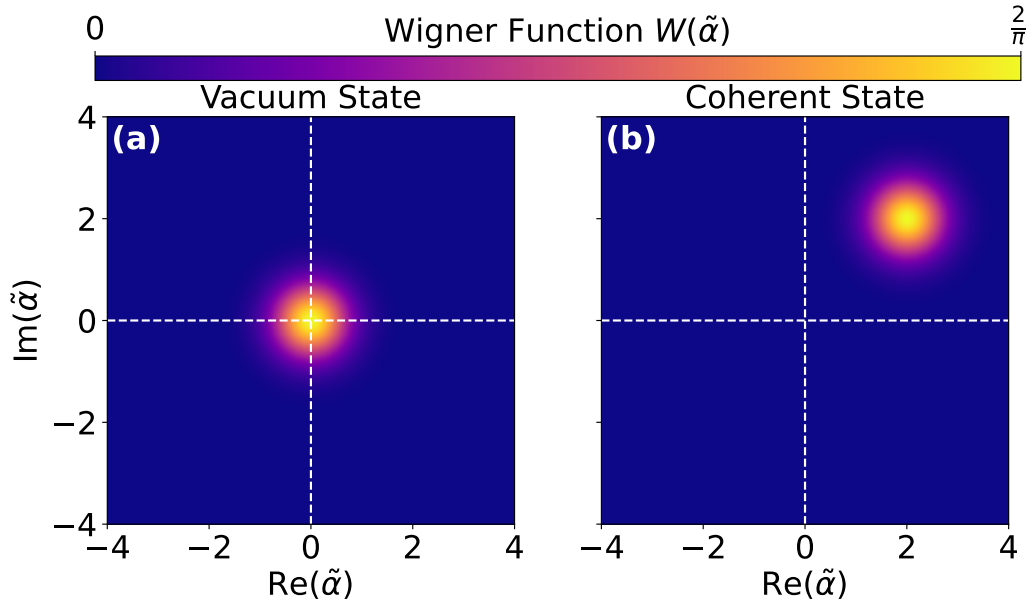

Figure 2.4: Wigner function $W(\tilde{\alpha})$ for (a) a vacuum state $|0\rangle$ (b) a coherent state $|\alpha\rangle$ with $\alpha = 2+2i$, corresponding to a mean photon number of $N = 8$.

2.3.2 Squeezed States

To present the idea of squeezed states, it is more instructive to start from the Heisenberg uncertainty relation. It states that the product of the uncertainties of two Hermitian operators A and B has a lower bound that is finite if these operators do not commute:

$$(\Delta A)(\Delta B) \geq \frac{1}{2}|\langle [A,B]_- \rangle|. \tag{2.34}$$

Since this inequality only applies to the product of uncertaincies, one can prepare states in which

$$(\Delta A)^2 < \frac{1}{2}|\langle [A,B]_- \rangle| \quad \text{or} \quad (\Delta B)^2 < \frac{1}{2}|\langle [A,B]_- \rangle|, \tag{2.35}$$

which are called squeezed states. In our case, the operators A and B correspond to the quadratures Q and P defined in Eq. (2.11) and Eq. (2.12), which we now rename as X_1 and X_2 as commonly done in literature. In this case, the inequality reads:

$$(\Delta X_1)(\Delta X_2) \geq \frac{1}{4}, \tag{2.36}$$

and a squeezed state must fulfill

$$(\Delta X_1)^2 < \frac{1}{4} \quad \text{or} \quad (\Delta X_2)^2 < \frac{1}{4}. \tag{2.37}$$

To introduce a state that matches the condition Eq. (2.37) we start with the mathematical description and will later mention physical processes for the generation. A single-mode squeezed vacuum state $|\xi\rangle$ is described by

$$|\xi\rangle = \exp\left(\frac{1}{2}\left(\xi^* b^2 - \xi b^{\dagger 2}\right)\right)|0\rangle = S(\xi)\,|0\rangle\,, \tag{2.38}$$

where $S(\xi)$ is the squeezing operator and ξ is called squeezing and is often decomposed into $\xi = re^{i\vartheta}$, where $r = |\xi|$ is the squeezing parameter. The squeezing operator only allows for the creation or annihilation of 2 photons, expressed by $b^{\dagger 2}$ and b^2, respectively. This reflects in the Fock state representation of a squeezed vacuum state, which can be calculated as:

$$|\xi\rangle = \sum_{k=0}^{\infty} c_k\,|k\rangle = \sum_{m=0}^{\infty}(-1)^m \frac{\sqrt{(2m)!}}{2^m m!}\frac{(e^{i\vartheta}\tanh(r))^m}{\sqrt{\cosh(r)}}\,|2m\rangle \quad \text{with} \quad k = 2m. \tag{2.39}$$

Here, c_k can only be non-zero if k is even and can be written as $k = 2m$, where m is an integer. Even though the squeezed vacuum is a vacuum state, it can have an arbitrarily large mean photon number that is given by:

$$N = \langle\xi|\, b^\dagger b\,|\xi\rangle = \sinh^2(r). \tag{2.40}$$

The photon statistics $|c_k|^2$ for a squeezed vacuum state with a mean photon number of $N = 10$ is depicted in Fig. 2.5. One can see that the probability decreases with increasing Fock state number and only even photon numbers result in a finite probability.

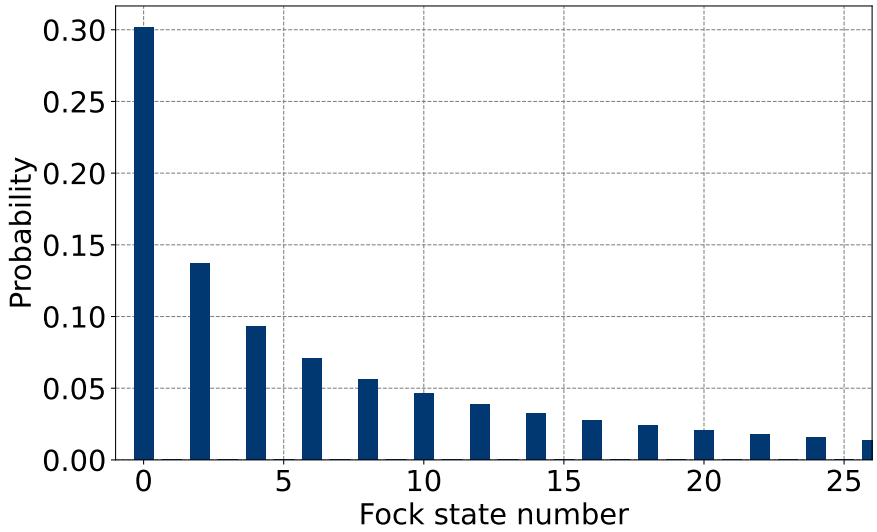

Figure 2.5: Photon statistics $|c_k|^2$ for a squeezed vacuum state with a mean photon number of $N = 10$.

To demonstrate that this state is a squeezed state according to Eq. (2.37), we now consider the uncertainties of the quadratures X_1 and X_2, which are given by:

$$\Delta^2 X_1 = \left\langle X_1^2 \right\rangle - \langle X_1 \rangle^2 = \frac{1}{4}(-\sinh(2r)\cos(\vartheta) + \cosh(2r)) \overset{\vartheta=0}{=} \frac{1}{4}\exp(-2r), \tag{2.41}$$

$$\Delta^2 X_2 = \left\langle X_1^2 \right\rangle - \langle X_1 \rangle^2 = \frac{1}{4}(\sinh(2r)\cos(\vartheta) + \cosh(2r)) \overset{\vartheta=0}{=} \frac{1}{4}\exp(2r). \tag{2.42}$$

This demonstrates that a finite squeezing parameter r leads to quadrature squeezing. In the special case $\vartheta = 0$, the smallest uncertainty is obtained for X_1, while, in general, it is not necessarily found for either X_1 or X_2, but for a superposition of these.

The squeezing is also reflected in the Wigner function, see Fig. 2.4(a), where the Wigner function for a squeezed vacuum state $|\xi\rangle$ is shown for $r = 0.658479$ (corresponding to a mean photon number of ≈ 0.5) and $\vartheta = \pi/2$. The Wigner function resembles a vacuum state, which, however, is squeezed along the direction rotated by $\vartheta/2$ from the $\mathrm{Re}(\tilde{\alpha})$-axis, while being stretched along the direction rotated by $\vartheta/2$ from the $\mathrm{Im}(\tilde{\alpha})$-axis. This has the interesting consequence that a squeezed vacuum state leads to less noise (quadrature uncertainty) than having no light at all, which makes it very useful for quantum metrology applications [59].

Beside squeezed vacuum states, one can also generate states that share properties of both, coherent and squeezed states. One example are displaced squeezed vacuum states $|\alpha, \xi\rangle$,

which are obtained by applying both operators:

$$|\alpha, \xi\rangle = D(\alpha)S(\xi)\,|0\rangle\,, \tag{2.43}$$

where the mean photon number is given by the sum of the mean photon numbers of the coherent and squeezed components:

$$N = \langle \alpha, \xi|\, b^\dagger b\, |\alpha, \xi\rangle = |\alpha|^2 + \sinh^2(r) \tag{2.44}$$

Fig. 2.6(b) shows the corresponding Wigner function for the same squeezing as before and a displacement of $\alpha = 2 + 2i$, as used for the coherent state in Fig. 2.4(b). The result is analog to the case for coherent states, as we find a squeezed vacuum state $|\xi\rangle$ that is displaced by α.

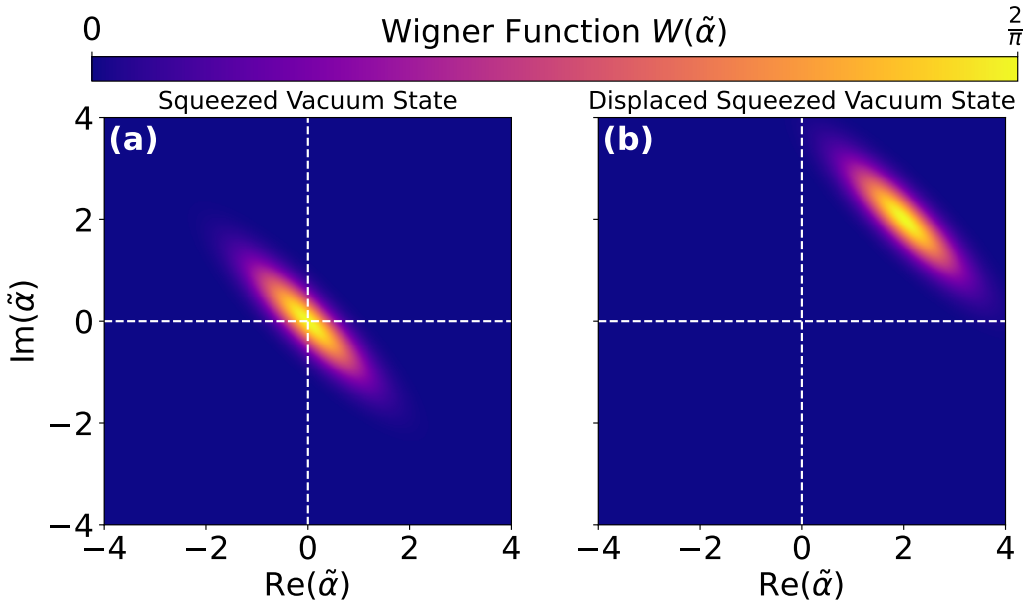

Figure 2.6: Wigner function $W(\tilde{\alpha})$ for (a) a squeezed vacuum state $|\xi\rangle$ with $\xi = 0.658479\exp(i\pi/2)$, corresponding to a mean photon number of $N = 0.5$ (b) a displaced squeezed vacuum state $|\alpha, \xi\rangle$ with $\alpha = 2 + 2i$ and $\xi = 0.658479\exp(i\pi/2)$, corresponding to a mean photon number of $N = 8.5$.

Practical realizations of squeezed states typically rely on nonlinear optical processes, like spontaneous parametric down-conversion [60–63], four-wave mixing [64] or second-harmonic conversion in optical cavities [65].

In contrast to coherent states, squeezed states are considered to be non-classical light, since there is no equivalent in a classical theory. There are several indicators for the presence of non-classicality, such as inequalities of phase-space functions [66, 67].

2.4 Light-Matter Interaction

In this section, we describe the fully quantized light-matter interaction. We start with the derivation of the Hamiltonian for a fully quantized description of light-matter interaction, allowing for the description of a material system with several discrete energy levels that is excited by multiple quantum light modes inside of an optical cavity. Afterwards, we introduce the equations of motion for such systems and will then move towards a simple example, allowing us to demonstrate general properties of such systems.

2.4.1 Hamiltonian

The total Hamiltonian H can be written as a sum of Hamiltonians describing the matter H_{Matter}, the light field H_{Light}, and the interaction between these $H_{\text{Interaction}}$:

$$H = H_{\text{Matter}} + H_{\text{Light}} + H_{\text{Interaction}}. \tag{2.45}$$

We now continue with finding expressions for these Hamiltonians. In Section 2.1 we already concluded that the Hamiltonian of the light field H_{Light} is given by Eq. (2.17). The material is modeled as an arbitrary arrangement of discrete energy levels given by a complete set $\{|i\rangle\}$ with $i = 1, 2, 3, \ldots$, where we define the transition operator $\sigma_{ij} = |i\rangle \langle j|$, that describes the transition from the state $|j\rangle$ to the state $|i\rangle$. The Hamiltonian H_{Matter} is now required to fulfill the eigenvalue equation:

$$H_{\text{Matter}} |i\rangle = \tilde{E}_i |i\rangle , \tag{2.46}$$

where $\tilde{E}_i$ is the eigenenergy of the matter state $|i\rangle$. Thus, the Hamiltonian can be written as:

$$H_{\text{Matter}} = \sum_i \tilde{E}_i |i\rangle \langle i| = \sum_i \tilde{E}_i \sigma_{ii}. \tag{2.47}$$

The interaction between light and matter is treated in the dipole approximation, so that:

$$H_{\text{Interaction}} = -e_0 \boldsymbol{r} \cdot \boldsymbol{E}, \tag{2.48}$$

where e_0 is the charge of an electron and $\boldsymbol{r}$ is its position vector. From the completeness of the set $\{|i\rangle\}$ we can rewrite the term $e_0\boldsymbol{r}$:

$$e_0 \boldsymbol{r} = \sum_{i,j} e_0 |i\rangle \langle i| \boldsymbol{r} |j\rangle \langle j| = \sum_{i,j} \boldsymbol{d}_{ij} \sigma_{ij}, \tag{2.49}$$

where $\boldsymbol{d}_{ij} = e_0 \langle i| \boldsymbol{r} |j\rangle$ is the dipole transition matrix element and the intraband dipole moments $\boldsymbol{d}_{ii}$ are assumed to be zero. Based on the equations given in Section 2.1, one can

rewrite total electric field $\boldsymbol{E}$ as

$$\boldsymbol{E} = \sum_k \tilde{\epsilon}_k \mathcal{E}_k (b_k + b_k^\dagger), \tag{2.50}$$

with the vacuum field amplitude $\mathcal{E}_k = \sqrt{\frac{\hbar \nu_k}{2\epsilon_0 V}}$ and $\tilde{\epsilon}_k$ being the polarization unit vector. Altogether, the total Hamiltonian from Eq. (2.45) can be written as:

$$H = \sum_i E_i \sigma_{ii} + \sum_k \hbar \nu_k \left(b_k^\dagger b_k + \frac{1}{2} \right) + \hbar \sum_{i,j} \sum_k g_k^{ij} \sigma_{ij} (b_k + b_k^\dagger), \tag{2.51}$$

where we introduced the light-matter coupling

$$g_k^{ij} = -\frac{d_{ij} \cdot \tilde{\epsilon}_k \mathcal{E}_k}{\hbar}. \tag{2.52}$$

2.4.2 Equations of Motion

The Hamiltonian H can be used to compute the system's dynamics. Our current analysis is done in the Schrödinger picture, where state vectors are time-dependent, but operators are not. In this case, the time evolution of a state vector is determined by the Schrödinger equation:

$$i\hbar \frac{\partial}{\partial t} |\Psi\rangle = H |\Psi\rangle , \tag{2.53}$$

which allows to compute the time evolution of the expectation values of an observable O with

$$\langle O \rangle = \langle \Psi | O | \Psi \rangle . \tag{2.54}$$

A description with state vectors, however, is limited to pure states. The density matrix (DM) is a generalization of a state-vector and can in general be written as:

$$\rho = \sum_j p_j |\Psi_j\rangle \langle \Psi_j| . \tag{2.55}$$

Its time evolution is determined by the von Neumann equation:

$$\frac{\partial}{\partial t} \rho = \frac{1}{i\hbar} [H, \rho]_- . \tag{2.56}$$

An advantage of the DM formalism is the straightforward inclusion of loss mechanisms with Lindblad terms [68]:

$$\partial_t \rho = \frac{1}{i\hbar}[H, \rho]_- + \sum_L \mathcal{L}_L(\rho), \tag{2.57}$$

where the Lindblad term $\mathcal{L}_L(\rho)$ is given by

$$\mathcal{L}_L(\rho) = L\rho L^\dagger - \frac{1}{2}\left(L^\dagger L\rho + \rho L^\dagger L\right), \tag{2.58}$$

and describes a loss applied to the operator L than can be attributed to physical processes. The time evolution of observables is then computed by:

$$\langle O \rangle = \mathrm{Tr}(\rho O). \tag{2.59}$$

All numerical simulations that will be shown in this thesis were obtained by integrating the differential equations with the Runge-Kutta method of fourth-order.

2.4.3 Jaynes-Cummings Model

The first description of a fully quantized light-matter coupling was performed using the Jaynes-Cummings model (JCM), where the interaction of a two-level absorber and a quantum state of light was introduced [69–71]. In the following, we will use this model and consider the eigenvalue problem of the Hamiltonian to demonstrate properties that are exclusive to quantum-optical treatments. Reducing the Hamiltonian H from Eq. (2.51) to a two-level system (TLS) and a single light mode yields:

$$H = \hbar\nu\left(b^\dagger b + \frac{1}{2}\right) + \hbar\omega\sigma_z + \hbar g(\sigma_+ + \sigma_-)(b + b^\dagger), \tag{2.60}$$

where $\sigma_z = \frac{1}{2}(\sigma_{22} - \sigma_{11}) = \frac{1}{2}(|2\rangle\langle 2| - |1\rangle\langle 1|)$, $\sigma_+ = \sigma_{21} = |2\rangle\langle 1|$, $\sigma_- = \sigma_{12} = |1\rangle\langle 2|$, and $\hbar\omega$ is the energy difference between excited and ground state. Furthermore, we apply the rotating-wave approximation (RWA) in which the terms $\sigma_+ b^\dagger$ and $\sigma_- b$ are omitted, which describe the promotion from the ground to the excited state under emission of a photon and the demotion from the excited to the ground state under the absorption of a photon, respectively and are negligible under resonant excitation conditions. This yields the Jaynes-Cummings Hamiltonian:

$$H_{\mathrm{JC}} = \hbar\nu\left(b^\dagger b + \frac{1}{2}\right) + \hbar\omega\sigma_z + \hbar g(\sigma_+ b + \sigma_- b^\dagger). \tag{2.61}$$

The interaction part now only contains the operators $\sigma_+ b$ and $\sigma_- b^\dagger$, which describe the promotion from the ground to the excited state under absorption of a photon and the demotion from the excited to the ground state under emission of a photon.

Eigenvalue Problem

Since the light-matter interaction leads to the formation of new eigenstates, the solution of the eigenvalue problem allows a transparent insight into this formation. To clearly separate the material states $|1\rangle$ and $|2\rangle$ from the Fock states $|n\rangle$, we proceed with the notation $|-\rangle \equiv |1\rangle$ for the ground and $|+\rangle \equiv |2\rangle$ for the excited state. First, we consider the non-interacting part of the Jaynes-Cummings Hamiltonian

$$H_{\mathrm{JC}}^{0} = \hbar\nu\left(b^{\dagger}b + \frac{1}{2}\right) + \hbar\omega\sigma_z. \tag{2.62}$$

We already know the solution of the eigenvalue problems for the separate parts from Eq. (2.18), Eq. (2.19), and Eq. (2.46):

$$\hbar\nu\left(b^{\dagger}b + \frac{1}{2}\right)|n\rangle = \hbar\nu\left(n + \frac{1}{2}\right)|n\rangle\,, \tag{2.63}$$

$$\hbar\omega\sigma_z\,|\pm\rangle = \pm\frac{\hbar\omega}{2}\,|\pm\rangle\,. \tag{2.64}$$

The eigenstates of H_{JC}^{0} are the product states $|\pm, n\rangle = |\pm\rangle \otimes |n\rangle$, given by a tensor product between $|\pm\rangle$ and $|n\rangle$

$$H_{\mathrm{JC}}^{0}\,|\pm, n\rangle = \hbar\left(\nu\left(n + \frac{1}{2}\right) \pm \frac{\omega}{2}\right)|\pm, n\rangle = E_{\pm,n}^{0}\,|\pm, n\rangle\,. \tag{2.65}$$

With the introduction of an optical detuning as $\Delta = \nu - \omega$, the eigenenergies can be written as:

$$E_{-,n}^{0} = \hbar\left(\nu n + \frac{\Delta}{2}\right), \quad n = 0, 1, 2, \ldots \tag{2.66}$$

$$E_{+,n-1}^{0} = \hbar\left(\nu n - \frac{\Delta}{2}\right), \quad n = 1, 2, 3, \ldots \tag{2.67}$$

Independently on the Fock state number n, the states $|-, n\rangle$ and $|+, n-1\rangle$ have an energy difference of $\hbar\Delta$, while the states $|-, n+1\rangle$ and $|-, n\rangle$ (or $|+, n\rangle$ and $|-, n-1\rangle$) show an energy difference of $\hbar\nu$.

Secondly, we consider the eigenvalue problem of the Jaynes-Cummings Hamiltonian H_{JC} including the interaction:

$$H_{\mathrm{JC}}\left|\Phi_n^{\pm}\right\rangle = E_n^{\pm}\left|\Phi_n^{\pm}\right\rangle. \tag{2.68}$$

In this case, one can show that the eigenenergies read (see Ref. [1] for more details)

$$E_n^{\pm} = \hbar\nu n \pm \hbar\sqrt{\frac{1}{4}\Delta^2 + g_n^2} \tag{2.69}$$

with $g_n = g\sqrt{n}$, and the corresponding eigenstates are given by

$$\left|\Phi_n^+\right\rangle = \cos(\theta_n)\left|+, n-1\right\rangle + \sin(\theta_n)\left|-, n\right\rangle, \tag{2.70}$$

$$\left|\Phi_n^-\right\rangle = \cos(\theta_n)\left|-, n\right\rangle - \sin(\theta_n)\left|+, n-1\right\rangle. \tag{2.71}$$

with

$$\cos(2\theta_n) = \frac{\Delta}{\sqrt{\Delta^2 + 4g_n^2}}, \quad \sin(2\theta_n) = \frac{2g_n}{\sqrt{\Delta^2 + 4g_n^2}}. \tag{2.72}$$

The inclusion of the light-matter interaction leads to relevant changes in the eigenvalues, as their difference now depends on the Fock state number n, which for $\Delta = 0$ reads:

$$\Delta E_n^{\pm} = E_{n+1}^{\pm} - E_n^{\pm} = \hbar\nu \pm \hbar g\left(\sqrt{n+1} - \sqrt{n}\right). \tag{2.73}$$

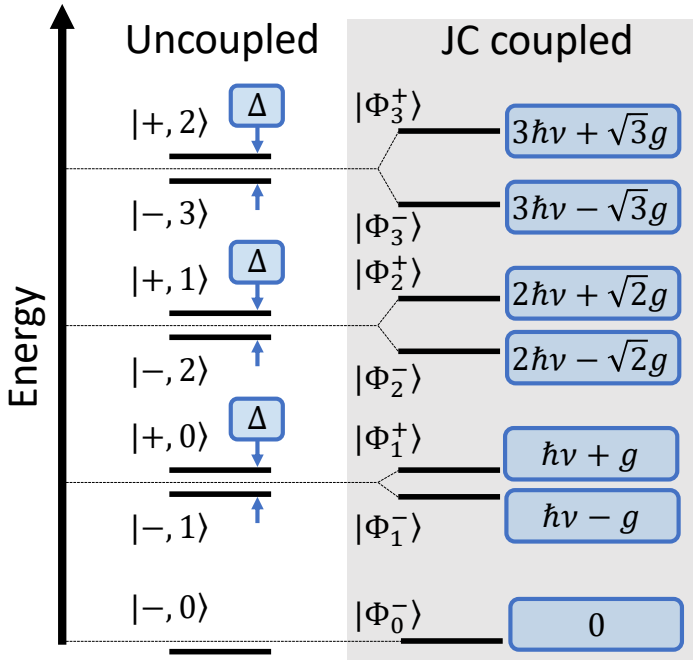

Figure 2.7: Schematical demonstration of the eigenvalues and eigenstates of the Jaynes-Cummings model. The left sides depicts the eigenenergies (horizontal lines) and eigenstates $|\pm, n\rangle$ obtained from the non-interacting part of the Jaynes-Cummings Hamiltonian H_{JC}^0 for a positive detuning $\Delta > 0$, while the right side depicts the same, but for $\Delta = 0$ and the full Jaynes-Cummings Hamiltonian H_{JC}. (After [1])

The energies $E_n^{\pm}$ are known as Jaynes-Cummings ladder and constitute a pure quantum effect. Fig. 2.7 illustrates the solution to the eigenvalue problems for the non-interacting

and the interacting case, resulting in the Jaynes-Cummings ladder. Remarkably, the energy levels of the Jaynes-Cummings ladder, also known as rungs, are not equidistant, which leads to novel dynamics exclusive for a a treatment with a quantum-optical description of light.

Dynamics of the Population Inversion

After discussing the eigenvalue problem and demonstrating the Jaynes-Cummings ladder, we want to show that this has a direct consequence for the time dynamics of such systems. For this, we assume $\Delta = 0$ and treat the system in the interaction picture, where the time evolution is given by

$$i\hbar \frac{\partial}{\partial t} |\Psi\rangle = (H_{\mathrm{JC}} - H_{\mathrm{JC}}^0) |\Psi\rangle . \tag{2.74}$$

We can expand the state vector in the basis set $|\pm, n\rangle$:

$$|\Psi\rangle = \sum_n \left(c_{+,n} |+, n\rangle + c_{-,n} |-, n\rangle \right) . \tag{2.75}$$

Assuming that the TLS is initially in its ground state, i.e. $c_{+,-}(0) = 0$ and $c_{-,n+1} = c_{n+1}$, the probability amplitudes can be computed with Eq. (2.74):

$$c_{+,n} = -ic_{n+1} \sin\left(gt\sqrt{n+1}\right), \tag{2.76}$$

$$c_{-,n+1} = c_{n+1} \cos\left(gt\sqrt{n+1}\right), \tag{2.77}$$

where c_n is the probability amplitude for an arbitrary quantum state of light. Similar to the physical interpretation of $|c_n|^2$ as the probability of finding n photons in the field, $|c_{+,n}|^2$ expresses the probability of finding n photons in the field, while the TLS is in its excited state $|+\rangle$, while $|c_{-,n}|^2$ means the same, but for the ground state $|-\rangle$. The probabilities O_+ and O_- of finding the TLS in its excited and ground state, respectively, are now obtained by calculating the expectation value of the corresponding operators $|+\rangle\langle+|$ and $|-\rangle\langle-|$:

$$O_+ = \langle\Psi|+\rangle\langle+|\Psi\rangle = \sum_{n=0}^{\infty} |c_{+,n}|^2, \quad O_- = \langle\Psi|-\rangle\langle-|\Psi\rangle = \sum_{n=0}^{\infty} |c_{-,n}|^2, \tag{2.78}$$

where $O_+ + O_- = 1$. We see that these probabilities are obtained by the sum over all photon numbers. Now, we consider the inversion I:

$$I = O_+ - O_- = 2O_+ - 1. \tag{2.79}$$

For a coherent state $|\alpha\rangle$ the inversion I is given by:

$$I_{\text{coherent}} = -\sum_{n=0}^{\infty} e^{-|\alpha|^2} \frac{|\alpha|^{2n}}{n!} \cos\left(2gt\sqrt{n}\right). \tag{2.80}$$

Fig. 2.8 shows I_{coherent} for $|\alpha|^2 = 10$ (solid line), together with the inversion predicted from a semiclassical theory (shaded area). The semiclassical theory leads to a Rabi oscillation with a fixed frequency. In contrast, the inversion obtained with a quantum theory results in a Rabi ocillation with a more complicated behavior, showing a collapse and revival behavior, which is a direct consequence of the field quantization [72–74]. This behavior can be understood qualitatively from Eq. (2.80), which is a superposition of oscillations with frequencies $2g\sqrt{n}$ originating from the rungs of the Jaynes-Cummings ladder that give rise to a destructive interference.

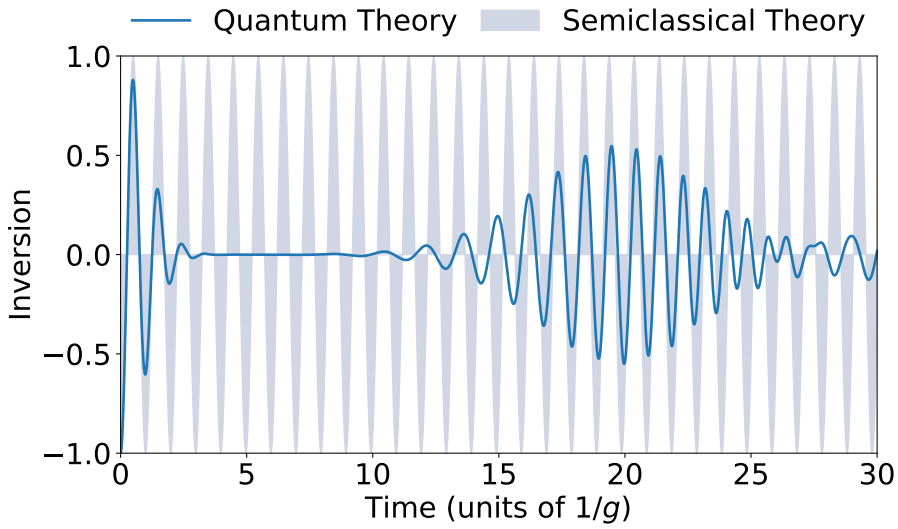

Figure 2.8: Inversion for a coherent state $|\alpha\rangle$ with a mean photon number of 10 according to Eq. (2.80). The shaded area depicts the qualitative result that one would expect from a semiclassical treatment. (After [1])

Dark-State and Loss-Induced Phenomena

3

In this chapter, we consider Λ-type three-level systems (3LS). This system consists of three discrete energy levels $|1\rangle$, $|2\rangle$, and $|3\rangle$, where $|3\rangle$ is the energetically highest level and optical transitions between $|1\rangle$ and $|2\rangle$ are forbidden, while others are allowed. A schematical drawing of a Λ-type 3LS is depicted in Fig. 3.1, where the colored arrows mark the optically allowed transitions.

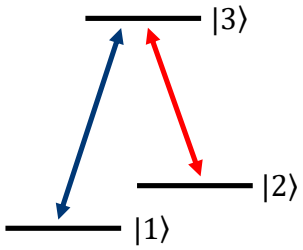

Figure 3.1: Schematical drawing of a Λ-type 3LS. The arrows depict the optically allowed transitions.

Λ-type 3LS describe a variety of material systems ranging from atomic systems to special situations in semiconductor nanostructures. Optically excited semiconductor quantum wells enclosed in a microcavity show a splitting of the 1*s*-exciton into a lower ($|1\rangle$) and an upper polariton state ($|2\rangle$). While optical transition between these states are not allowed, both, however, show an optically allowed transition to the energetically higher 2*p*-exciton state ($|3\rangle$) and thus form a Λ-type 3LS [75, 76]. Another example are negatively charged InAs quantum dots inside of a magnetic field, which show a splitting of the electronic spin eigenstate, since the Landé g-factor is different for the each spin quantum number. The excitation from these electronic spin states ($|1\rangle$ and $|2\rangle$) to an energetically higher located trion state ($|3\rangle$) forms a Λ-type 3LS [77, 78]. Λ-type 3LS are of special interest since they show unique features that allow for special quantum applications such as optical quantum memories that are an important tool for quantum-information processing [79–81], quantum repeaters that contribute to the distribution of quantum states over long distances which is not possible with amplification due to the no-cloning theorem [82], or as nonlinear activation function in an all-optical neural network [83]. A central property that is exploited in these applications is the formation of dark-states in Λ systems, leading to phenomena such as electromagnetically induced transparency (EIT) [84–88] and coherent population trapping (CPT) [89, 90].

We proceed with a demonstration of the equations of motion and will then present results obtained for this system that are based on references [91–93].

3.1 Equations of Motion

We reduce the Hamiltonian from Eq. (2.51) to a Λ-type 3LS, where each transition is excited by single quantum light mode and apply the RWA. This leads to the following Jaynes-Cummings-type Hamiltonian

$$H = \sum_{n=1}^{3} E_n \sigma_{nn} + \sum_{j=1}^{2} \hbar\omega_j \left(b_j^\dagger b_j + \frac{1}{2} \right) + \hbar g \sum_{j=1}^{2} (b_j^\dagger \sigma_{j3} + b_j \sigma_{3j}). \tag{3.1}$$

Here, we assumed that the light-matter coupling is the same for both transitions, so that $g_1^{1,3} = g_2^{2,3} = g$. The DM of this system can in general be written in the following form:

$$\rho = \sum_{\substack{n=1 \\ n'=1}}^{3} \sum_{\substack{k=k'=0 \\ m=m'=0}}^{\infty} \rho_{n',k',m'}^{n,k,m} \left| n,k,m \right\rangle \left\langle n',k',m' \right|, \tag{3.2}$$

where n (n') denotes the electronic state of the material, while k (k') and m (m') denote the Fock state number of the first and second quantum field mode, exciting the $|1\rangle - |3\rangle$ and $|2\rangle - |3\rangle$ transition, respectively. The dynamics is now determined by the von Neumann equation from Eq. (2.57), where we apply a loss to the operator $L = \sqrt{\kappa} b$:

$$\partial_t \rho = \frac{1}{i\hbar} [H, \rho]_- + \mathcal{L}_{\sqrt{\kappa} b}(\rho), \tag{3.3}$$

where κ is the cavity loss rate. To simplify the treatment, we will decompose $\rho_{n',k',m'}^{n,k,m}$ which is a DM element in the Schrödinger picture as follows:

$$\rho_{n',k',m'}^{n,k,m} = p_{n',k',m'}^{n,k,m} \exp\left(\frac{1}{i\hbar} (E_{n,k,m} - E_{n',k',m'}) t \right), \tag{3.4}$$

$$E_{n,k,m} = E_n + \hbar\omega_1 \left(k + \frac{1}{2} \right) + \hbar\omega_2 \left(m + \frac{1}{2} \right) \tag{3.5}$$

where $p_{n',k',m'}^{n,k,m}$ is a DM element in the interaction picture. Numerical simulations in the interaction picture are advantageous, since the fast oscillations that arise due to the non-interacting part of the Hamiltonian do not need to be computed, allowing for larger time steps and shorter computation times. Therefore, we simulate $p_{n',k',m'}^{n,k,m}$ and obtain $\rho_{n',k',m'}^{n,k,m}$ from Eq. (3.4). The vector space of the Fock states has infinite dimensions, which reflects in the summation in Eq. (3.2). One can truncate this summation of k (k') and m (m') at $k_{\max}$ and $m_{\max}$, respectively, which leads to a converged result if they are chosen large enough. The required value depends on the considered quantum state of light and its

mean photon number. The total number of DM elements is $3^2(k_{\max}+1)^2(m_{\max}+1)^2$. This leads to a practical problem for quantum states of light with large mean photon numbers: considering, e.g., two squeezed vacuum states with mean photon numbers of 10 and 100 respectively, a reasonable choice is $k_{\max}=200$ and $m_{\max}=1200$, leading to a total number of $\approx 5.2\cdot 10^{11}$ DM elements, which is beyond any practical realization. This problem can be circumvented by only computing DM elements that are relevant for the observables of interest. For this, we derive an explicit expression for the equations of motion for the DM elements, by substituting Eq. (3.1) and Eq. (3.2) with Eq. (3.4) into Eq. (3.3) and obtain:

$$\begin{aligned}
\partial_t p^{n,k,m}_{n',k',m'}(t) = ig\Big(&p^{n+2,k-1,m}_{n',k',m'}(t)e^{i\Delta_P t}\sqrt{k} + p^{n-2,k+1,m}_{n',k',m'}(t)e^{-i\Delta_P t}\sqrt{k+1} \\
&- p^{n,k,m}_{n'+2,k'-1,m'}(t)e^{-i\Delta_P t}\sqrt{k'} - p^{n,k,m}_{n'-2,k'+1,m'}(t)e^{i\Delta_P t}\sqrt{k'+1}\Big) \\
+ig\Big(&p^{n+1,k,m-1}_{n',k',m'}(t)e^{i\Delta_C t}(1-\delta_{n,1})\sqrt{m} + p^{n-1,k,m+1}_{n',k',m'}(t)e^{-i\Delta_C t}(1-\delta_{n,2})\sqrt{m+1} \\
&- p^{n,k,m}_{n'+1,k',m'-1}(t)e^{-i\Delta_C t}(1-\delta_{n',1})\sqrt{m'} \\
&- p^{n,k,m}_{n'-1,k',m'+1}(t)e^{i\Delta_C t}(1-\delta_{n',2})\sqrt{m'+1}\Big) \\
+\frac{\kappa}{2}\Big[&2p^{n,k+1,m}_{n',k'+1,m'}(t)\sqrt{k+1}\sqrt{k'+1} + 2p^{n,k,m+1}_{n',k',m'+1}(t)\sqrt{m+1}\sqrt{m'+1} \\
&- p^{n,k,m}_{n',k',m'}(t)\big(k+k'+m+m'\big)\Big],
\end{aligned} \tag{3.6}$$

with the optical detunings $\Delta_P = E_3 - E_1 - \hbar\omega_1$ and $\Delta_C = E_3 - E_2 - \hbar\omega_2$. Eq. (3.6) can be numerically solved after specifying the initial condition. Throughout this chapter, we always consider state $|1\rangle$ to be initially full, while the others are empty, leading to the following initial conditions:

$$p^{n,k,m}_{n',k',m'}(t=0) = \delta_{n,1}\delta_{n',1}c_k\tilde{c}_m c_k^*\tilde{c}_m^*, \tag{3.7}$$

where c_k and $\tilde{c}_m$ are the probability amplitudes for the first and second quantum state of light, respectively. The time dynamics of observables is obtained by its expectation value according to Eq. (2.59), so that the electronic population O_n of the n-th level takes the following form:

$$O_n(t) = \langle\sigma_{nn}\rangle = \mathrm{Tr}(\sigma_{nn}\rho) = \sum_{k=0}^{\infty}\sum_{m=0}^{\infty}\rho^{n,k,m}_{n,k,m} = \sum_{k=0}^{\infty}\sum_{m=0}^{\infty}p^{n,k,m}_{n,k,m}. \tag{3.8}$$

Here, we see that only DM elements contribute in which $n=n'$, $k=k'$, and $m=m'$, leading to a total number of $3(k_{\max}+1)(m_{\max}+1)$ DM elements that contribute to the dynamics of O_n, which are less than 10^6 elements for the previous example. The number of differential equations that needs to be solved is approximately three times that number,

taking into account the coherences with $k = k' \pm 1$ and $m = m' \pm 1$ that enter the dynamics. Thus, explicitly calculating the relevant DM elements not only reduces the numerical complexity, but allows for a treatment of quantum states of light with large mean photon numbers in the first place.

In order to get a first impression of the dynamics of such a system, we start with showing simulations of O_n for different initial photon statistics, see Fig. 3.2.

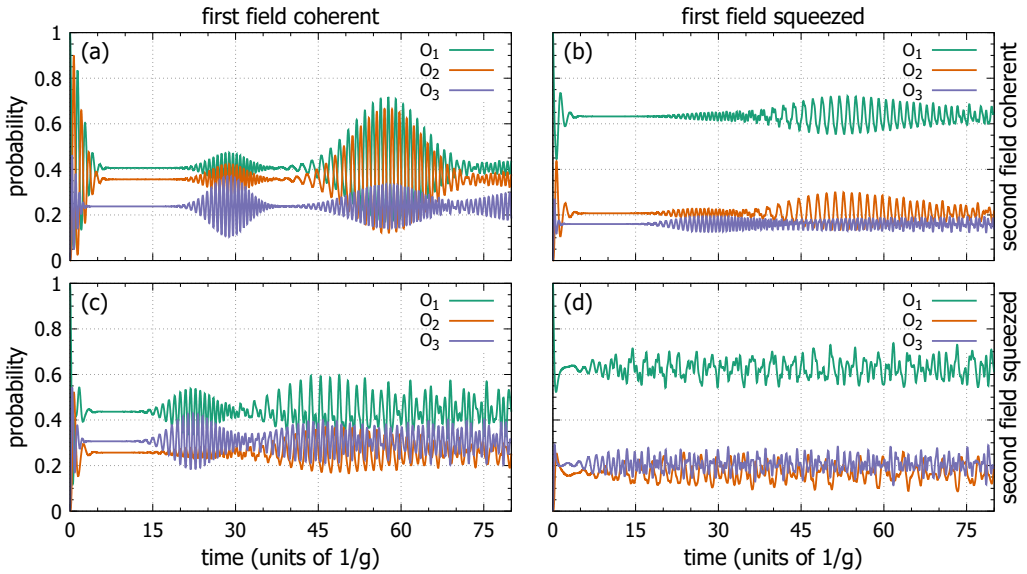

Figure 3.2: Numerical simulation of O_n for n = 1,2,3 and different initial photon statistics with mean photon numbers of 10 in each case. The initial photon statistics of the first and second field is chosen as (a) coherent and coherent state, (b) squeezed vacuum and coherent state, (c) coherent and squeezed vacuum state, (d) squeezed vacuum and squeezed vacuum state, respectively.

The time dynamics for coherent states in Fig. 3.2(a) shows collapses and revivals, which is similar to the behavior discussed in Section 2.4.3. In combination with a squeezed vacuum state as first or second field, shown in Fig. 3.2(b) and Fig. 3.2(c), respectively, the clear collapse and revival features change. In the case of two squeezed vacuum states as shown in Fig. 3.2(d) the dynamics seems rather chaotic and does not follow an obvious pattern.

3.2 Electromagnetically Induced Transparency

As a first application to the Λ-type 3LS, we consider EIT performed with quantum states of light. EIT is a situation in which the $|2\rangle - |3\rangle$ transition is excited with a strong coupling field $|C\rangle$, while the $|1\rangle - |3\rangle$ transition, which is otherwise accompanied by a strong absorption, becomes transparent when excited with a weak probe field $|P\rangle$. This effect is well known from semiclassical treatments and originates from quantum interference between the excitation pathways [86]. EIT is most pronounced for resonant probe fields and decreases for increasing absolute values of the detuning. Therefore, the linear absorption has a minimum at zero detuning and increases for increasing absolute values of the detuning up to a point where the detuning is too large to properly excite the optical transition, so that the absorption decreases. Thus, a typical EIT absorption spectrum has a minimum at zero detuning, surrounded by two peaks.

In a quantum-optical description, however, there is no straightforward definition for a linear absorption, which is why proceed with a consideration of the electronic population. Since the first electronic level is initially occupied, the amount of population that is transferred from the first to the third level is proportional to the absorption of this transition. A measure for the transferred population is the time-averaged population of the third electronic level. This leads to the following definition for the considered measure for absorption:

$$\alpha_{\mathrm{QO}} \equiv \bar{O}_3 = \frac{1}{T}\int_0^T O_3(t')\mathrm{d}t'. \tag{3.9}$$

A schematical drawing of the considered system at $t = 0$ is shown in Fig. 3.3.

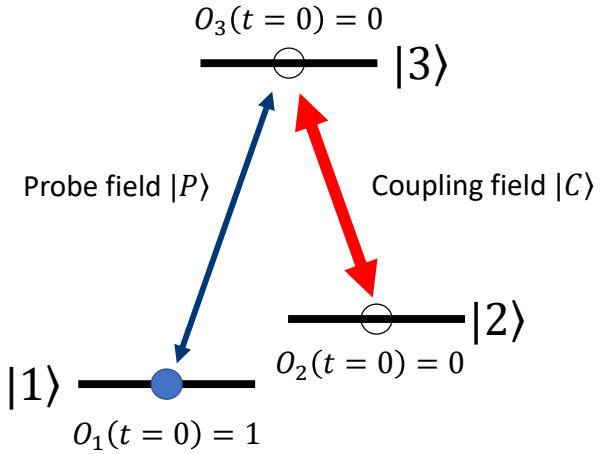

Figure 3.3: Schematical drawing of the system considered for the simulation of EIT spectra

Fig. 3.4 shows numerical simulations of α_{QO} in dependence on the optical detuning of the probe pulse Δ_P for different states of light as described in the legend, where no losses are

applied, i.e. $\kappa = 0$. Here, the mean photon number of the probe pulse is chosen as $N_P = 10$, while the mean photon number of the coupling pulse is chosen as $N_C = 100$ in Fig. 3.4(a), as $N_C = 50$ in Fig. 3.4(b), and as $N_C = 0$ in Fig. 3.4(c), which means that Fig. 3.4(a) and Fig. 3.4(b) show EIT spectra, while Fig. 3.4(c) demonstrates the absorption without any influence of the coupling field.

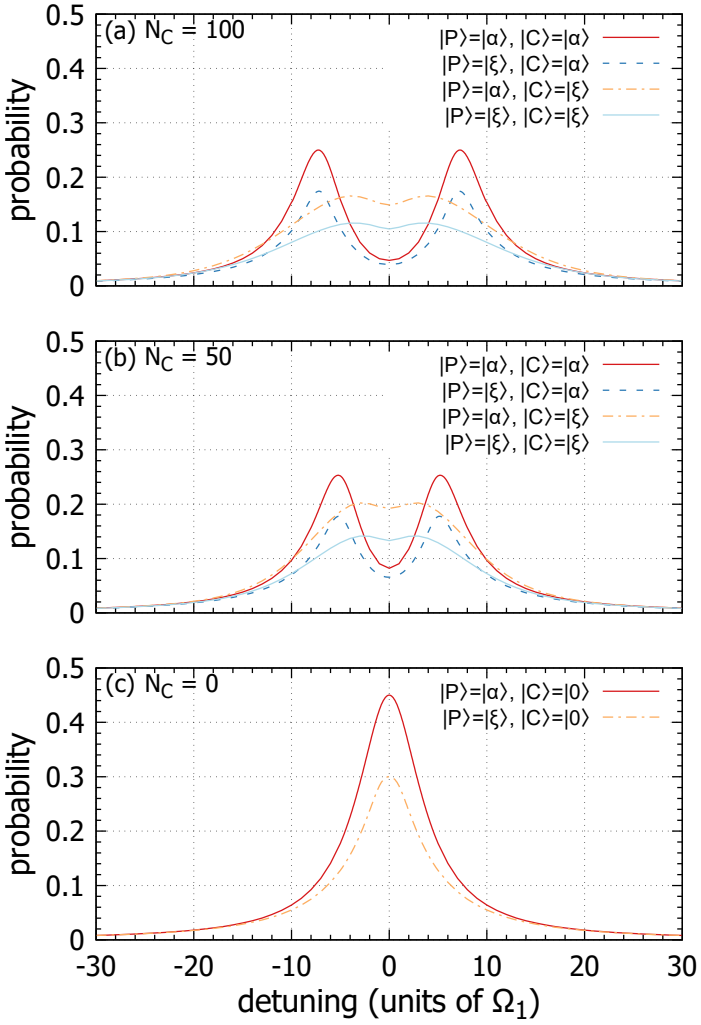

Figure 3.4: Numerical simulations of α_{QO} from Eq. (3.9) in dependence on the detuning Δ_P for different photon statistics depicted in the legend. The probe field has a mean photon number of $N_P = 10$, while the coupling field has a mean photon number of (a) $N_C = 100$, (b) $N_C = 50$, and (c) $N_C = 0$. The detuning is given in units of $\Omega_1 = \sqrt{2}g$ and therefore is proportional to the light-matter coupling g. Taken from [91].

We see that the EIT spectra show the expected result, i.e., a minimum at zero detuning

surrounded by two peaks. A special feature is found in the case of squeezed vacuum states as probe field, i.e. $|P\rangle = |\xi\rangle$, as it leads to less absorption than a coherent state, despite having the same mean photon number, which is equivalent to a more efficient EIT. This behavior can be understood from the photon statistics of squeezed vacuum states, as they show a large contribution in the vacuum component, which cannot promote electrons. This is also demonstrated in Fig. 3.4(c), where a squeezed state $|\xi\rangle$ with a mean photon number of 10 leads to less absorption than coherent state $|\alpha\rangle$ with the same mean photon number.

The application of a squeezed vacuum state as coupling field leads to a different lineshape of the EIT spectra, which can be understood by considering the effective splitting given by the dressed states that form during the light-matter interaction. The position of the maxima Ω_g can be estimated with

$$\Omega_g \approx \pm g \sum_{m=0}^{\infty} |c_m^C|^2 \sqrt{m} = \pm \frac{\Omega_1}{\sqrt{2}} \sum_{m=0}^{\infty} |c_m^C|^2 \sqrt{m}. \tag{3.10}$$

The values for Ω_g obtained from the simulation shown in Fig. 3.4 and from Eq. (3.10) are listed in Table 3.1. We see that the values are in a good agreement for coherent states $|\alpha\rangle$

coupling field	Ω_g (simulated)	Ω_g (Eq. (3.10))
$\|C\rangle = \|\alpha\rangle$, $N_C = 100$	$\pm 7.2\Omega_1$	$\pm 7.06\Omega_1$
$\|C\rangle = \|\alpha\rangle$, $N_C = 50$	$\pm 5.2\Omega_1$	$\pm 4.99\Omega_1$
$\|C\rangle = \|\xi\rangle$, $N_C = 100$	$\pm 3.6\Omega_1$	$\pm 5.58\Omega_1$
$\|C\rangle = \|\xi\rangle$, $N_C = 50$	$\pm 2.5\Omega_1$	$\pm 3.91\Omega_1$

Table 3.1: The maxima Ω_g of the EIT spectra for different coupling fields are listed obtained from both, the numerical simulation shown in Fig. 3.4 and from the estimation Eq. (3.10)

and that Eq. (3.10) predicts the general trend of Ω_g found in the simulation. The value is slightly underestimated, since the probe field is not taken into account. The agreement for squeezed vacuum states $|\xi\rangle$, however, is worse, since the peaks show a significant overlap as can be seen in Fig. 3.4(a) and Fig. 3.4(b). This overlap between the two peaks leads a significant decrease in the positon of their maxima, which is why Eq. (3.10) provides a strong overestimation. Regardless, Eq. (3.10) provides a qualitative understanding of the peak position and predicts the location of the maxima at smaller detunings for squeezed vacuum states.

Summarizing, we simulate EIT spectra with quantum states of light. Here, we demonstrate that the non-classical squeezed vacuum state enhances the EIT when used as a probe field. In addition, we show that the choice of the coupling field significantly alters the form of the EIT spectra, which can be understood with the dressed state picture.

3.3 Classical and Quantum Polarization

Until now we only considered the electronic population. Another relevant quantity in the context of light-matter interaction, however, is the polarization that leads to the occupation of the electronic states in the first place. A polarization can be assigned to each optical transition, where we will focus on the $|1\rangle - |3\rangle$ transition. From a semiclassical perspective, the polarization is defined as expectation value of the dipole moment from Eq. (2.49), where we only consider the operator σ_{13}:

$$P_{31}^{C} = \langle \sigma_{13} \rangle = \mathrm{Tr}(\sigma_{13}\rho) = \sum_{k=0}^{\infty}\sum_{m=0}^{\infty} \rho_{1,k,m}^{3,k,m} = \exp\left(-\frac{i}{\hbar}(E_3 - E_1)t\right) \sum_{k=0}^{\infty}\sum_{m=0}^{\infty} p_{1,k,m}^{3,k,m}. \tag{3.11}$$

In this definition, however, the field information is not incorporated. This has striking drawbacks, as we will demonstrate in the following. From the equations of motion Eq. (3.6) one can conclude that $\rho_{1,k,m}^{3,k,m}$ is coupled to $\rho_{1,k+1,m}^{1,k,m}$. Since we assume the first level to be initially populated, a finite $\rho_{1,k,m}^{3,k,m}$ can only be obtained if $\rho_{1,k+1,m}^{1,k,m}$ is finite initially. According to the initial condition in Eq. (3.7)

$$\rho_{1,k,m}^{1,k+1,m}(t=0) \propto c_{k+1}c_k^*. \tag{3.12}$$

The product $c_{k+1}c_k^*$ expresses a correlation between photon numbers $k+1$ and k and is required to be non-zero to obtain a finite P_{31}^{C}. However, one can show that $c_{k+1}c_k^*$ is zero for a lot of relevant quantum states of light including squeezed vacuum states $|\xi\rangle$, Fock states $|n\rangle$, even and odd cat states $|\mathrm{cat}_e\rangle \propto |\alpha\rangle + |-\alpha\rangle$ and $|\mathrm{cat}_o\rangle \propto |\alpha\rangle - |-\alpha\rangle$, and thermal states. Thus, the aforementioned quantum states of light do not excite a classical polarization but still lead to electronic population. A similar conclusion for thermal states in the context of the generation of exciton population was done in Ref. [8]. In contrast, the coherent state $|\alpha\rangle$ which is the most classical analog does lead to a classical polarization P_{31}^{C}. Fig. 3.5 shows numerical simulations of the classical polarization P_{31}^{C} for different combinations of initial photon statistics. The gap frequency $\omega_{31} = (E_3 - E_1)/\hbar$ was set to $100\Omega_1$ for this purpose and only the imaginary part is shown, since the real part is qualitatively the same due to the fast oscillation. One can see that P_{31}^{C} is only finite when the $|3\rangle - |1\rangle$ transition is excited with a coherent state, which results from the aforementioned property.

We conclude that a proper definition for the polarization in a quantum-optical treatment must include field operators. In general, one can formulate a polarization operator that carries the complete information of the exciting field:

$$P_{31} = \sum_{m=0}^{\infty} \rho_{1,k',m}^{3,k,m} \, |k'\rangle \langle k| \, . \tag{3.13}$$

In our case, however, the consideration of an absorption and an emission of a single photon is sufficient, which is why we only consider $k' = k+1$, leading to our definition of the

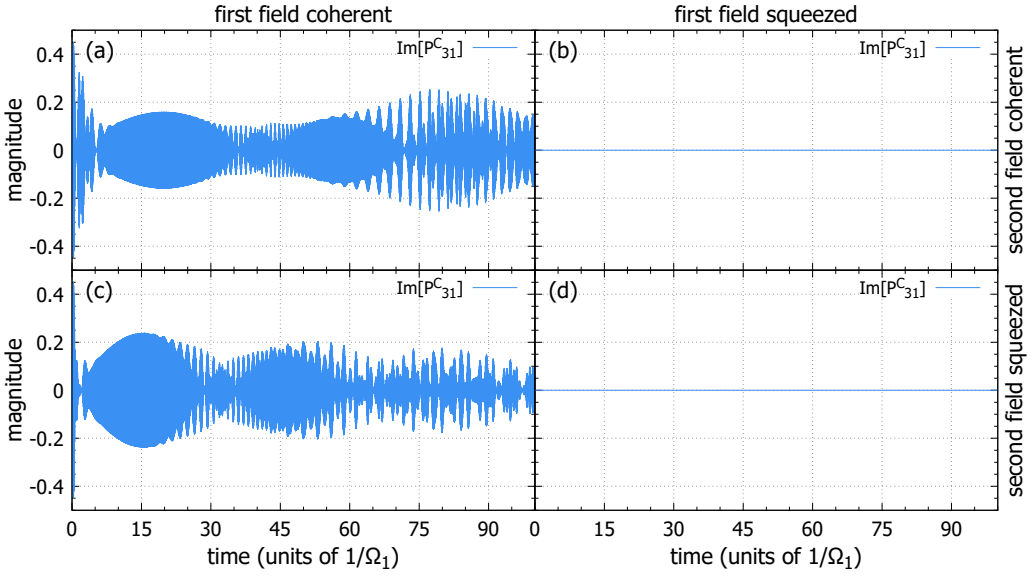

Figure 3.5: Time dynamics of the classical polarization P_{31}^{C} for different initial photon statistics with a mean photon number 10 each. The initial photon statistics of the first and second field is chosen as (a) coherent and coherent state, (b) squeezed vacuum and coherent state, (c) coherent and squeezed vacuum state, (d) squeezed vacuum and squeezed vacuum state, respectively. Taken from [91].

quantum polarization that is suitable for the analysis of the current problem

$$P_{31}^{Q} = \sum_{k=0}^{\infty}\sum_{m=0}^{\infty} \rho_{1,k+1,m}^{3,k,m} = \exp\left(-\frac{i}{\hbar}\Delta_P t\right) \sum_{k=0}^{\infty}\sum_{m=0}^{\infty} p_{1,k+1,m}^{3,k,m}. \tag{3.14}$$

In contrast to the previous case, the quantum polarization is finite for all quantum states of light that lead to an optical excitation. Fig. 3.6 demonstrates the same as in Fig. 3.5, but for the quantum polarization P_{31}^{Q} instead. In contrast to the previous case, we see finite magnitudes in all cases. Furthermore, the dynamics of the quantum polarization behaves similar to the population dynamics, i.e., it shows the collapse and revival behavior for coherent states and a rather chaotic behavior for squeezed vacuum states, as demonstrated in Fig. 3.2. We conclude that the quantum polarization P_{31}^{Q} seems to be a more promising measure when studying polarizations in the context of quantum-optical excitations.

In the following, we demonstrate the applicability of the quantum polarization by using it to simulate the dispersion and absorption of a quantum-optical excitation. For this, we consider the time averaged real and imaginary part in dependence on the detuning, obtained in a similar way as in Eq. (3.9). The real part corresponds to the dispersion and the imaginary part to the absorption.

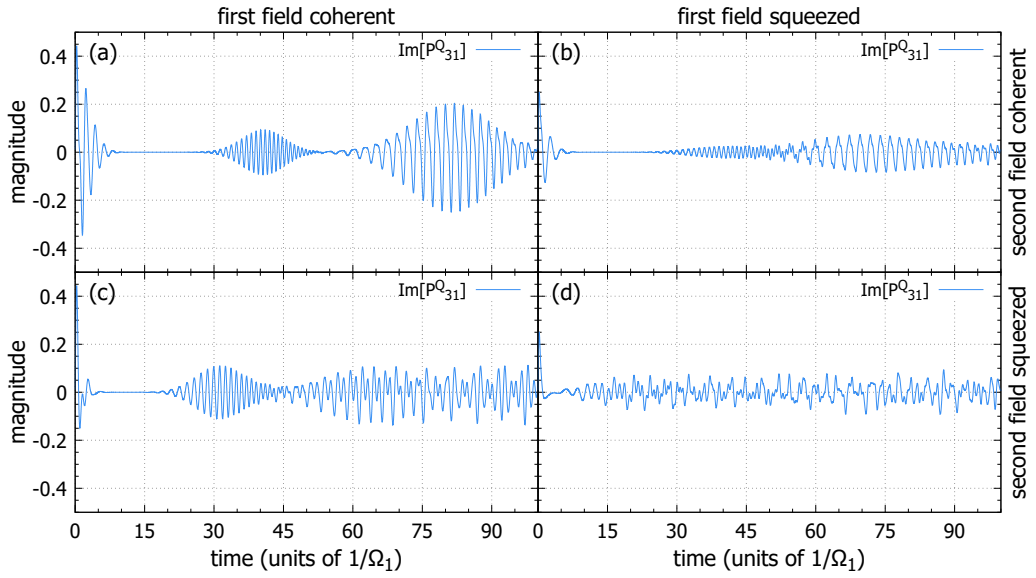

Figure 3.6: Time dynamics of the quantum polarization P_{31}^{Q} for different initial photon statistics with a mean photon number 10 each. The initial photon statistics of the first and second field is chosen as (a) coherent and coherent state, (b) squeezed vacuum and coherent state, (c) coherent and squeezed vacuum state, (d) squeezed vacuum and squeezed vacuum state, respectively. Taken from [91].

Besides the numerical treatment, we also consider an approximate analytical solution that can be derived in the perturbative limit for weak probe fields:

$$P_{31,A}^{Q}(\Delta_P) = \sum_{k=0}^{\infty}\sum_{m=0}^{\infty} \frac{\Omega_1 \Delta_P \sqrt{\frac{k+1}{2}} |c_{k+1}|^2 |\tilde{c}_m|^2}{\Omega_1^2(\frac{m+1}{2}) - \Delta_P^2 - i\Delta_P \tilde{r}_{1,3}}, \tag{3.15}$$

where $\tilde{r}_{1,3}$ was introduced within this derivation to describe a decay of the nondiagonal matrix elements. This allows for a direct comparison between the numerically computed $P_{31,N}^{Q}(\Delta_P)$ and the analytically obtained $P_{31,A}^{Q}(\Delta_P)$. We start with the consideration of two coherent states with mean photon numbers of $N_P = 10$ and $N_C = 100$. For the numerical treatment, we perform the time averaging until $t\Omega_1 = 20$ which is after the first collapse of the dynamics. Fig. 3.7(a) shows the real and imaginary parts for both, the numerically computed $P_{31,N}^{Q}$ and the analytical solution $P_{31,A}^{Q}$ from Eq. (3.15). We see that both treatments are in a good agreement and yield the expected result from a semiclassical treatment, as e.g. shown in [5]. In our case, however, the approach can be extended towards non-classical light. We demonstrate this by repeating the same calculation for two squeezed vacuum states, see Fig. 3.7(b). In this case, we see a worse agreement between the numerical and the analytical curves, which, however, are still in a qualitative agreement, while the peaks at $\Delta_P = 0$ are more pronounced for the analytical solution. While the real parts behave similar, $\mathrm{Im}[\mathrm{P}_{31,\mathrm{N}}^{\mathrm{Q}}]$ shows an oscillatory behavior that arises from the fact that the time-averaged imaginary part approaches zero for increasing time intervals and a finite value obtained

from a finite time interval therefore cannot be converged and depends on the time interval. In contrast, the analytical solution $\mathrm{Im}[\mathrm{P}^{\mathrm{Q}}_{31,\mathrm{A}}]$ does not show this oscillations and therefore seems to lead to a more reasonable result. A way to verify the suitability of this method is to compare the obtained absorption spectra $\mathrm{Im}[P^{Q}_{31,A}]$ with the EIT spectra obtained in the previous section show in Fig. 3.4, as they are in a qualitative agreement.

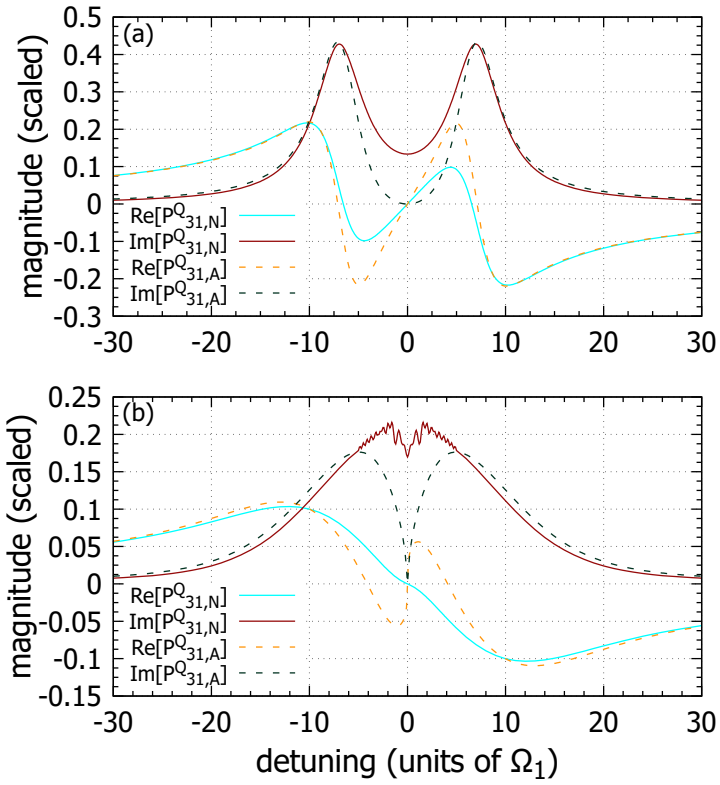

Figure 3.7: Time-avergaed real and imaginary part of the quantum polarization obtained from both, a numerical treatment ($P^{Q}_{31,N}$) and the analytical solution Eq. (3.15) ($P^{Q}_{31,A}$). For the analytical solution, $\tilde{r}_{1,3} = 5\Omega_1$ is chosen. The probe and coupling field are chosen as (a) two coherent states and (b) two squeezed vacuum states with mean photon numbers of $N_P = 10$ and $N_C = 100$. Taken from [91].

In conclusion, we defined a new measure for the description of the polarization for quantum-optical excitations, the quantum polarization P^{Q}_{31}, which can successfully describe the excitation with non-classical light.

3.4 Control of Steady States with Cavity Losses

In the previous sections we considered the lossless population and polarization dynamics, corresponding to the case of high-quality cavities in which loss mechanisms are negligible on short time scales. In this section, however, we consider the bad cavity limit in which the cavity loss ratio κ is dominant while other mechanisms are negligible and demonstrate that cavity losses can be used as an advantage by controlling steady states with them. Such a situation is a realistic assumption for quantum dots, as they show large dephasing times, leading to cavity losses being dominant for lossy cavities [77]. There are also atomic systems in which this condition applies [94, 95]. The bad cavity limit has been widely studied over recent centuries. Besides of theoretical studies on TLS [96], the bad cavity limit was used to demonstrate laser cooling [97]. The bad cavity limit is of special interest for applications in quantum information, such as in the realization of an optical storage [98] and for the processing of quantum information [99–101]. Further applications include the entangling of atoms [102], the formation of new types of eigenmodes [103], quantum Zeno-type effects [104], and the formation of dark states [105]. Moreover, cavities with a larger Q-factor allow to efficiently support inhomogeneous broadened samples [106, 107].

For the present treatment, we restrict our analysis to resonant excitations, i.e., $\Delta_P = \Delta_C = 0$. In addition, we consider the second light state to be a vacuum state $|0\rangle$, while the first one is an arbitrary quantum state of light $|\Psi_1\rangle$. A schematical illustration of the considered system is depicted in Fig. 3.8.

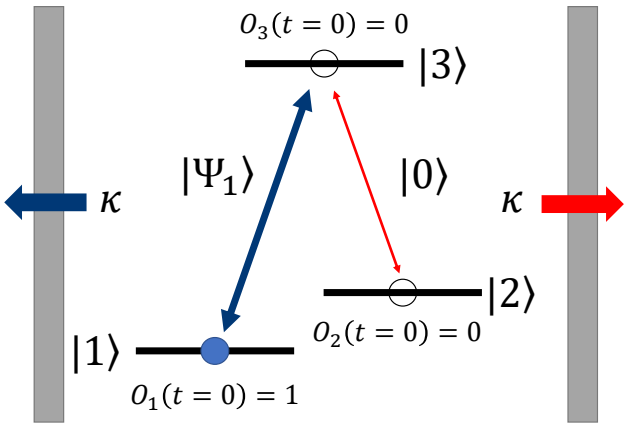

Figure 3.8: Schematical illustration of the system considered for the simulations performed in this section

In this section, we work with the following rescalings:

$$\tilde{\kappa} = \frac{\kappa}{g}, \qquad \tilde{t} = tg, \tag{3.16}$$

so that dependencies will always be shown in terms of the dimensionless quantities $\tilde{\kappa}$ and $\tilde{t}$. Fig. 3.9 shows the time dynamics of the electronic populations for $|\Psi_1\rangle = |\alpha\rangle$ with a mean photon number of $N = 10$ with cavity losses ($\tilde{\kappa} = 0.3$) and without cavity losses ($\tilde{\kappa} = 0$).

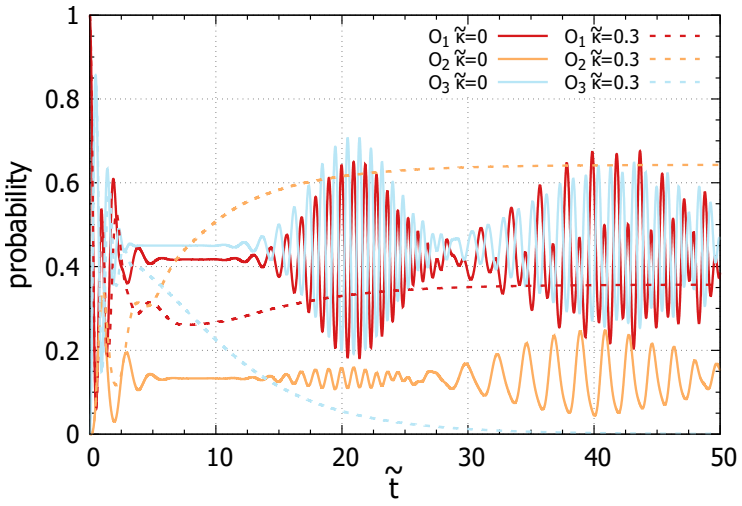

Figure 3.9: Population dynamics O_n for a coherent state $|\alpha\rangle$ with a mean photon number of 10 as first field and the vacuum state as second field. The solid lines show the lossless case ($\tilde{\kappa} = 0$) and the dashed lines show the case with cavity losses ($\tilde{\kappa} = 0.3$). Taken from [92].

The time dynamics without cavity losses shows collapses and revivals, which is similar to the behavior shown in Fig. 3.2 and discussed for a TLS in Section 2.4.3. Since the second field is chosen as the vacuum state, it is to be expected that population of the second level remains comparably small over time. This, however, is different when cavity losses are applied. In this case, a steady state forms in which the value of O_2 surpasses both, the values of O_1 and O_3. This indicates a mechanism that allows to control the steady state population by using cavity losses, which will be discussed in this section.

3.4.1 Analysis of the Equations of Motion

We proceed with an analysis of the involved processes, where we start by quantifying the steady-state values. The time dynamics of the electronic population is computed according to Eq. (3.8). For the limit $\tilde{t} \to \infty$, however, the cavity losses have led to the destruction of all photons and only DM elements with Fock state indices $k = 0$ and $m = 0$ can contribute.

Thus, the steady-state populations can be written according to

$$O_{1,\mathrm{st}} = O_1(\tilde{t} \to \infty) = p^{1,0,0}_{1,0,0}(\tilde{t} \to \infty), \tag{3.17}$$

$$O_{2,\mathrm{st}} = O_2(\tilde{t} \to \infty) = p^{2,0,0}_{2,0,0}(\tilde{t} \to \infty). \tag{3.18}$$

The corresponding equations of motion have the following form:

$$\partial_{\tilde{t}} p^{1,0,0}_{1,0,0} = \tilde{\kappa}\left[p^{1,1,0}_{1,1,0} + p^{1,0,1}_{1,0,1}\right], \tag{3.19}$$

$$\partial_{\tilde{t}} p^{2,0,0}_{2,0,0} = \tilde{\kappa}\left[p^{2,0,1}_{2,0,1} + p^{2,1,0}_{2,1,0}\right]. \tag{3.20}$$

For clarity, we continue the discussion for the $n = n' = 1$ case (Eq. (3.17)), since it is the same for the $n = n' = 2$ case (Eq. (3.18)). Eq. (3.19) reveals that $p^{1,0,0}_{1,0,0}$ is driven by $p^{1,1,0}_{1,1,0}$ and $p^{1,0,1}_{1,0,1}$. The driving terms on the right-hand side have an import difference: $p^{1,1,0}_{1,1,0}$ describes a state of the system in which the first electronic level is occupied, while the first field is a single photon Fock state, whichs allows for an optical excitation. Therefore, $p^{1,1,0}_{1,1,0}$ couples to other DM elements, as can be seen by its equation of motion:

$$\partial_{\tilde{t}} p^{1,1,0}_{1,1,0} = i(p^{3,0,0}_{1,1,0} - p^{1,1,0}_{3,0,0}) + \tilde{\kappa}\left[-p^{1,1,0}_{1,1,0} + 2p^{1,2,0}_{1,2,0} + p^{1,1,1}_{1,1,1}\right]. \tag{3.21}$$

In contrast, $p^{1,0,1}_{1,0,1}$ does not describe an optical promotion of electrons, since the first field has no photons. The corresponding equation of motion reads:

$$\partial_{\tilde{t}} p^{1,0,1}_{1,0,1} = \tilde{\kappa}\left[p^{1,1,1}_{1,1,1} + p^{1,0,2}_{1,0,2}2 - p^{1,0,1}_{1,0,1}\right]. \tag{3.22}$$

Similar to $p^{1,0,0}_{1,0,0}$ from Eq. (3.19), $p^{1,0,1}_{1,0,1}$ from Eq. (3.22) can only change during the time-evolution if $\tilde{\kappa} > 0$.

From this example, we extract a more general distinction between DM elements. We define non-interacting element (NIE) and interacting elements (IE) as follows: $p^{n,k,m}_{n',k',m'}$ is a NIE if $\partial_{\tilde{t}} p^{n,k,m}_{n',k',m'} = 0|_{\tilde{\kappa}=0}$ and an IE if $\partial_{\tilde{t}} p^{n,k,m}_{n',k',m'} \neq 0|_{\tilde{\kappa}=0}$. The NIE that are relevant for the present dynamics are given by $p^{1,0,m}_{1,0,m}$ or $p^{2,k,0}_{2,k,0}$ that are determined by the following equations of motion:

$$\partial_{\tilde{t}} p^{1,0,m}_{1,0,m} = \tilde{\kappa}\left[p^{1,1,m}_{1,1,m} + p^{1,0,m+1}_{1,0,m+1}(m+1) - p^{1,0,m}_{1,0,m}m\right], \tag{3.23}$$

$$\partial_{\tilde{t}} p^{2,k,0}_{2,k,0} = \tilde{\kappa}\left[p^{2,k,1}_{2,k,1} + p^{2,k+1,0}_{2,k+1,0}(k+1) - p^{2,k,0}_{2,k,0}k\right]. \tag{3.24}$$

From the right-hand side, we see that a NIE is always driven by a NIE and an IE, both of higher Fock state index and has a loss term proportional to its own Fock state index which is consistent with the identification in Eq. (3.17) and Eq. (3.18). From this we can conclude that all NIE elements of the form $p^{1,0,m}_{1,0,m}$ contribute to $O_{1,\mathrm{st}}$ and all NIE of the form $p^{2,k,0}_{2,k,0}$ contribute to $O_{2,\mathrm{st}}$. To get an understanding of the simulation shown Fig. 3.9 one must consider that the number of contributing NIE $p^{2,k,0}_{2,k,0}$ is given by the number of relevant

Fock state indices k of the initial photon statistics of the first field. Qualitatively, a bright first field leads to many NIE of the form $p^{2,k,0}_{2,k,0}$, while a vacuum state as second field only allows for $p^{1,0,0}_{1,0,0}$. Thus, the asymmetry in the exciting fields also leads to an asymmetry in the electronic population, but in such a way that the initially unoccupied second electronic state that is excited with a vacuum state shows the highest population.

This behavior can be attributed to the physical process that the promotion of an electron over the $|1\rangle - |3\rangle$ transition can result in a relaxation into the state $|2\rangle$ under the emission of a photon which is immediately destroyed by cavity losses so that the electron in the second level cannot be promoted again. The NIE exactly capture this process and represent the probability of such an event. However, it is clear that this does not work the same for all loss rates $\tilde{\kappa}$, which we will investigate in the next subsection.

3.4.2 Simulations for Different Photon Statistics and Loss Rates

We proceed with simulations of $O_{2,\mathrm{st}}$ in dependence on $\tilde{\kappa}$ for different initial photon statistics of the first field. Fig. 3.10(a) shows such simulations for a coherent state $|\alpha\rangle$, a Fock state $|n\rangle$, and a squeezed vacuum state $|\xi\rangle$ with a mean photon number of 10 each and Fig. 3.10(b) is a zoom of Fig. 3.10(a) that makes the difference in the curves more visible. It is clearly visible that the squeezed vacuum leads to a smaller $O_{2,\mathrm{st}}$ for all $\tilde{\kappa}$. This originates in the strong contribution at $k = 0$ in the squeezed vacuum state (e.g. shown in Fig. 2.5), leading to a strong initial contribution in $p^{1,0,0}_{1,0,0}$ that cannot be reverted. In contrast, the vacuum component for a coherent state is very small and zero for a Fock state.

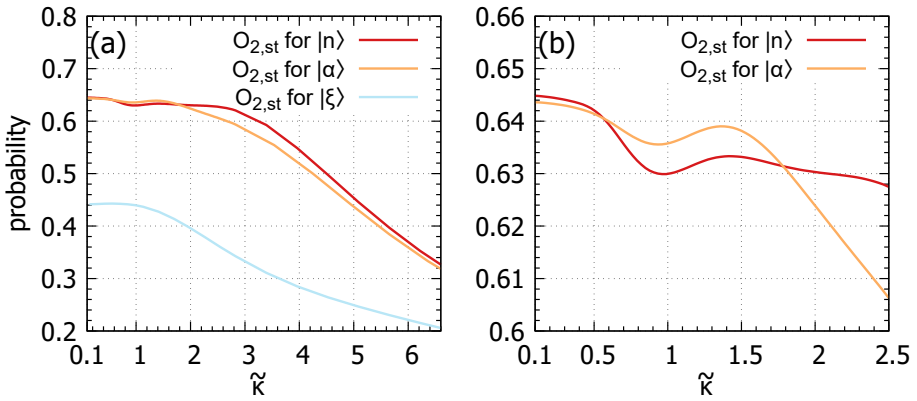

Figure 3.10: Steady-state probability $O_{2,\mathrm{st}}$ in dependence on $\tilde{\kappa}$ for different initial photon statistics of the first field, while the second field initially is a vacuum state. The considered initial photon statistics are (a) a Fock state, a coherent state, and a squeezed vacuum state with a mean photon number of 10 each (b) same as in (a) but without the squeezed vacuum state and for a smaller interval for $\tilde{\kappa}$. Taken from [92].

For a further analysis, the loss rates κ are divided in different regimes:

- small κ ($\tilde{\kappa} \ll 1$)

- intermediate κ ($\tilde{\kappa}$ and the light-matter coupling are in the same order of magnitude)
- high κ ($\tilde{\kappa} \gg 1$)

In the regime of small κ the time dynamics of the populations shows several Rabi oscillations, so that the physical process that was described in the previous subsection applies, while the value of $O_{2,\mathrm{st}}$ mainly depends on the applied photon statistics.

The regime of high κ shows a clear trend of a decreasing $O_{2,\mathrm{st}}$. In this case, the system has not performed a full Rabi cycle and therefore, generally speaking, the photons are destroyed faster than electrons can be promoted. Thus, for high κ, the system tends to remain in its initial electronic state. In Fig. 3.10(b) one can see that a coherent state leads to a faster decrease of $O_{2,\mathrm{st}}$ than for a Fock state. This can be led back to the contribution of fewer-number Fock states in the coherent state, which the Fock state does not have. We conclude that in this regime, the value of $O_{2,\mathrm{st}}$ is determined by both, the photon statistics and the exact value of $\tilde{\kappa}$. The importance of the photon statistics, however, decreases for increasing $\tilde{\kappa}$ since the photon statistics becomes irrelevant if all photons are destroyed immediately.

The third regime of intermediate $\tilde{\kappa}$ cannot be categorized as clear as the other two regimes, since the dynamics is damped within the first few Rabi cycles and thus the exact value of $\tilde{\kappa}$ is important, which determines at which phase of the Rabi oscillation the damping occurs. The behavior can be seen in Fig. 3.10(b) in the range of $\tilde{\kappa} \approx 1$, where no clear trend can be seen and the curves even show inflection points.

In conclusion, both, the initial photon statistics and the exact value of κ is relevant for the obtained steady-state probabilities, which allows for a more precise tailoring when applying this method.

3.5 Conclusions

In this chapter, we consider a Λ-type 3LS that is pre-excited by two quantum light modes. We demonstrate that the numerical complexity can be drastically reduced by specifically choosing the DM elements that are relevant for the observables of interest, which allows the efficient treatment of large mean photon numbers.

We proceed with the simulation of EIT within the quantum-optical regime and conclude that the non-classical squeezed vacuum state enhances the efficiency of EIT when used as probe field. Afterwards, we consider the classical polarization and conclude that it is not suitable for the description of most quantum-optical excitations. Therefore, we introduce a new quantity, the quantum polarization, and demonstrate its applicability by using it to model the absorption and dispersion for the excitation with coherent and squeezed vacuum states, which is in a qualitative agreement with the EIT spectra from the population-dynamics approach. We conclude that the quantum polarization is suitable for a versatile analysis of quantum excitations. Finally, we study the light-matter interaction

for lossy cavities and demonstrate that one can take advantage of the cavity loss rate κ to obtain desired steady states. We obtain an understanding of this mechanism by closely considering the equations of motion and simulated steady states for different initial photon statistics and different cavity loss rates κ. This proposed mechanism is suitable to control steady states since it only depends on the photon statistics of the applied field and the design of the cavity and does not require an initial preparation of the system.

Population Dynamics of Two-Band Models

4

The material system that we modeled so far is a suitable description for special situations in which excitonic resonances are optically pre-excited or semiconductor nanostructures are doped and subjected to a magnetic field. In the most practical situations, however, one is interested in the optical and electric properties of intrinsic semiconductor nanostructures that are initially in their electronic ground state. To achieve a proper description for such a situation, one needs to consider the band structure of a semiconductor nanostructure. Here, we restrict our investigation to two-band models that are initially excited by a single-mode quantum field inside of an optical microcavity, where we neglect many-body interactions, such as electron-electron and electron-photon interactions [1], since we want to focus on the quantum-optical description as the main layer of complexity. We will consider quasi-1D and quasi-2D semiconductors, corresponding to quantum wires and quantum wells, respectively. The content in this chapter is partly based on Ref. [108] and mainly on Ref. [109], which is currently submitted.

4.1 Theoretical Model

In contrast to the previous considerations, the present scenario requires a quantum light mode to excite many few-level systems. We assign a TLS to each k-point transition of the continuous k-space in which the electronic band structure is described. Fig. 4.1 shows a schematical drawing of a two-band model, where the approximate description with TLS is indicated.

Eq. (2.51) does not cover this case, as it describes the interaction between a single material system with several quantum light modes. The extension, however, is straightforward, and just requires to increase the dimension of the basis states. The interaction between N identical TLS and a single quantum light mode is known as the Tavis-Cummings model [110]. We, however, consider the interaction between N TLS that follow a given band structure that are excited by a quantum field mode. We start with a derivation of the equations of motion for arbitrary band structures, which we will later specify for a proper description of semiconductor nanostructures. Neglecting the Coulomb interaction and the coupling to phonons, the Hamiltonian takes the following form [1]:

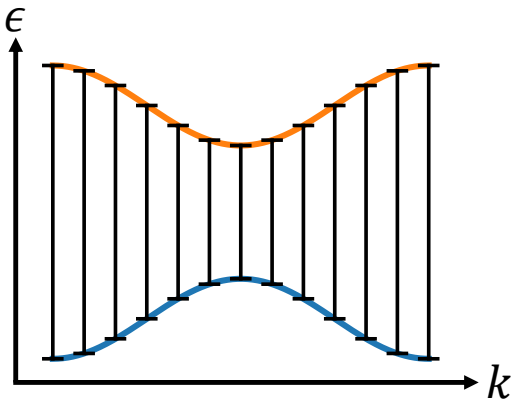

Figure 4.1: Schematical drawing of an electronic band structure that connects the energy ϵ and the momentum $\boldsymbol{k}$ of an electron, represented by a single valence (blue curve) and a single conduction band (orange curve). Several TLS transitions are depicted to indicate the approximate description of such a band structure in the continuous k-space.

$$H = \sum_{\boldsymbol{k}} \left[\epsilon^{v}_{\boldsymbol{k}} a^{\dagger}_{v,\boldsymbol{k}} a_{v,\boldsymbol{k}} + \epsilon^{c}_{\boldsymbol{k}} a^{\dagger}_{c,\boldsymbol{k}} a_{c,\boldsymbol{k}}\right] + \hbar\nu\left[b^{\dagger}b + \frac{1}{2}\right] - \sum_{\boldsymbol{k}} M_{\boldsymbol{k}}(b^{\dagger} a^{\dagger}_{v,\boldsymbol{k}} a_{c,\boldsymbol{k}} + b a^{\dagger}_{c,\boldsymbol{k}} a_{v,\boldsymbol{k}}). \quad (4.1)$$

Here, we no longer work with the notation of transition operators σ_{ij}, but introduced fermionic creation and annihilation operators $a^{\dagger}_{\gamma,\boldsymbol{k}}$ and $a_{\gamma,\boldsymbol{k}}$, respectively, that describe the creation and annihilation of an electron with momentum $\boldsymbol{k}$ in the band γ. $\epsilon^{\gamma}_{\boldsymbol{k}}$ denotes the energy of the γ-band for a momentum $\boldsymbol{k}$, which specifies the band structure. In the present analysis, we will restrict ourselves to a single valence and a single conduction band, which means that γ can either be v for the valence band or c for the conduction band. $M_{\boldsymbol{k}}$ corresponds to g^{ij}_{k} from Eq. (2.52), but was assigned to a new symbol to distinguish between the treatment of a single TLS and N TLS. We neglect the k-dependence of the light-matter coupling: $M_{\boldsymbol{k}} = M$. The resulting dynamics must not depend on the discretization of the band, i.e., on the number of k-points N, as long as N is sufficiently large to model the k-space continuum. To ensure that, the total oscillator strength $\mathcal{M}$ must be kept constant. Since

$$\mathcal{M} \sim \sum_{j=1}^{N} |M_{k_j}|^2 = \sum_{j=1}^{N} |M|^2 = N|M|^2, \quad \mathcal{M} = \text{const.} \Rightarrow M = M_0/\sqrt{N}, \quad (4.2)$$

where k_j denotes the discretization of $\boldsymbol{k}$ in terms of integers j. We see that M, which corresponds to the light-matter coupling between the light mode and a single k-point transition, depends N, which is why M_0 is considered as the relevant quantity instead, which is directly proportional to $\mathcal{M}$ and does not depend on the discretization. In reality,

however, the coupling strength of a single transition cannot depend on the discretization. Mathematically, the additional factor of $1/\sqrt{N}$ is a consequence from preserving the commutation relation for the creation and annihilation operator for different choices of discretization of the continuous k-space [111].

In the following, we want to formulate explicit equations of motion that describe the dynamics of such a system. Since all combinations of k-points being excited or not must be taken into account, it is convenient to introduce the compound index (γ) as:

$$(\gamma) = \gamma_1, \gamma_2, ..., \gamma_N. \tag{4.3}$$

Here, γ_j denotes the state of the electron with momentum k_j, which can either be in the valence band ($\gamma_j = v$) or in the conduction band ($\gamma_j = c$). To denote changes applied to this compound index, we introduce the following notation:

$$\gamma_1, \gamma_2, ..., \gamma_{j-1}, \gamma_j \pm 1, \gamma_{j+1}, ..., \gamma_N = (\gamma|\gamma_j \pm 1), \tag{4.4}$$

$$\gamma_1, \gamma_2, ..., \gamma_{j-1}, \tilde{\gamma}, \gamma_{j+1}, ..., \gamma_N = (\gamma|\gamma_j = \tilde{\gamma}), \tag{4.5}$$

$$v, v, ..., v, v = (v), \tag{4.6}$$

where $\gamma_j \pm 1$ is meant in such a way that "$v + 1 = c$" and "$c - 1 = v$". Eq. (4.4) denotes the promotion (+1) or demotion (−1) of an electron in the state γ_j, while Eq. (4.5) denotes that γ_j is set to a given state $\tilde{\gamma}$. Eq. (4.6) is a notation for the state in which all electrons the valence band, which corresponds to the electronic ground state that is initially assumed.

With this notation, the state vector in the Schrödinger picture takes the following form:

$$|\Psi\rangle = \sum_{(\gamma)}^{v,c} \sum_{n=0}^{\infty} \tilde{c}_n^{(\gamma)} \, |(\gamma), n\rangle = \sum_{(\gamma)}^{v,c} \sum_{n=0}^{\infty} c_n^{(\gamma)} e^{\frac{1}{i\hbar} E_n^{(\gamma)} t} \, |(\gamma), n\rangle \,, \tag{4.7}$$

where the sum over (γ) is meant in such a way that the summation is performed for all possible compound indices. $E_n^{(\gamma)}$ is the energy of the state $|(\gamma), n\rangle$ that does not need to be specified, but can be obtained from Eq. (4.1). Substituting Eq. (4.1) and Eq. (4.7) into the Schrödinger equation Eq. (2.53) leads equations of motion for the probability amplitudes $c_n^{(\gamma)}$:

$$\begin{aligned} -i\hbar\partial_t c_n^{(\gamma)} = &\sum_{j=1}^{N} M c_{n-1}^{(\gamma|\gamma_j+1)} e^{-\frac{i}{\hbar}\Delta_{k_j} t} \sqrt{n} \delta_{\gamma_j, v} \\ &+ \sum_{j=1}^{N} M c_{n+1}^{(\gamma|\gamma_j-1)} e^{\frac{i}{\hbar}\Delta_{k_j} t} \sqrt{n+1} \delta_{\gamma_j, c}. \end{aligned} \tag{4.8}$$

The first summand on the right-hand side describes all possible relaxations of an electron under the respective emission of a photon, whereas the second summand describes all possible promotions of an electron under the respective absorption of a photon. The optical

detuning $\Delta_{\boldsymbol{k}}$ reads:

$$\Delta_{\boldsymbol{k}} = \hbar(\omega_{\boldsymbol{k}} - \nu), \tag{4.9}$$

$$\hbar\omega_{\boldsymbol{k}} = \epsilon^{c}_{\boldsymbol{k}} - \epsilon^{v}_{\boldsymbol{k}}, \tag{4.10}$$

where we call the $\boldsymbol{k}$-dependent transition frequency $\omega_{\boldsymbol{k}}$ the band structure, that determines that material properties of the considered semiconductor nanostructure. We model the electronic band structure by use the tight-binding approximation, where the electrons of the isolated atoms that form the solid are assumed to be strongly localized at the atomic sites, so that the electron wave functions of two neighbouring sites have a small overlap, while this overlap is negligible when considering two sites that are not neighbours, e.g. next-nearest neighbours [23]. Tight-binding models typically lead to band energies $\epsilon^{\gamma}_{\boldsymbol{k}}$ that have a cosine-dependence with respect to the momentum $\boldsymbol{k}$, so that a 1D tight-binding model leads to the following band structure:

$$\omega_k = \omega_g + \frac{\omega_b}{2}\Big[1 - \cos(ka)\Big], \tag{4.11}$$

where ω_g is the band gap, ω_b is the band width, and a is the lattice constant. ω_g and ω_b are determined by the lattice periodical atomic potential and atomic wave-functions. We, however, use parameters that allow for a reasonable description of the direct semiconductor GaAs: $\omega_g = 1.5$ eV, $\omega_b = 1.8$ eV, and $a = 5.65$Å. We restrict our consideration to the first Brillouin zone, which means that $|k| \leq \frac{\pi}{a}$. The dispersion Eq. (4.10) for the 1D tight-binding model Eq. (4.11) is shown with respect to the band-gap energy $\hbar\omega_g$ in Fig. 4.2. Similarly,

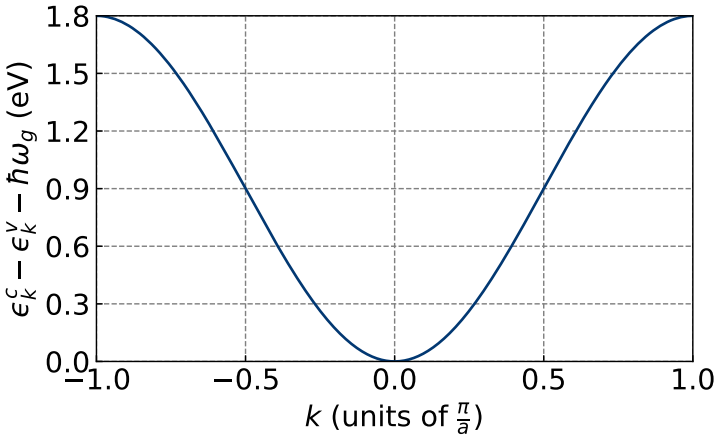

Figure 4.2: Dispersion $\hbar\omega_{\boldsymbol{k}}$ from Eq. (4.10) for the 1D tight-binding model Eq. (4.11). Taken from [109].

the 2D tight-binding model leads to the following band structure:

$$\omega_{\boldsymbol{k}} = \omega_g + \frac{\omega_b}{4}\Big[2 - \cos(k_x a) - \cos\big(k_y a\big)\Big]. \tag{4.12}$$

Fig. 4.3 shows the dispersion Eq. (4.10) for the 2D tight-binding model Eq. (4.12) with respect to the band-gap energy $\hbar\omega_g$. We note that this dispersion does not take into account the face centered cubic lattice of GaAs in k-space, but rather models a cubic lattice.

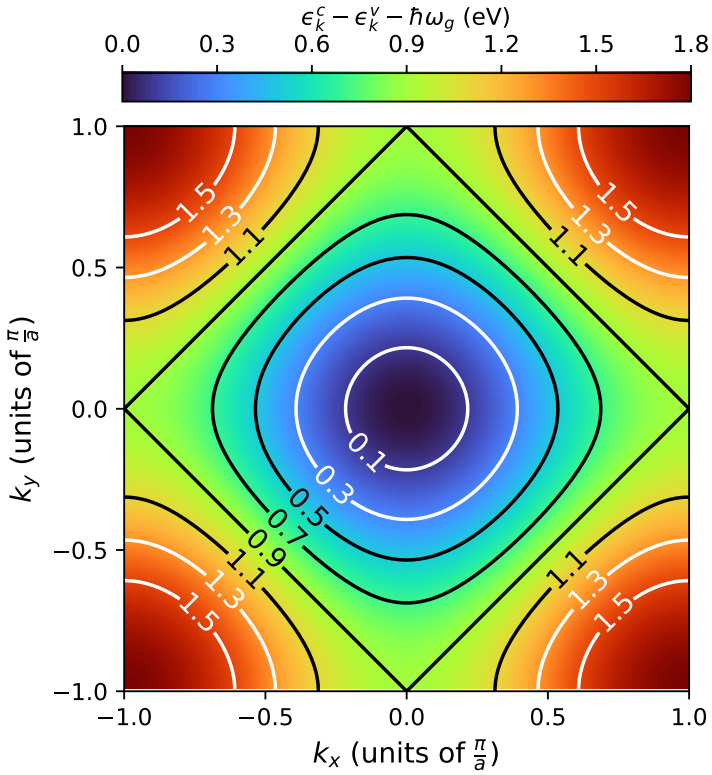

Figure 4.3: Dispersion $\hbar\omega_{\boldsymbol{k}}$ from Eq. (4.10) for the 2D tight-binding model Eq. (4.12). The contour lines run along a constant energy that is given in units of eV. Taken from [109].

The observables that we focus on are the (electronic) ground-state probability (GSP) O_{ground}, i.e., the probability of all k-points being in the ground state and the conduction-band probability $O_c^{k_j}$ of a single k-point k_j. These observables can be written in terms of probability amplitudes $c_n^{(\gamma)}$:

$$O_{\text{ground}} = \sum_{n=0}^{\infty} |c_n^{(v)}|^2, \tag{4.13}$$

$$O_c^{k_j} = \sum_{n=0}^{\infty} \sum_{\gamma \neq \gamma_j} |c_n^{(\gamma|\gamma_j=c)}|^2. \tag{4.14}$$

In the following, we comment on the numerical complexity of the problem. We note that a quantum state of light that is truncated at a maximum Fock state number of $n_{\max}$ can excite $n_{\max}$ k-points simultaneously at maximum. We define Γ as the number of possible

compound indices (γ), i.e., the number of possible matter excitation states, for a given $n_{\max}$. Since N is assumed to be large, we can always assume $n_{\max} < N$, which allows to write Γ as:

$$\Gamma = \sum_{j=0}^{n_{\max}} \binom{N}{j} = \sum_{j=0}^{n_{\max}} \frac{N!}{j!(N-j)!} = \underbrace{1}_{n_{\max}=0} + N + \underbrace{\frac{1}{2}(N-1)N}_{n_{\max}=1} + \underbrace{\frac{1}{6}(N-2)(N-1)N + \ldots}_{n_{\max}=2}, \quad (4.15)$$

where we find the dependence $\Gamma \sim N^{n_{\max}}$, which means that the number of matter excitation states increases exponentially with $n_{\max}$, making the treatment of bright quantum states of light numerically demanding and in some cases even impossible [112, 113]. Therefore, we will mainly focus on the excitation with single photon Fock state, which reduces the basis B_{sp} to $N+1$ states:

$$B_{\text{sp}} = \{ |(v), 1\rangle, |(v|\gamma_1 = c), 0\rangle, |(v|\gamma_2 = c), 0\rangle, ..., |(v|\gamma_N = c), 0\rangle \}, \quad (4.16)$$

and allows to write the equations of motion from Eq. (4.8) in the following form:

$$\partial_t c_1^{(v)} = \frac{i}{\hbar} \sum_{l=1}^{N} M c_0^{(v|\gamma_l = c)} e^{-\frac{i}{\hbar}\Delta_{k_l} t}, \quad (4.17)$$

$$\partial_t c_0^{(v|\gamma_j = c)} = \frac{i}{\hbar} M c_1^{(v)} e^{\frac{i}{\hbar}\Delta_{k_j} t}. \quad (4.18)$$

Note that the probability amplitudes in the Schrödinger picture read $\tilde{c}_n^{(\gamma)} = c_n^{(\gamma)} e^{\frac{1}{i\hbar} E_n^{(\gamma)} t}$, whereas $c_n^{(\gamma)}$ corresponds to the probability amplitude in the interaction picture. While the interaction picture is advantageous for numerical treatments, the Schrödinger picture can be more advantageous for analytical treatments. The equations of motion for $\tilde{c}_n^{(\gamma)}$ can be written as:

$$i\hbar \partial_t \tilde{c}_1^{(v)} = \sum_{l=1}^{N} -M \tilde{c}_0^{(v|\gamma_l = c)}, \quad (4.19)$$

$$i\hbar \partial_t \tilde{c}_0^{(v|\gamma_j = c)} = -M \tilde{c}_1^{(v)} + \Delta_{\boldsymbol{k}_j} \tilde{c}_0^{(v|\gamma_j = c)}, \quad (4.20)$$

where the energies were shifted with respect to the resonance. The matrix that describes the system of differential equations is the Hamiltonian, as can be identified with the

Schrödinger equation Eq. (2.53):

$$i\hbar\partial_t \begin{bmatrix} \tilde{c}_1^{(v)} \\ \tilde{c}^{(v|\gamma_1=c)} \\ \tilde{c}^{(v|\gamma_2=c)} \\ \vdots \\ \tilde{c}^{(v|\gamma_N=c)} \end{bmatrix} = \underbrace{\begin{bmatrix} 0 & -M & -M & \cdots & -M \\ -M & \Delta_1 & 0 & \cdots & 0 \\ -M & 0 & \Delta_2 & \ddots & 0 \\ \vdots & \vdots & \ddots & \ddots & \vdots \\ -M & 0 & 0 & \cdots & \Delta_N \end{bmatrix}}_{=H} \begin{bmatrix} \tilde{c}_1^{(v)} \\ \tilde{c}^{(v|\gamma_1=c)} \\ \tilde{c}^{(v|\gamma_2=c)} \\ \vdots \\ \tilde{c}^{(v|\gamma_N=c)} \end{bmatrix}, \tag{4.21}$$

where $\Delta_j = \Delta_{k_j}$ was introduced for a more convenient notation.

The observables Eqs. (4.13) and (4.14) simplify in the single-photon case as follows:

$$O_{\text{ground}} = |c_1^{(v)}|^2, \tag{4.22}$$

$$O_c^{k_j} = |c_0^{(v|\gamma_j=c)}|^2. \tag{4.23}$$

The same simplification can be done for the case of a two-photon Fock state, which leads to a basis set B_{tp} containing $\frac{1}{2}N(N-1)+N+1$ states:

$$\begin{aligned} B_{\text{tp}} = \{ &|(v),2\rangle, |(v|\gamma_1=c),1\rangle, |(v|\gamma_2=c),1\rangle, ..., |(v|\gamma_N=c),1\rangle, \\ &|(v|\gamma_1=\gamma_2=c),0\rangle, |(v|\gamma_1=\gamma_3=c),0\rangle, ..., |(v|\gamma_{N-1}=\gamma_N=c),0\rangle\}. \end{aligned} \tag{4.24}$$

Applying this basis set to Eq. (4.8) leads to the equations of motion for the two-photon Fock-state:

$$\partial_t c_2^{(v)} = \frac{i}{\hbar}\sum_{l=1}^{N} M c_1^{(v|\gamma_l=c)} e^{-\frac{i}{\hbar}\Delta_{k_l} t}\sqrt{2}, \tag{4.25}$$

$$\partial_t c_1^{(v|\gamma_j=c)} = \frac{i}{\hbar} M c_0^{(v)} e^{\frac{i}{\hbar}\Delta_{k_j} t}\sqrt{2} + \frac{i}{\hbar}\sum_{l=1,l\neq j}^{N} M c_0^{(v|\gamma_j=\gamma_l=c)} e^{-\frac{i}{\hbar}\Delta_{k_l} t}, \tag{4.26}$$

$$\partial_t c_0^{(v|\gamma_j=\gamma_l=c)} = \frac{i}{\hbar} M c_1^{(v|\gamma_l=c)} e^{\frac{i}{\hbar}\Delta_{k_j} t} + \frac{i}{\hbar} M c_1^{(v|\gamma_j=c)} e^{\frac{i}{\hbar}\Delta_{k_l} t}. \tag{4.27}$$

and to a simpler expression for the observables Eqs. (4.13) and (4.14):

$$O_{\text{ground}} = |c_2^{(v)}|^2, \tag{4.28}$$

$$O_c^{k_j} = |c_1^{(v|\gamma_j=c)}|^2 + \sum_{l=1,l\neq j}^{N} |c_0^{(v|\gamma_j=\gamma_l=c)}|^2. \tag{4.29}$$

4.2 Analytical Treatment

Since the system has a large number of dynamical quantities, it is evident that an analytical treatment of the system is challenging. Therefore, the analytical treatment is restricted to the single photon case.

We start with a general consideration of the system and will then subdivide the treatment into a 1D and 2D case. The analytical treatment is based on the solution of the eigenvalue of the Hamiltonian:

$$H\left|\psi\right\rangle = \lambda\left|\psi\right\rangle, \tag{4.30}$$

$$\Rightarrow \det(H - \lambda\mathbb{1}) = 0. \tag{4.31}$$

where $\mathbb{1}$ is the identity matrix. The Hamiltonian can be referred from Eq. (4.21), so that the matrix $H - \lambda\mathbb{1}$ takes the following form:

$$H - \lambda\mathbb{1} \equiv A_N = \begin{bmatrix} -\lambda & -M & -M & \cdots & -M \\ -M & \Delta_1 - \lambda & 0 & \cdots & 0 \\ -M & 0 & \Delta_2 - \lambda & \ddots & 0 \\ \vdots & \vdots & \ddots & \ddots & \vdots \\ -M & 0 & 0 & \cdots & \Delta_N - \lambda \end{bmatrix} \in \mathbb{R}^{N+1\times N+1}. \tag{4.32}$$

The determinant of A_N is given by:

$$\det(A_N) = -\lambda\prod_{k=1}^{N}(\Delta_k - \lambda) - M^2\sum_{i=1}^{N}\prod_{\substack{j=1\\ j\neq i}}^{N}(\Delta_j - \lambda). \tag{4.33}$$

We proof Eq. (4.33) with induction. We see that Eq. (4.33) is true for N=2:

$$\begin{aligned}\det(A_2) &= -\lambda(\Delta_1 - \lambda)(\Delta_2 - \lambda) - M^2[(\Delta_1 - \lambda) + (\Delta_2 - \lambda)] \\ &= -\lambda\sum_{k=1}^{2}(\Delta_k - \lambda) - M^2\sum_{i=1}^{2}\prod_{\substack{j=1\\ j\neq i}}^{2}(\Delta_j - \lambda)\end{aligned} \tag{4.34}$$

The induction step is computed with help of the Laplace expansion, where the expansion is done with respect to the last column of the matrix and the determinant of the first

submatrix is solved with an expansion with respect to the last row:

$$\begin{aligned}
\det(A_{N+1}) =& (-1)^{N+3}(-M)(-1)^{N+2}(-M)\prod_{i=1}^{N}(\Delta_i-\lambda) + (-1)^{2N+2}(\Delta_{N+1}-\lambda)\det(A_N)\\
=& (\Delta_{N+1}-\lambda)\det(A_N) - M^2\prod_{i=1}^{N}(\Delta_i-\lambda)\\
\overset{\text{Eq. (4.33)}}{=}& (\Delta_{N+1}-\lambda)\left(-\lambda\prod_{k=1}^{N}(\Delta_k-\lambda) - M^2\sum_{i=1}^{N}\prod_{\substack{j=1\\ j\neq i}}^{N}(\Delta_j-\lambda)\right) - M^2\prod_{\substack{i=1\\ i\neq N+1}}^{N+1}(\Delta_i-\lambda)\\
=& -\lambda\prod_{k=1}^{N+1}(\Delta_k-\lambda) - M^2\sum_{i=1}^{N}\prod_{\substack{j=1\\ j\neq i}}^{N+1}(\Delta_j-\lambda) - M^2\prod_{\substack{i=1\\ i\neq N+1}}^{N+1}(\Delta_i-\lambda)\\
=& -\lambda\prod_{k=1}^{N+1}(\Delta_k-\lambda) - M^2\sum_{i=1}^{N+1}\prod_{\substack{j=1\\ j\neq i}}^{N+1}(\Delta_j-\lambda). \qquad \square
\end{aligned}$$

Substituting Eq. (4.33) into Eq. (4.31) leads to:

$$-\lambda = M^2\sum_{i=1}^{N}\frac{1}{\Delta_i-\lambda} \equiv G(\lambda), \tag{4.35}$$

where the right-hand side is defined as $G(\lambda)$ to allow for more convenient notations.

In the following, we will analyze the eigenvalue spectrum, where we proof that the eigenvalue spectrum is composed of a single negative eigenvalue λ_0 and N positive eigenvalues λ_i, $i = 1, 2, ..., N$. According to Eq. (4.35), λ is a solution when the functions $f(\lambda) = -\lambda$ and $G(\lambda)$ intersect. While the domain of f is unrestricted, i.e., $f : \mathbb{R} \to \mathbb{R}$, whereas G shows singularities at $\lambda = \Delta_i$. Since $\Delta_i \geq 0$, we can restrict our consideration to the interval $D_0^G = (\infty, 0[$, such that $G : D_0^G \to B_0^G$, where B_0^G is the resulting range of G. We continue with a consideration of the monotonous behavior. f is a strictly monotonous decreasing function, while G is a strictly monotonous increasing function, as can be seen from the first derivatives:

$$f'(\lambda) = -1 < 0, \tag{4.36}$$

$$G'(\lambda) = M^2\sum_{i=1}^{N}\frac{1}{(\Delta_i-\lambda)^2} > 0. \tag{4.37}$$

When considering D_0^G as domain, we find $f : D_0^G \to]0, \infty)$ and since $G(\lambda) > 0$ for $\lambda < 0$, it follows that $B_0^G \subseteq]0, \infty)$. This together with the monotonous behavior results in the existence of exactly one negative eigenvalue λ_0. Since a $(N + 1) \times (N + 1)$ matrix has $N + 1$ eigenvalues when counted according to their algebraic multiplicity, the remaining N

eigenvalues must be positive. □

The existence of the positive eigenvalues can be qualitatively understood by limiting the domain to intervals between the adjacent singularities $]\Delta_i, \Delta_j[$, where each of these lead to a positive solution. Thus, for $N \longrightarrow \infty$, the continuous eigenvalue spectrum is expected to behave like the band structure. Physically, the negative eigenvalue is an analog to the electronic ground state, where all k-point transitions are not excited, whereas the positive eigenvalues are an analog to the N possible excitations, which means that this continuum of positive eigenvalues can be interepreted as the collective excitation to a broadband second level. Note that this is only an analog, since the eigenstates $|\psi_m\rangle$ are a superposition of the product states $|\gamma, n\rangle$ and vice versa the product states $|\gamma, n\rangle$ are a superposition of eigenstates $|\psi_m\rangle$.

We continue with the normalized eigenvectors that are obtained by solving the following linear system of equations

$$A_N |\psi\rangle = 0, \tag{4.38}$$

which leads to the following solution

$$|\psi_m\rangle = \frac{1}{\sqrt{1 + G'(\lambda_m)}} \left[|(v), 1\rangle + \sum_{j=1}^{N} \frac{M}{\Delta_j - \lambda_m} \left| (v|\gamma_j = c), 0 \right\rangle \right]. \tag{4.39}$$

The state vector from Eq. (4.7) for the single-photon base from Eq. (4.16) can now be expressed in terms of eigenvectors:

$$|\Psi(t)\rangle = \sum_{m=0}^{N} z_m e^{-\frac{i}{\hbar}\lambda_m t} |\psi_m\rangle, \tag{4.40}$$

with $z_m = \langle\psi_m|\Psi(t=0)\rangle$. Since we assume the semicondcutor to initially be in the ground state, i.e., $|\Psi(t=0)\rangle = |(v), 1\rangle$, c_m can be calculated as:

$$z_m = \langle\psi_m|\Psi(t=0)\rangle = \langle\psi_m|(v), 1\rangle = \frac{1}{\sqrt{1 + G'(\lambda_m)}}. \tag{4.41}$$

Eq. (4.40) can now be used to find an expression for the probability amplitudes $\tilde{c}_n^{\gamma}$, where we are interested in the GSP that is determined by $\tilde{c}_1^{v}$:

$$\tilde{c}_1^{(v)} = \langle (v), 1|\Psi\rangle = \sum_{m=0}^{N} \langle\psi_m|(v), 1\rangle \, e^{-\frac{i}{\hbar}\lambda_m t} \, \langle (v), 1|\psi_m\rangle \tag{4.42}$$

$$= \sum_{m=0}^{N} |\, \langle\psi_m|(v), 1\rangle \,|^2 e^{-\frac{i}{\hbar}\lambda_m t} = \sum_{m=0}^{N} w_m e^{-\frac{i}{\hbar}\lambda_m t}, \tag{4.43}$$

where the abbreviation w_m was introduced, which expresses the weight of an eigenvalue:

$$w_m = \left[1 + G'(\lambda_m)\right]^{-1} \tag{4.44}$$

Eq. (4.43) expresses $c_1^{(v)}$ in terms of the eigenvalues, which we, however, do not know yet explicitly. What we do know, however, is that the eigenvalue spectrum is composed of a single negative eigenvalue while all others are positive, so that Eq. (4.43) can be written as:

$$\tilde{c}_1^{(v)} = \underbrace{w_0 e^{\frac{i}{\hbar}|\lambda_0|t}}_{\text{single state}} + \underbrace{\sum_{m=1}^{N} w_m e^{-\frac{i}{\hbar}|\lambda_m|t}}_{\text{continuum}}, \tag{4.45}$$

We continue with a proof that the continuum vanishes for $t \to \infty$. For $N \to \infty$ we obtain a continuous spectrum of eigenvalues $\lambda(z)$ and a continuous function for the weights $w(z)$, where $\lambda(z)$ behaves like the band structure and therefore is an integrable function. Since, however, the weight of a single value in a continuous space must be zero, it needs to be considered in a small region $\mathrm{d}z$, so that the sum can be approximated as an integral:

$$\sum_{m=1}^{N} w_m e^{-\frac{i}{\hbar}|\lambda_m|t} \xrightarrow{N\to\infty} \sim \int_{z_{\min}}^{z_{\max}} w(z) e^{-\frac{i}{\hbar}|\lambda(z)|t} \mathrm{d}z = \int_{\lambda(z_{\min})}^{\lambda(z_{\max})} \underbrace{\frac{w(\lambda^{-1}(u))}{\lambda'(\lambda^{-1}(u))}}_{\equiv \Lambda(u)} e^{-\frac{i}{\hbar}|u|t} \mathrm{d}u = \mathcal{F}(\Lambda)(t), \tag{4.46}$$

where $\lambda^{-1}(z)$ is the inverse of $\lambda(z)$ and $\mathcal{F}(f)$ denotes the Fourier transform of f.

Since we consider only finite contributions of $\Lambda(u)$ within the interval $[\lambda(z_{\min}), \lambda(z_{\max})]$, $\Lambda(u)$ is an integrable function, which means that the Riemann Lebsegue lemma [114] applies for the Fourier transform: $\mathcal{F}(\Lambda)(t) \xrightarrow{t\to\infty} 0$. □

This leads to the following conclusion:

$$\lim_{t\to\infty} |\tilde{c}_1^{(v)}|^2 = \lim_{t\to\infty} |c_1^{(v)}|^2 = |w_0|^2. \tag{4.47}$$

The steady-state value of the GSP only depends on the weight of the negative eigenvalue w_0, which only depends on the negative eigenvalue λ_0 for a given band structure. For the previous arguments, it was not required to specify the dimension of the system. In the following subsections, we will derive analytical solutions for λ_0 that allow to study steady-state values of the GSP.

4.2.1 One-Dimensional Band Structure

We start with the calculation of $G(\lambda)$ from Eq. (4.35) for the 1D tight-binding model Eq. (4.11), where we convert the sum to an integral for $N \to \infty$, which symbolically reads:

$$\lim_{N\to\infty} M^2 \sum_{j=1}^{N} \to \lim_{N\to\infty} M^2 \frac{N-1}{\frac{2\pi}{a}} \int_{1.\,\mathrm{BZ}} \mathrm{d}k = M_0^2 \frac{a}{2\pi} \int_{1.\,\mathrm{BZ}} \mathrm{d}k \tag{4.48}$$

Using Eq. (4.48), we can rewrite Eq. (4.35) with Eq. (4.11) as follows:

$$\begin{aligned} G(\lambda) &= M^2 \sum_{j=1}^{N} \frac{1}{\Delta_j - \lambda} = M_0^2 \frac{a}{2\pi} \int_{-\pi/a}^{\pi/a} \frac{1}{\frac{\omega_b}{2}[1-\cos(ka)] - \lambda} \mathrm{d}k \\ &= -M_0^2 \frac{1}{\lambda\sqrt{1-\frac{\omega_b}{\lambda}}}, \quad \lambda < 0. \end{aligned} \tag{4.49}$$

The integral has only solutions for negative eigenvalues, which is what we are interested in. Note that aside from the approximations that are included in the model itself, no approximations were done to obtain Eq. (4.49). Assuming that $\omega_b \gg \lambda_0$ (which is valid for small M_0), we find a compact expression for the negative eigenvalue:

$$\lambda_0 \approx -\left(\frac{M_0^4}{\omega_b}\right)^{1/3} \quad \text{for} \quad 1 - \frac{\omega_b}{\lambda_0} \approx -\frac{\omega_b}{\lambda_0}. \tag{4.50}$$

The derivative of $G(\lambda)$ can be calculated to:

$$G'(\lambda) = -M_0^2 \frac{\omega_b - 2\lambda}{2\lambda^2(\lambda-\omega_b)\sqrt{1-\frac{\omega_b}{\lambda}}}. \tag{4.51}$$

Eq. (4.51) can be used to efficiently compute Eq. (4.44). This calculation demonstrates the existence of the single negative eigenvalue for the 1D tight-binding model Eq. (4.11), which was already proofed to exist the general case. In addition, Eq. (4.50) provides an explicit expression, which together with Eq. (4.51) reveals that the steady-state probability can only depend on M_0 and ω_b, where the latter is a material constant, while the former depends on the material, the light, and especially on the optical microcavity.

To get a better idea of the full eigenvalue spectrum, we proceed with showing a numerical simulation of the diagonalization, see Fig. 4.4. Fig. 4.4(a) and Fig. 4.4(b) show the weight w_m in dependence on the respective eigenvalue λ_m. This reflects the behavior that we concluded from Eq. (4.35), i.e., the eigenvalue spectrum is composed of a single negative eigenvalue and a continuum of positive eigenvalues. Fig. 4.4(c) shows the eigenvalue λ_m in dependence on the discretization index m, which demonstrates that the positive eigenvalues follow the form of the band structure, as already concluded from Eq. (4.35).

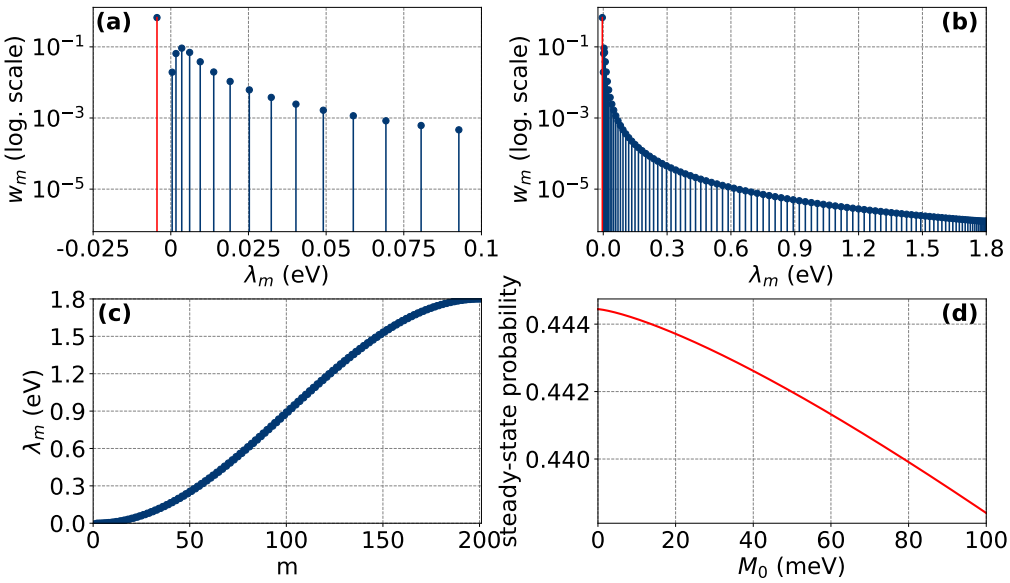

Figure 4.4: Numerical solution of the eigenvalue problem. (a) and (b) show the weights w_m at their corresponding eigenvalue λ_m (c) shows the eigenvalues λ_m in dependence on the discretization index m, where $M_0 = 20$ meV and $N = 200$. (d) shows the steady-state probability $|w_0|^2$ in dependence on M_0. Taken from [109].

Next, we take advantage of Eq. (4.47) to calculate steady-state values for different M_0 by evaluating $|w_0|^2$, see Fig. 4.4(d). For $M_0 < 1$ meV, the analytical solution from Eq. (4.50) can be used, while it is computed numerically from Eq. (4.49) otherwise. We conclude that the steady-state value $|w_0|^2$ is $\approx 4/9$ and does not significantly depend on M_0. This is a special feature found for 1D band structures, as e.g. also demonstrated for a parabolic dispersion in the vicinity of the Γ-point, where also a value of $4/9$ was found [108]. Note that the depicted values for M_0 can be realized with suitable cavities, since the coupling strength is inversely proportional to $\sqrt{V}$. A variety of optical cavities that would allow for this parameter range are presented in Ref. [115]

4.2.2 Two-Dimensional Band Structure

We proceed with the 2D tight-binding model Eq. (4.12) and follow the same order as in the previous subsection. We start with evaluating $G(\lambda)$, where we used a similar conversion from the sum to the integral as in Eq. (4.48):

$$G(\lambda) = M_0^2 \frac{a^2}{(2\pi)^2} \int_{-\pi/a}^{\pi/a} \int_{-\pi/a}^{\pi/a} \frac{\mathrm{d}k_x \mathrm{d}k_y}{\frac{\omega_b}{4}\left[2 - \cos(k_x a) - \cos\left(k_y a\right)\right] - \lambda} \tag{4.52}$$

$$= \frac{M_0^2}{\pi} \sqrt{\frac{4}{\lambda(\lambda - \omega_b)}} K\left(- \frac{\omega_b^2}{4\lambda(\lambda - \omega_b)} \right), \quad \lambda < 0, \tag{4.53}$$

where the complete elliptic integral of the first kind $K(x)$ [116], given by

$$K(x) = \int_0^{\pi/2} \frac{1}{\sqrt{1 - x\sin^2(\theta)}} \mathrm{d}\theta = \int_0^1 \frac{1}{\sqrt{(1-t^2)(1-xt^2)}} \mathrm{d}t, \tag{4.54}$$

was identified to simplify the appearing expression. For $\omega_b \gg \lambda_0$, the negative eigenvalue can approximately be obtained as:

$$\lambda_0 \approx -\frac{2M_0^2}{\pi\omega_b} W\left(\frac{2\pi\omega_b^2}{M_0^2}\right) \quad \text{for} \quad 1 - \frac{\omega_b}{\lambda_0} \approx -\frac{\omega_b}{\lambda_0}. \tag{4.55}$$

where $W(z)$ is the Lambert W function [117] that is given by the inverse function of $z(W)$ with

$$z(W) = We^W. \tag{4.56}$$

The derivative of $G(\lambda)$ can be explicitly computed to

$$G'(\lambda) = \frac{1}{\pi(\omega_b - 2\lambda)} 4M_0^2 \sqrt{\frac{1}{\lambda(\lambda - \omega_b)}} \mathrm{E}\left(-\frac{\omega_b^2}{4\lambda(\lambda - \omega_b)}\right), \tag{4.57}$$

where $E(x)$ is the complete elliptic integral of the second kind [116], given by

$$E(x) = \int_0^{\pi/2} \sqrt{1 - x\sin^2(\theta)} \mathrm{d}\theta = \int_0^1 \frac{\sqrt{1-xt^2}}{\sqrt{1-t^2}} \mathrm{d}t. \tag{4.58}$$

We note that the analytical treatment of the 2D tight-binding model Eq. (4.12) is more involved when compared with the 1D tight-binding model Eq. (4.11), but, however, still possible when introducing special mathematical functions. As in the previous case, the existence of a single negative eigenvalue and its analytical expression is demonstrated for the 2D tight-binding structure and the steady-state value can only depend on M_0 and ω_b. A numerical simulation of the eigenvalue spectrum would qualitatively lead to the same result as before, i.e., a single negative eigenvalue and a continuum of positive eigenvalues, which is why we decide to not show it again. Instead, we show the steady-state probability $|w_0|^2$ in dependence on M_0, where λ_0 for values of $M_0 < 1$ meV was computed with Eq. (4.55), while Eq. (4.53) was numerically solved otherwise and Eq. (4.57) is used for the calculation of w_m, see Fig. 4.5. In contrast to the previous case, the $|w_0|^2$ does significantly depend on M_0. It is also evident that $|w_0|^2$ is larger for the 2D case as compared to the 1D case. This can physically be understood from the increased number of non-resonant transitions introduced to the system when considering a 2D grid, instead of a 1D grid. This results in non-resonant transitions (which show a less effective transport) to be effectively weighted stronger, which reduces the significance of resonant transitions and overall leads to a higher probability of finding the electronic system in its ground state.

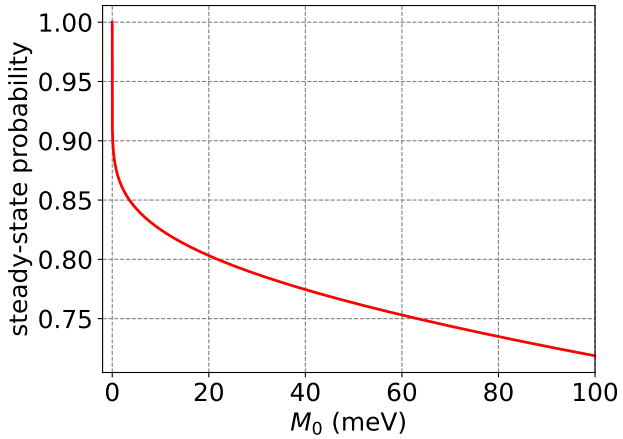

Figure 4.5: The steady-state probability $|w_0|^2$ in dependence on M_0 is shown for the 2D tight-binding model Eq. (4.12). Taken from [109].

4.3 Numerical Simulations

Subsequently to the analytical investigation, we proceed with numerical simulations of the equations of motion. This serves to demonstrate the time dynamics of the GSP, as well as of the conduction-band occupation. Furthermore, the numerical treatment allows us to easily investigate situations in which the band gap is not resonantly excited, but an energetic offset $\delta = \hbar(\nu - \omega_g)$ is introduced. If not stated otherwise, the considered quantum light is a single-photon Fock-state.

4.3.1 One-Dimensional Band Structure

We start with the consideration of the 1D tight-binding model Eq. (4.11), where we use a fixed model parameter of $M_0 = 20$ meV for all simulations.

Fig. 4.6 shows a simulation of the conduction-band occupation $O_c^{k_j}$ and the GSP, where $\delta = 0$ meV. One can see that the GSP is initially 1, which corresponds to an unexcited semiconductor, and continues with an oscillation whose amplitude gradually decreases and strives towards a constant steady-state value of approximately $\frac{4}{9}$. This is in agreement with the results of the analytical treatment in the previous section. The conduction-band occupation for the individual k_j results in an oscillation with a frequency of approximately the detuning $\Delta_j/\hbar$. Apart from the discussion of the eigenvalue spectrum, this yields another understanding of the constant value that forms during the dynamics. Due to the conservation of the trace of the density matrix, we can find the following relation between

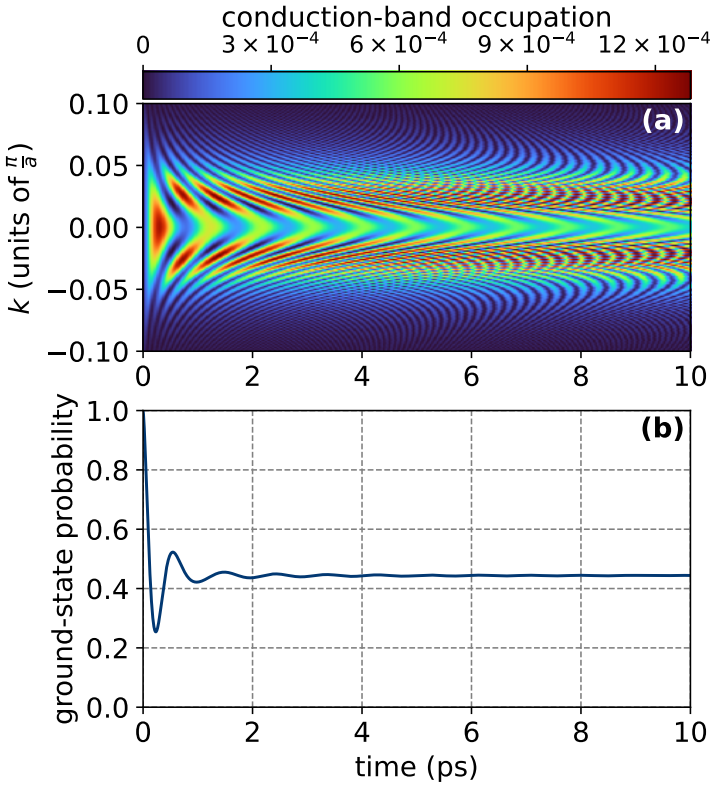

Figure 4.6: Numerical solution of (a) the conduction-band occupation $O_c^{k_j}$ (b) the GSP for the 1D tight-binding model Eq. (4.11) with $N = 20001$ and $\delta = 0$ meV. Taken from [109].

the GSP and the conduction-band occupation

$$O_{\text{ground}} = 1 - \sum_{j=1}^{N} O_c^{k_j}. \tag{4.59}$$

The oscillations at different frequencies give rise to a destructive interference that prevents further oscillations of the GSP and eventually leads to the formation of a constant value.

We continue with the consideration of $\delta \neq 0$ meV. Here, $\delta > 0$ meV means that the frequency of the light ν is larger than the band gap ω_g, leading to an excitation in the band. In contrast, $\delta < 0$ meV corresponds to an excitation below the band gap, such that no electronic transition is addressed resonantly. Fig. 4.7 shows the conduction-band occupation for different δ. One can observe that $\delta < 0$ meV leads to a smaller magnitude, since all transitions are addresses non-resonantly. In the case of $\delta > 0$ meV, however, we can see the formation of stripes, which are approximately located at $\Delta_{k_j} = 0$. In this case, certain eigenstates that are energetically located inside the band structure are excited resonantly.

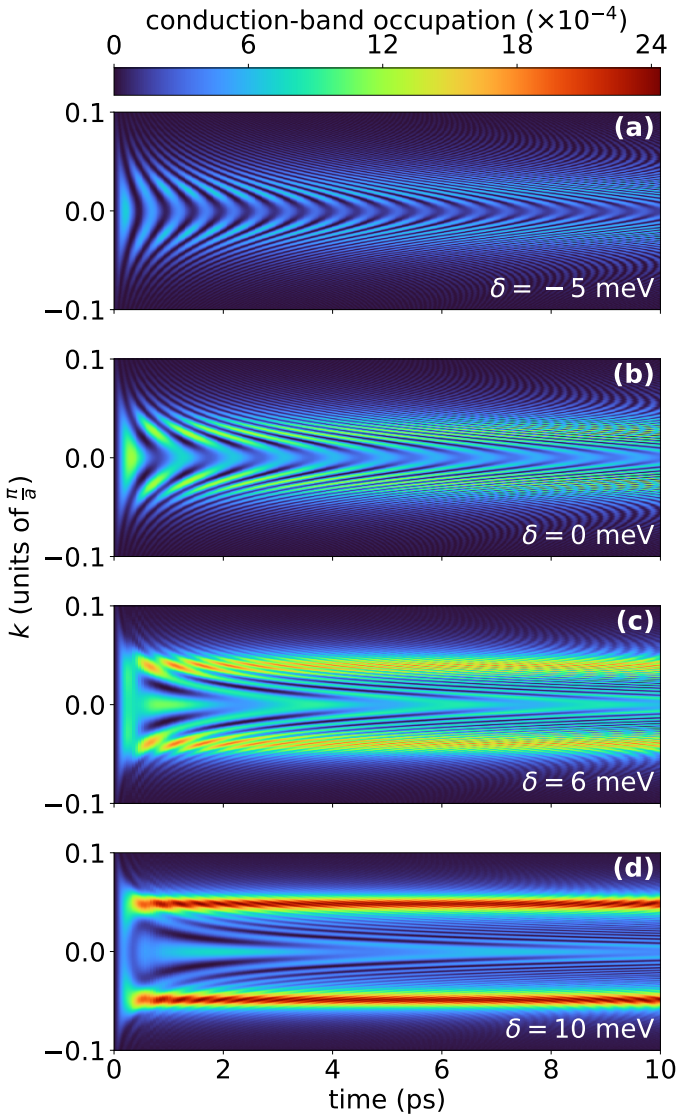

Figure 4.7: Numerical solutions of the conduction-band occupation $O_c^{k_j}$ with (a) $\delta = -5$ meV (b) $\delta = 0$ meV (c) $\delta = 6$ meV (d) $\delta = 10$ meV and $N = 20001$ for the 1D tight-binding model Eq. (4.11). Taken from [109].

The presented dynamics has a direct consequence for the GSP, according to Eq. (4.59). Fig. 4.8 shows the GSP for different δ, including the ones shown Fig. 4.7. $\delta < 0$ meV leads to a high GSP, since the probability of exciting conduction-band occupation is small. In contrast, $\delta > 0$ meV leads to a small GSP due to the resonantly excited quasienergy states inside the conduction band.

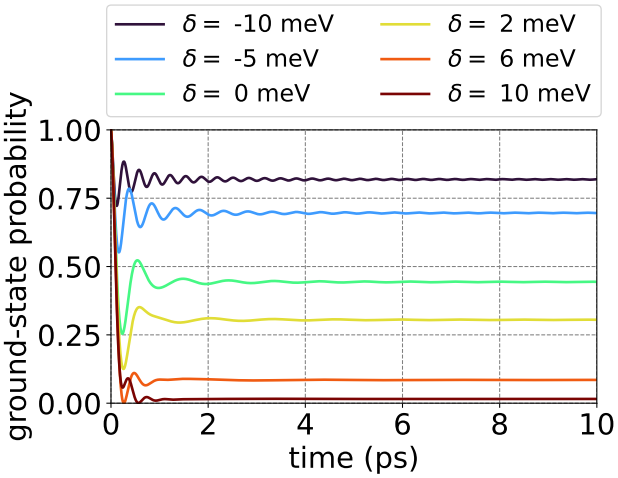

Figure 4.8: Numerical simulations of the GSP for different energetic offsets δ for the 1D tight-binding model Eq. (4.11), where $N = 20001$. Taken from [109].

After investigating the dynamics for different energetic offsets, we also want to investigate the dynamics when exciting with more photons. For this, we consider the GSP when exciting with a two-photon Fock-state, and compare it to the excitation with a single-photon Fock-state, see Fig. 4.9. The notable difference is that the GSP for a two-photon Fock-state is smaller. This is accounted to the possibility of exciting two k-point transitions at the same time, leading to more combinations of exciting the electrons into the conduction band and thus, leading to a smaller GSP. This result allows us to estimate that the GSP will further decrease for higher photon numbers, since the number of possible excitations also increases. In the limit of infinite photons, corresponding to a semiclassical theory, one would expect the GSP to be zero, which makes a finite GSP a feature exclusive to a quantum-optical description.

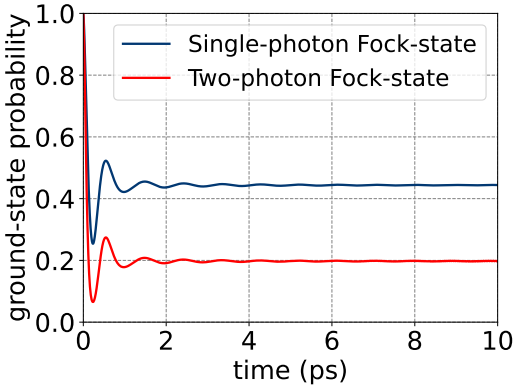

Figure 4.9: Numerical simulations of the GSP where the initial quantum state of light is a single-photon Fock-state with $N = 20001$ and a two-photon Fock-state with $N = 5001$, respectively, for the 1D tight-binding model Eq. (4.11). Taken from [109].

4.3.2 Two-Dimensional Band Structure

We proceed with the consideration of the 2D tight-binding model Eq. (4.12). In contrast to the 1D case, the steady-state probability for the 2D case was demonstrated to show a significant dependence on M_0. Therefore, we start with simulating the GSP for different M_0, see Fig. 4.10. The predicted steady-state values depicted in Fig. 4.5 are reproduced by the

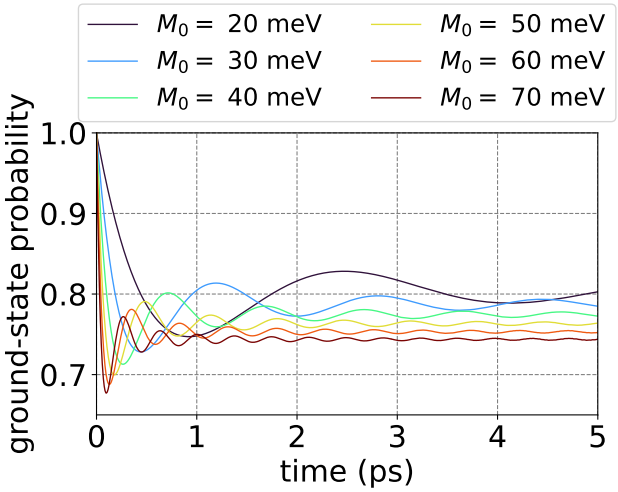

Figure 4.10: Numerical simulations of the GSP for different M_0 for the 2D tight-binding model Eq. (4.12) with $N = 2000$ per dimension and $\delta = 0$ meV. Taken from [109].

numerical simulation, even though not clearly visible, since not all dynamics have reached the constant value in the depicted time range. Qualitatively, the dynamics for different M_0 are similar, but scaled on the time-axis. Thus, considering the dynamics for a fixed M_0 is representative for other choices of M_0, where a larger M_0 is preferred, since the required simulation time window is smaller. Therefore, we proceed with a fixed model parameter of $M_0 = 50$ meV for all following simulations in this section. Fig. 4.11 shows the GSP for different energetic offsets δ. Qualitatively, the result is similar to the 1D case and there is not more insight to gain in this case. More interestingly, however, is the conduction-band occupation, which is expected to behave differently due to the increased dimension of the system. For a fixed point in time t, the conduction-band occupation is a 2D quantity, depending on k_x and k_y. For the demonstration of the conduction-band occupation, we present it in dependence on k_x and k_y at $t = 1$ ps, and in dependence on k_y and t for $k_x = 0$, as well as for energetic offsets of $\delta = 0$ meV and $\delta = 50$ meV, see Fig. 4.12. The cut at $k_x = 0$ are comparable to the 1D case, whereas, however, the cut at $t = 1$ ps allows for a different geometrical interpretation. In the case of $\delta = 0$ meV, the oscillations at different frequencies results in circles of increased probability, whose magnitude gradually decreases at higher energies, see Fig. 4.12(b). From Fig. 4.12(a) one can see that these the radius of these circle decreases over time. The stripes that can be seen in Fig. 4.12(c) correspond to a circle in the 2D k-space, see Fig. 4.12(d). Apart from the geometrical interpretation, the underlying physics is similar as discussed in the previous section.

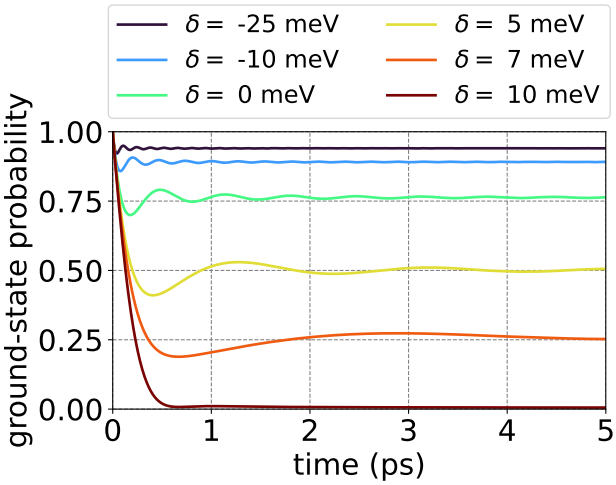

Figure 4.11: Numerical simulations of the GSP for different energetic offsets δ for the 2D tight-binding model Eq. (4.12), where $N = 2000$. Taken from [109].

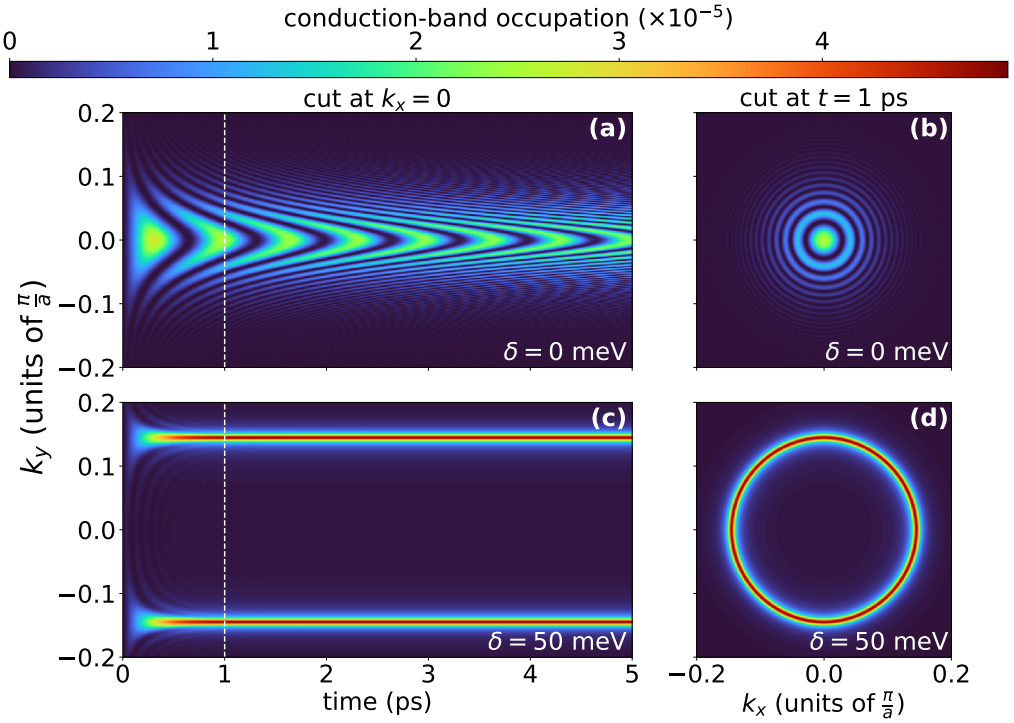

Figure 4.12: Numerical simulations of the conduction-band occupation for the 2D tight-binding model Eq. (4.12) with $N = 2501$ per dimension. Since the conduction-band occupation depends on three variables t, k_x, and k_y, the conduction-band occupation is shown for a cut, where one of these variables is fixed. The concudction-band occupation is shown for (a) $k_x = 0$ and $\delta = 0$ meV, (b) $t = 1$ ps and $\delta = 0$ meV, (c) $k_x = 0$ and $\delta = 50$ meV, and (d) $t = 1$ ps and $\delta = 50$ meV. Taken from [109].

4.4 Conclusions

In this chapter, we investigated the quantum-optical excitation of semiconductor nanostructures, by modeling their electronic band structure by a two-band model and the tight-binding approximation. We formulate the model and derive the equations of motion, where we noted that the numerical complexity significantly increases when quantum states of light with multiple photons are considered, which is why we restrict our analysis to a single-photon Fock-state and a two-photon Fock-state. We proceed with an analytical treatment of the single-photon case, where we proof properties that are valid for arbitrary band structures. We use these properties to find explicit expressions for the steady-state value of the GSP, i.e., the probability of finding the system in its electronic ground state during the interaction, which we do for both, the 1D and the 2D tight-binding model. We proceed with a numerical treatment of the system, where we investigate the time-dynamics of the system. The numerical simulations are in an agreement with the results from the analytical investigations and provide alternative physical interpretations of the demonstrated behavior. The investigation of the dynamics with different energetic offsets $\delta = \hbar(\nu - \omega_g)$ results in the formation of a steady state in the conduction-band occupation for $\delta > 0$ meV, which can be understood from eigenstates that are energetically located inside the band structure. The 2D case qualitatively leads to similar results as the 1D case, where, however, key difference are: the dependence on the light-matter coupling M_0, the increased GSP due to stronger contributions from non-resonantly excited transitions, and the different geometry of the conduction-band occupation due to 2D grid. We furthermore conclude that the excitation with quantum states of light containing more than a single photon results in a smaller GSP due to the increased number of possibilities to promote electrons to the conduction band.

Semiclassical Wave Mixing 5

Up to this point, we investigated quantum properties of semiconductor nanostructures that are pre-excited by a single quantum field. Now, we want to move on towards the description of scenarios in which the semiconductor system is excited with multiple pulses. We are especially interested in the nonlinear optical response obtained by wave-mixing experiments, where multiple pulses impinge on a sample and the nonlinear response in a designated direction is considered. Before we present the theoretical description of wave-mixing experiments for a fully quantized light-matter interaction, however, this chapter starts with presenting wave-mixing results obtained from a semiclassical theory. Here, ensembles of semiconductor quantum dots (QDs) are considered, that are useful emitters [118, 119] whose trion transition is well described by a TLS. We start with an explanation of wave-mixing experiments, followed by the formulation of a semiclassical theory for the photoexcited TLS, where we will follow a standard procedure that can be found in textbooks [120]. We proceed with the demonstration and discussion of results obtained from wave mixing, which are based on Refs. [121–123], where experimental data was analyzed. In this thesis, however, the focus is set on the theoretical descriptions, rather than on the experimental realization.

5.1 Wave-Mixing Experiments

Wave-mixing experiments is a collective term to classify experiments in which several electric fields impinge on a sample and the nonlinear optical response by the material is measured.

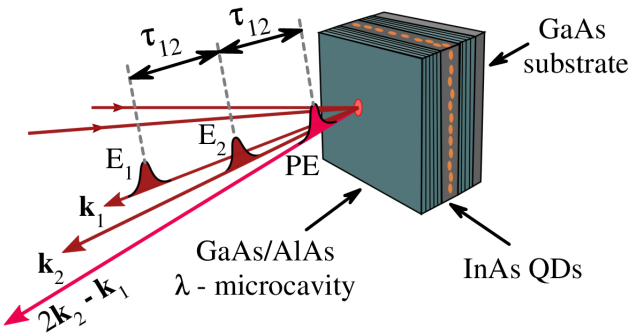

Figure 5.1: Schematical drawing of a FWM setup with two pulses in reflection geometry, performed on a QD sample confined in a microcavity. Taken from [121].

An important example is four-wave mixing (FWM) [28], where two electric fields with wave vectors $\boldsymbol{k}_1$ and $\boldsymbol{k}_2$, delayed by the time τ, impinge on the sample and the nonlinear response in the $2\boldsymbol{k}_2 - \boldsymbol{k}_1$ direction is measured. In experimental realizations, there are different geometries that can be used to retrieve this signal. Fig. 5.1 schematically depicts a FWM setup in reflection geometry. The name FWM originates from the number of waves involved in this process: since the second field counts twice when considering the direction $2\boldsymbol{k}_2 - \boldsymbol{k}_1$, the number of incoming fields together with the nonlinear response adds up to four waves.

5.2 Optical Bloch Equations

In a semiclassical theory, one does not consider a quantization of the electromagnetic field, but rather treats the electric field classically. In this case, the electric field is solely described by its amplitude and phase, so that the electric field for n pulses in free space is given by:

$$\boldsymbol{E}(t) = \sum_{l=1}^{n} (\boldsymbol{E}_l(t) \exp[i\boldsymbol{k}_l \cdot \boldsymbol{r} - i\omega_L t] + c.c.), \tag{5.1}$$

where ω_L is the frequency of the electric field and the wave-vector $\boldsymbol{k}_l$ determines the propagation direction. Since the electric field is treated classically, there is no Hamiltonian for the light. The material system, however, is treated fully quantum mechanically. Thus, the Hamiltonian from Eq. (2.45) reduces to

$$H = H_{\text{Matter}} + H_{\text{Interaction}}. \tag{5.2}$$

In this chapter, we are only interested in ensembles of TLS. In this case of a single TLS, the Hamiltonian simplifies to:

$$H_{\text{Matter}} = E_1\sigma_{11} + E_2\sigma_{22}, \tag{5.3}$$

$$H_{\text{Interaction}} = -e_0\boldsymbol{r} \cdot \boldsymbol{E} \overset{\text{Eq. (2.49)}}{=} -\boldsymbol{E} \cdot \underbrace{(\boldsymbol{d}_{12}\sigma_{12} + \boldsymbol{d}_{21}\sigma_{21})}_{\equiv \boldsymbol{P}} = -\boldsymbol{E} \cdot \boldsymbol{P}, \tag{5.4}$$

where the polarization operator $\boldsymbol{P}$ was identified. In the following, we assume the dipole matrix element $\boldsymbol{d}_{ij}$ and the electric field $\boldsymbol{E}$ to be parallel, so that the vector can be replaced by its absolute value. Since only the material is treated quantum mechanically, the DM for a TLS is given by a 2×2 matrix. If represented in the bare-state (BS) basis $\{|1\rangle, |2\rangle\}$, the DM reads:

$$\rho^{\text{BS}} = \sum_{i=1}^{2}\sum_{j=1}^{2} \rho_{ij}^{\text{BS}} |i\rangle \langle j| \tag{5.5}$$

where we can make the following identification:

$$p \equiv \langle \sigma_{21} \rangle = \mathrm{Tr}(\rho^{\mathrm{BS}} \sigma_{21}) = \rho_{12}^{\mathrm{BS}}, \tag{5.6}$$

$$n \equiv \langle \sigma_{22} \rangle = \mathrm{Tr}(\rho^{\mathrm{BS}} \sigma_{22}) = \rho_{22}^{\mathrm{BS}}, \tag{5.7}$$

where p is the microscopic polarization and n is the occupation of the excited state. Note that using p and n or ρ_{12}^{BS} and ρ_{22}^{BS} is equivalent, where, however, the notation ρ_{ij}^{BS} is more advantageous since we will switch to a different basis later. The resulting equations of motion for p and n are the optical Bloch equations (OBE) and have the following form after the RWA is applied[124]:

$$\partial_t \rho_{12}^{\mathrm{BS}} = i\Delta \rho_{12}^{\mathrm{BS}} + i\Omega_R (1 - 2\rho_{22}^{\mathrm{BS}}), \tag{5.8}$$

$$\partial_t \rho_{22}^{\mathrm{BS}} = -2\mathrm{Im}\left[(\rho_{12}^{\mathrm{BS}})^* \Omega_R \right], \tag{5.9}$$

where $\Delta = \omega_L - (\tilde{E}_2 - \tilde{E}_1)/\hbar$ is the optical detuning and Ω_R is the Rabi frequency that depends on the dipole matrix element and the envelope of the electric field $\mathcal{E}$ as follows:

$$\Omega_R = \frac{d_{12}}{\hbar} \mathcal{E}. \tag{5.10}$$

An instructive way to visualize the dynamics of a TLS geometrically is given by the Bloch sphere, where one considers the vector

$$\boldsymbol{b} = \begin{bmatrix} 2\mathrm{Re}(p) \\ 2\mathrm{Im}(p) \\ 2n - 1 \end{bmatrix}. \tag{5.11}$$

Without any dephasing or losses, the Bloch vector $\boldsymbol{b}$ has a length of 1 and therefore spans a sphere of radius 1, which is the Bloch sphere. Conventionally, the x, y, and z components are called u, v, and w, which we will use from now on. In the RWA, the free evolution of p results in a rotation in the u-v-plane where the angular velocity is proportional to Δ. The excitation with an electric field leads to a rotation around the u-axis, where the angle of rotation traveled is called pulse area and is given by:

$$\Theta = \int_{-\infty}^{\infty} \Omega_R(t) \mathrm{d}t, \tag{5.12}$$

where we call a short electric field with a pulse area of Θ a Θ-pulse. The Bloch sphere will be used in the subsequent sections to explain the occurring dynamics.

5.3 Control of Photon Echoes

In QD ensembles, one does not usually find N identical QDs, but rather, one finds some variation in their properties such as their size. This gives rise to different transition energies

of the trions, distributed according to a distribution function $L(\omega)$ that informs about the number of trions with transition frequency ω. Such ensembles are called inhomogeneously broadened ensembles and give rise to optical properties that are distinctively different the ones found for homogeneous ensembles.

5.3.1 Photon Echoes

One feature of inhomogeneously broadened ensembles is the rapid decay of the macroscopic polarization, due to a dephasing of the microscopic polarizations p. The dephasing of the ensemble can be visualized on the Bloch sphere by assigning a single Bloch vector to each TLS, which freely evolve with their respective detuning Δ, visualized for a $\pi/2$-pulse as first pulse in Fig. 5.2(a).

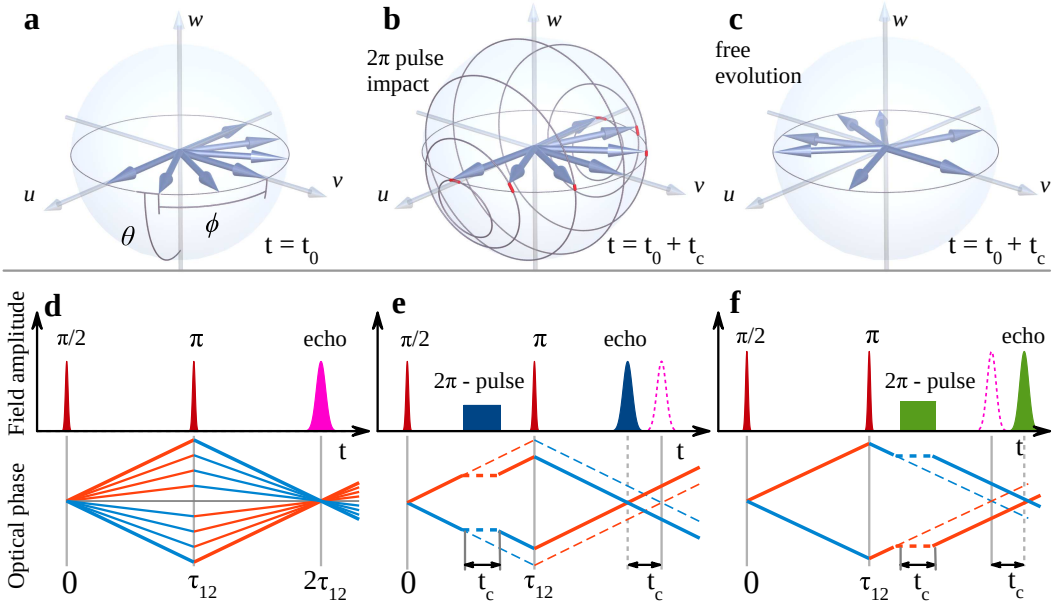

Figure 5.2: (a-c) Bloch spheres after the excitation with a $\pi/2$-pulse that display the Bloch vectors at (a) $t = t_0$ during the dephasing after the excitation with a pulse with a pulse area of π, (b) $t = t_0 + t_c$ after the application of a control pulse during the dephasing with duration t_c, where the trajectory of the Bloch vectors that is caused by the control pulse is marked in gray and the small difference towards a perfect 2π rotation that is not achieved due to the finite pulse duration is marked in red, (c) $t = t_0 + t_c$ without the application of a control pulse. (d-f) Schematical depiction the field amplitudes over time together with the time evolution of the optical phases of the microscopic polarizations p (angle of the Bloch vectors with respect to the v-axis) of a two-pulse FWM setup, where (a) no control pulse is applied (b) a control pulse during the dephasing is applied (c) a control pulse during the rephasing is applied. Taken from [121].

Overlapping Bloch vectors interfere constructively, while separated Bloch vectors interference destructively, leading to a decay of macroscopic polarization. This macroscopic

polarization, however, can be retrieved by FWM experiments in the form of a photon echo (PE) [125, 126]. A second pulse with a pulse area of π at $t = \tau$ conjugates the microscopic polarizations and leads to the formation of a PE at $t_{\mathrm{PE}} = 2\tau$. The evolution of the phases is schematically demonstrated in Fig. 5.2(d). On the Bloch sphere, the conjugation corresponds to a rotation of π around the u-axis without changing the angular velocity of the Bloch vectors. PEs are of special interest due their applicability for quantum memories [127–130].

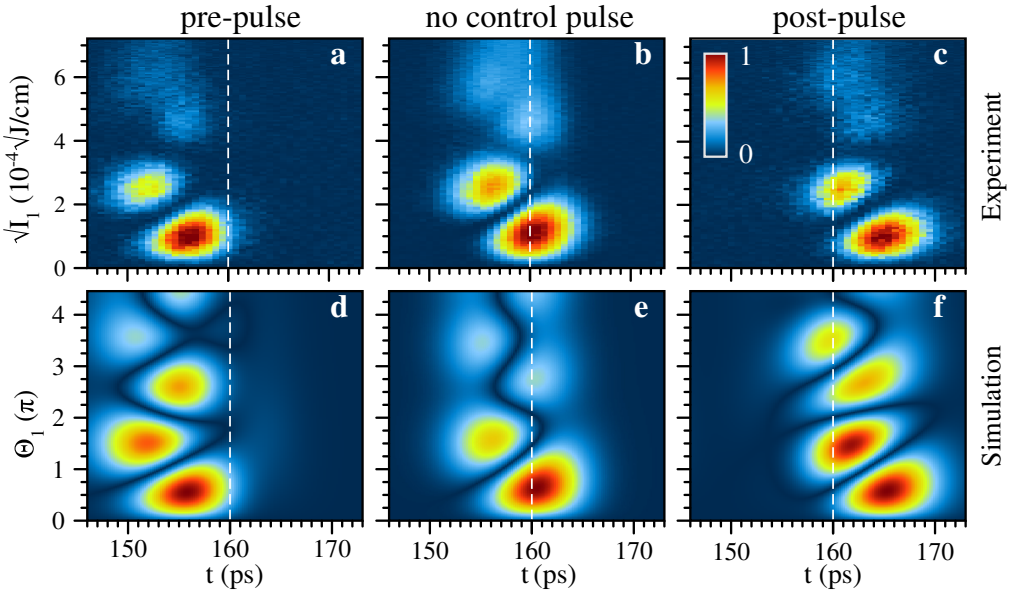

Figure 5.3: (a-c) Experimental data for the FWM setups discussed in the text. Each point on the y-axis corresponds to a different measurement, in which the amplitude of the electric field was set to the denoted value. (a) shows the pre-pulse setup, (b) shows the no control pulse setup, and (c) shows the post-pulse setup. (d-f) Numerical simulations of $|P_{\mathrm{Signal}}|$ from Eq. (5.20), where each point on the y-axis corresponds to a different pulse area of the first pulse, corresponding to the amplitudes considered in (a-c). (d) shows the pre-pulse setup, (e) shows the no control pulse setup, and (f) shows the post-pulse setup. Taken from [121].

5.3.2 Control Scheme

In the following, we present a scheme that allows to optically control the emission time of the PE, so that $t_{\mathrm{PE}} \neq 2\tau$. This scheme is based on adding an additional control pulse to the pulse sequence, that either freezes the dephasing or the rephasing. Fig. 5.2(a) shows the dephasing of the microscopic polarizations on the Bloch sphere at $t = t_0$. Applying a 2π control pulse leads to a 2π rotation of all Bloch vectors, such that they have not changed their position at $t = t_0 + t_c$, see Fig. 5.2(b). Without the application of this control pulse, the dephasing would continue and the Bloch vectors would be positioned as shown in Fig. 5.2(c). Thus, the application of a control pulses during the dephasing (pre-pulse)

leads to a temporal advancement of the PE. The field amplitudes and the optical phases of such a setup with and without the control pulse are schemed in Fig. 5.2(e). With the same approach, one can achieve a temporal retardation of the PE, by applying a control pulse during the rephasing (post-pulse), see Fig. 5.2(f). This effect was observed and verified by our experimental colleagues, see Figs. 5.3(a)-(c), where all details can be found in Ref. [121]. In this thesis, however, we focus on the theoretical description that analyzes the experiment and at this especially on the inclusion of damping mechanisms.

5.3.3 Theoretical Description

As demonstrated in Section 5.2, the optical properties of a TLS are described by the OBE Eqs. (5.8) and (5.9). The OBE, however, describe the polarization that is emitted in all directions, which is why one is formally required to filter the $2\boldsymbol{k}_2 - \boldsymbol{k}_1$-direction to correctly describe the signal. In the case of PEs, however, this is not required, since the PE is expected to be the dominant signal during the time span around $t = 2\tau$. For the theoretical decription, we need to apply two relevant extensions to the OBE, which are the inhomogeneous broadening given by $L(\omega)$ and the fact that laser light has a spatial distribution, which means that different points on the spot are excited with a different Rabi frequency. The former can be included by an additional index j, while the latter is incorpoarated by assigning a spatial dependence to p and n, i.e., $p = p(\boldsymbol{r}, t)$ and $n = n(\boldsymbol{r}, t)$. In this case, the we obtain the following set of extended OBE:

$$\partial_t p_j(\boldsymbol{r}, t) = i\Delta p_j(\boldsymbol{r}, t) + i\Omega_R(1 - 2n_j(\boldsymbol{r}, t)) - p_j(\boldsymbol{r}, t)/T_2, \tag{5.13}$$

$$\partial_t n_j(\boldsymbol{r}, t) = -2\mathrm{Im}\left[(p_j(\boldsymbol{r}, t))^* \Omega_R\right] - n_j(\boldsymbol{r}, t)/T_1, \tag{5.14}$$

where the coherence time and lifetime T_2 and T_1, respectively, was introduced. The spatial dependence of the microscopic polarizations is incorporated by considering the spatial dependence of the electric field, that is to say, the polarization $p(\boldsymbol{r} = \boldsymbol{r}', t)$ is obtained by using the electric field amplitude $\mathcal{E}(\boldsymbol{r} = \boldsymbol{r}', t)$ as input, where the electric field amplitude is modeled as follows:

$$\mathcal{E}(\boldsymbol{r}, t) = \exp\left(-r^2/\sigma_R^2\right)(\mathcal{E}_1(t) + \mathcal{E}_2(t) + \mathcal{E}_C(t)), \tag{5.15}$$

which means that the spatial profile follows a Gaussian envelope. The temporal envelope is modeled with a Gaussian function with a full-width at half-maximum (FWHM) of Δt with respect to the intensity, i.e.,

$$\mathcal{E}_i = \mathcal{E}_i^0 \exp\left(-2\ln(2)\frac{(t - t_i)^2}{\Delta t}\right), \tag{5.16}$$

where t_i is the time at which the pulse impinges the sample and $\mathcal{E}_i^0$ is the amplitude that is determined by the pulse area according to Eq. (5.12). According to the experiment, the first and the second pulse come at $t_1 = 0$ ps and $t_2 = 80$ ps, respectively, while the control pulse impinges at $t_c = 33$ ps in the pre-pulse setup and at $t_c = 107$ ps, where $\Delta t = 2.5$ ps.

The macroscopic polarization at the point $\boldsymbol{r}$ is due to the inhomogeneous broadening F given by:

$$P(\boldsymbol{r},t) = d_{12}\sum_j F(\Delta_j)p_j(\boldsymbol{r},t), \tag{5.17}$$

where F is modeled as a Gaussian function with a FWHM of 7.5 meV. The polarizations $P(\boldsymbol{r},t)$ that are created at different points $\boldsymbol{r}$ on the spot are assumed to emit an electric field that impinges on a detector at the same coordinate $\boldsymbol{r}$, such that the total signal that the detector would measure corresponds to an averaging of $P(\boldsymbol{r},t)$ over all $\boldsymbol{r}$. This process is called spatial averaging and can be expressed by the following integral

$$P_{\text{average}}(t) = \int \mathrm{d}\boldsymbol{r}\,\exp\left(-r^2/\sigma_R^2\right)P(\boldsymbol{r},t), \tag{5.18}$$

where the additional factor of $\exp\left(-r^2/\sigma_R^2\right)$ arises from the heterodyne detection, where a convolution with a reference pulse must be considered, which is assumed to have the same properties as the other pulses. Instead of solving the integral in 2D, we take advantage of the radial symmetry and switch to the polar coordinate system. Subsequent, we exchange the integral to a sum by introducing the discretization index s, which then yields an expression for P_{average} that can be efficiently computed numerically:

$$P_{\text{average}}(t) = 2\pi\sum_s r_s\Delta r\,\exp\left(r_s^2/\sigma_R^2\right)P(r_s,t). \tag{5.19}$$

Strictly following the order of the events, the spatial averaging must not be performed on $P(r_s,t)$, but on $P(r_s,t)$ which was convoluted with $\mathcal{E}_{\text{Ref}}$ in the time domain. Since, however, the convolution is a linear operation, the result remains the same if the convolution is applied afterwards. Thus, the final signal is obtained by computing the convolution between P_{average} and $\mathcal{E}_{\text{Ref}}$:

$$P_{\text{Signal}} = (P_{\text{average}} * \mathcal{E}_{\text{Ref}})(t), \tag{5.20}$$

where the convolution is defined as

$$(f*g)(t) \equiv \int_{-\infty}^{\infty} f(y)g(x-y)\mathrm{d}y. \tag{5.21}$$

Figs. 5.3(d-f) show $|P_{\text{Signal}}|$ for the pre-pulse setup, the no control pulse setup, and the post-pulse setup. For the simulation, $N = 1500$ TLS were considered, where detunings from −15 meV up to 15 meV with a resulting resolution of 0.02 meV were considered. The coherence time and the life time are set to $T_2 = 710$ ps and $T_1 = 360$ ps, respectively. The extended OBE Eqs. (5.13) and (5.14) were solved with the Runge-Kutta fourth-order method with a temporal time-step of 0.01 ps. For the spatial averaging, radii from $r = 0.05\sigma_R$ up to $r = 3.5\sigma_R$ with a step width of $\Delta r = 0.05\sigma_R$ were considered. Here, it is noteworthy that the value of σ_R, which corresponds to the spot size, does not influence the results. The

pulse areas were sampled with $\Delta\Theta_1 = 0.05$.

We see that the experimental results and the numerical simulations are in a good qualitative agreement. One can see, however, that the damping with respect to the pulse area Θ_1 is weaker for the simulated data. In the theoretical description, a perfect alignment of the spatial envelopes of the pulses is considered, which might not be fulfilled in the experimental setup. Therefore, we continue with investigating a displacement of the foci of the spatial envelopes. For this, we repeat the explained steps, but consider the following electric field amplitude:

$$\mathcal{E}(\boldsymbol{r}, t) = e^{-((x-x_0)^2+y^2)/\sigma_R^2}\mathcal{E}_1(t) + e^{-(x^2+y^2)/\sigma_R^2}(\mathcal{E}_2(t) + \mathcal{E}_3(t)), \tag{5.22}$$

which describes a displacement of the spatial enevelope of the first electric field by x_0 in the x-direction. In this case, we cannot take advantage of symmetries, which is why the problem needs to be computed in 2D. Therefore, P_{average} has the following form:

$$P_{\text{average}}(t) = \sum_{s,s'} \Delta x \Delta y \exp\left(-(x_s^2 + y_{s'}^2)/\sigma_R^2\right) P((x_s, y_{s'}), t). \tag{5.23}$$

Apart from these changes, the procedure to obtain P_{Signal} remains the same. We set the displacement to $x_0 = 0.5\sigma_R$ and consider values from $x = -3.5\sigma_R$ to $x = 5\sigma_R$ for the x-direction and from $y = -3.5\sigma_R$ to $y = 3.5\sigma_R$ for the y-direction. The stepwidths are chosen as $\Delta x = \Delta y = 0.2\sigma_R$, $dt = 0.04$ ps, and $\Delta\Theta_1 = 0.3$, while all other parameters are the same as before. The simulation for the same scenarios as before, but with displaced foci is shown in Fig. 5.4.

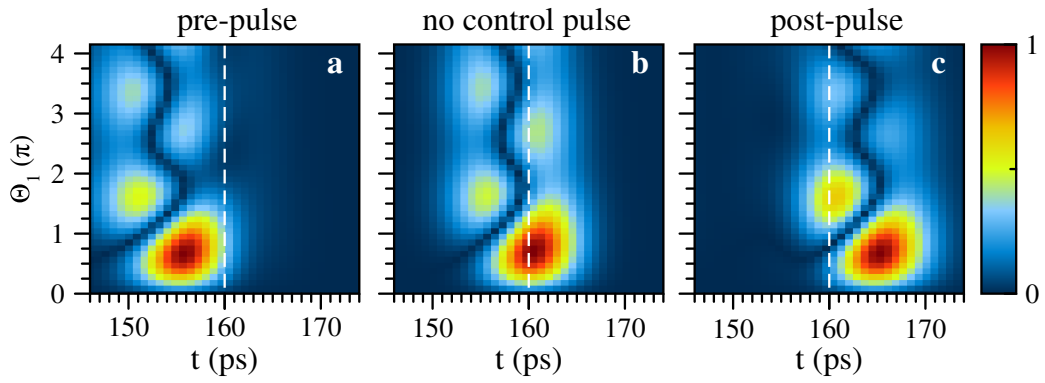

Figure 5.4: Numerical simulations of $|P_{\text{Signal}}|$, where different foci of the spots according to Eq. (5.22) with $x_0 = 0.5\sigma_R$ are assumed. The considered pulse setup is the (a) pre-pulse setup (b) no control pulse setup (c) post-pulse setup. Taken from [121].

We see that a displacement of the foci of a fraction of standard deviation already leads to a significantly stronger damping, which is in a very good agreement with the experimental data. Thus, we conclude that the spatial averaging and especially imperfect alignments of the electric field amplitudes on the spot are the main damping mechanism in these types

of experiments.

5.4 Overcoming Damping Induced by Spatial Averaging

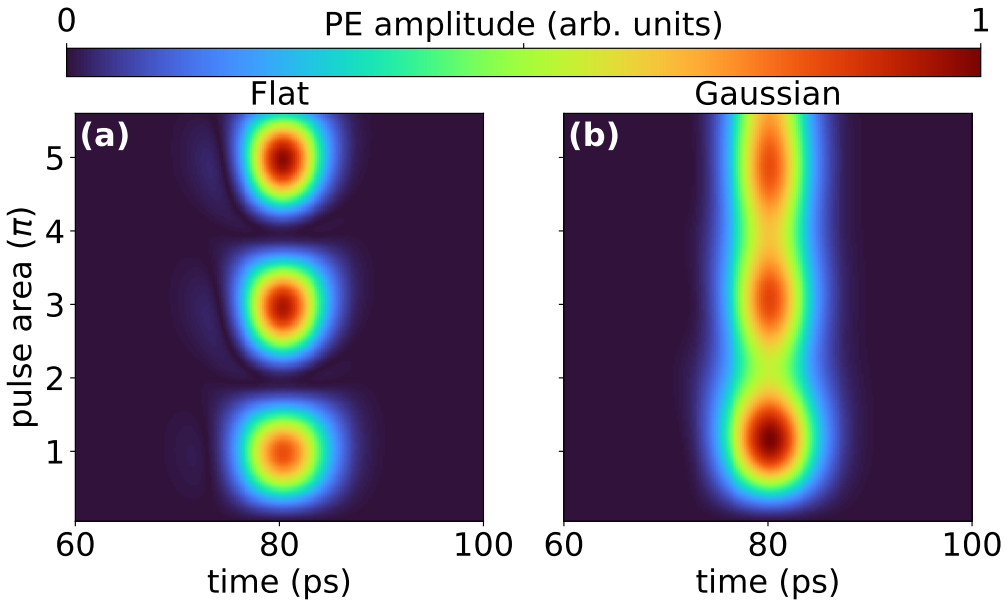

Figure 5.5: Numerical simulation of the FWM response $|P_{\text{signal}}|$, which yields the PE amplitude, with the parameters from Section 5.3.3, where the pulse area of the second pulse is scanned on the y-axis, while the first pulse is a $\pi/2$-pulse. The first pulse has a Gaussian spatial distribution and the second pulse has a (a) flat spatial distribution (b) Gaussian spatial distribution.

When moving towards the quantum regime, eliminating and overcoming damping mechanism is relevant, since these mechanisms usually destroy quantum properties. Since we identified the spatial averaging as main damping mechanism, we aim to eliminate this mechanism. Considering the integral that describes the spatial averaging Eq. (5.18), it becomes evident that any cancellation by this averaging can be bypassed if the polarization at each point $\boldsymbol{r}$ is the same, i.e. $P(\boldsymbol{r}, t) = P(t)$. This can be achieved by using spatially flat pulses, which can experimentally realized by pulse shaping, as demonstrated by a numerical simulation in Fig. 5.5. The emerging challenge, however, is to identify and incorporate the damping mechanisms that were negligible when compared with the spatial averaging, but are dominant without the spatial averaging. Comparisons with experimental data reveal that two new damping mechanisms must be considered when working with flat pulses, which are randomly distributed dipole moments among the QDs and the interaction with longitudinal acoustic (LA) phonons. Similar as before, we will explain the details on the theoretical modeling and will later compare it with experimental results. In this section, however, we do not consider a scan of the pulse area of the first pulse, but of the

second pulse instead. This has the advantage that one obtains clear Rabi oscillations along $t = 2\tau$ (see Fig. 5.5), so that one can consider this section and obtains a more transparent insight when studying damping mechanisms.

5.4.1 Theoretical Description

In the following, we will explain the required steps to include both, the LA phonons and the randomly distributed dipole moments.

Inclusion of Longitudinal Acoustic Phonons

In Section 5.2, we treated the dynamics of a photo-excited TLS in the BS basis. When treating the interaction with LA phonons, however, the dressed-state (DS) basis constitutes a more suitable choice. We will explain this method based on Ref. [131], where a constant Rabi frequency Ω_R was considered, and will subsequently, extend the scheme to time-dependent Rabi frequencies $\Omega_R(t)$. Note, however, that both these methods are approximations. More profound approaches are based on the correlation expansion [132–134], polaron master equations [135–139], or path-integral calculations [140, 141].

In the presence of an electric field with the Rabi frequency Ω_R, new eigenstates $|l\rangle$ and $|u\rangle$ are formed, which we call dressed states:

$$|l\rangle = \frac{1}{\sqrt{2\Omega}} \left(\sqrt{\Omega - \Delta}\, |1\rangle + \sqrt{\Omega + \Delta}\, |2\rangle \right), \tag{5.24}$$

$$|u\rangle = \frac{1}{\sqrt{2\Omega}} \left(\sqrt{\Omega + \Delta}\, |1\rangle - \sqrt{\Omega - \Delta}\, |2\rangle \right), \tag{5.25}$$

where $\Omega = \sqrt{\Omega_R^2 + \Delta^2}$. The DM can be formulated with respect to the DS basis:

$$\rho^{\mathrm{DS}} = \rho_{11}^{\mathrm{DS}} |l\rangle \langle l| + \rho_{21}^{\mathrm{DS}} |u\rangle \langle l| + \rho_{12}^{\mathrm{DS}} |l\rangle \langle u| + \rho_{22}^{\mathrm{DS}} |u\rangle \langle u|, \tag{5.26}$$

such that the transformation between ρ^{BS} and ρ^{DS} is given by

$$\rho^{\mathrm{DS}} = V^{-1} \rho^{\mathrm{BS}} V, \tag{5.27}$$

$$\rho^{\mathrm{BS}} = V \rho^{\mathrm{DS}} V^{-1}, \tag{5.28}$$

where the unitary matrix V is given by:

$$V = V(\Omega_R, \Delta) = \frac{1}{\sqrt{2\Omega}} \begin{bmatrix} \sqrt{\Omega - \Delta} & \sqrt{\Omega + \Delta} \\ \sqrt{\Omega + \Delta} & -\sqrt{\Omega - \Delta} \end{bmatrix}. \tag{5.29}$$

Considering the DM elements in the DS basis is advantageous, since LA phonons can be included as a rate equation:

$$\frac{\partial}{\partial t}\rho_{12}^{\mathrm{DS}} = -i\Omega\rho_{12}^{\mathrm{DS}} - \frac{\gamma}{2}\rho_{12}^{\mathrm{DS}}, \tag{5.30}$$

$$\frac{\partial}{\partial t}\rho_{22}^{\mathrm{DS}} = -\gamma\rho_{22}^{\mathrm{DS}}. \tag{5.31}$$

Here, γ is the phononic loss rate that is modeled according to Ref. [131]:

$$\gamma = \frac{\pi}{2}\left(\frac{\Omega_R}{\Omega}\right)^2 J(\Omega), \tag{5.32}$$

where $J(\omega)$ is the phonon spectral density, which for a spherical symmetric QD is given by:

$$J(\omega) = A\omega^3 \exp\left(-\frac{\omega^2}{\omega_c^2}\right), \tag{5.33}$$

where A is a constant the corresponds to the coupling strength of the phonons and ω_c is the cut-off frequency, where both these values are determined by material parameters of the QDs. This approach of incorporating the interaction with phonons is simple when compared to microscopic simulations, the transformation to the DS basis, however, is only defined for a fixed Rabi frequency Ω_R, which corresponds to a continuous-wave excitation, as investigated in Ref. [131].

We, however, are interested in the description of short pulses whose Rabi frequency $\Omega_R(t)$ changes rapidly as a function of time, which is why we are required to extend the presented approach to allow for arbitrary Rabi frequencies. This can be realized by approximating the time-dependent Rabi frequency $\Omega_R(t)$ as a sequence of rectangles. For this, we define the grid t_0,t_1,...,t_M such that $\Omega_R(t)$ is enclosed within t_0 and t_M. In this grid, we consider M rectangles that are delimited by t_{k-1} and t_k, where $t = 1, 2, ..., M$, whose Rabi frequency is given by the mean value of $\Omega_R(t_{k-1})$ and $\Omega_R(t_k)$:

$$\Omega_{R,k} = \frac{1}{2}\Big(\Omega_R(t_k) + \Omega_R(t_{k-1})\Big). \tag{5.34}$$

The approximation of $\Omega_R(t)$ by rectangles is schematically depicted in Fig. 5.6.

As a next step, we take advantages of this approximation as it allows us to compute the dynamics within a rectangle in the DS basis, since $\Omega_{R,k}$ is constant in time. At $t = t_k$, i.e., between two rectangle functions, we do the transformation

$$\rho^{DS} = V^{-1}(\Omega_{R,k+1}, \Delta)V(\Omega_{R,k}, \Delta)\rho^{DS}V^{-1}(\Omega_{R,k}, \Delta)V(\Omega_{R,k+1}, \Delta), \tag{5.35}$$

which describes the promotion from the rectangle at $\Omega_R = \Omega_{R,k}$ to the rectangle at $\Omega_R = \Omega_{R,k+1}$. If M is large enough, this excitation scheme converges and suitably describes

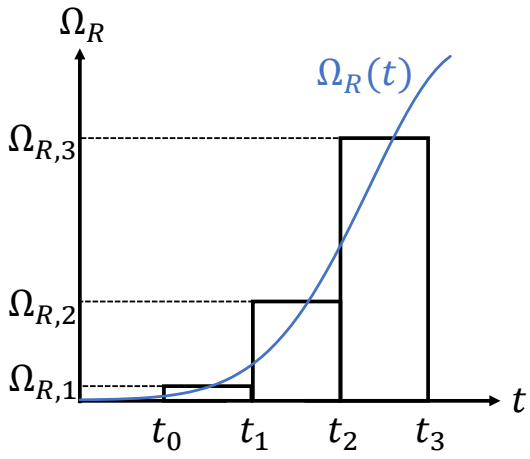

Figure 5.6: Schematical drawing of the excitation scheme in the DS basis

the interaction with LA phonons for time-dependent excitations. In absence of any electric field, the free evolution of the system is computed with the OBE:

$$\frac{\partial}{\partial t}\rho_{12}^{\mathrm{BS}} = i\Delta\rho_{12}^{\mathrm{BS}}, \tag{5.36}$$

$$\frac{\partial}{\partial t}\rho_{22}^{\mathrm{BS}} = 0. \tag{5.37}$$

Inclusion of Randomly Distributed Dipole Moments

After the inclusion of the LA phonons, we continue with including the remaining mechanisms, which include the inhomogeneous broadening, the spatial averaging, and the random distribution of the dipole moments [142]. The former two mechanisms were already introduced Section 5.3.3, which is why we will concentrate on the latter mechanism. Note that even though we have the goal to overcome the damping induced by spatial averaging, we still include it by using the experimentally measured amplitudes, to capture the imperfections in the setup. Radial slices of the experimentally measured amplitudes are shown in Fig. 5.7, where the first pulse has a Gaussian spatial profile and the second pulse has a flat spatial profile.

The incorporation of these three mechanisms is done by including subscripts j, d, and s, which correspond to the inhomogeneous broadening, the dipole averaging, and the spatial

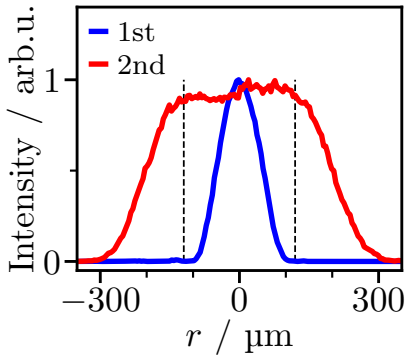

Figure 5.7: Section of the experimentally measured spatial distributions of the spots, which are used as an input for the numerical simulation. Taken from [123].

averaging, respectively:

$$\frac{\partial}{\partial t}[\rho_{12}^{\mathrm{DS}}]_{j,d,s} = -i\Omega_{j,d,s}[\rho_{12}^{\mathrm{DS}}]_{j,d,s} - \frac{\gamma}{2}[\rho_{12}^{\mathrm{DS}}]_{j,d,s}, \tag{5.38}$$

$$\frac{\partial}{\partial t}[\rho_{22}^{\mathrm{DS}}]_{j,d,s} = -\gamma[\rho_{22}^{\mathrm{DS}}]_{j,d,s}, \tag{5.39}$$

$$\frac{\partial}{\partial t}[\rho_{12}^{\mathrm{BS}}]_{j,d,s} = i\Delta_j[\rho_{12}^{\mathrm{BS}}]_{j,d,s}, \tag{5.40}$$

$$\frac{\partial}{\partial t}[\rho_{22}^{\mathrm{BS}}]_{j,d,s} = 0, \tag{5.41}$$

with $\Omega_{j,d,s} = \sqrt{[\Omega_R]_{d,s}^2 + \Delta_j^2}$, and $\left[\Omega_R\right]_{d,s} = (1-\delta\mu_d)A_s^n\Omega_R$, where $\delta\mu_d$ is the percentual deviation from the most likely dipole matrix element μ, and A_s^n is the spatial profile of the laser spot for first ($n = 1$) or second ($n = 2$) electric field, obtained from the experimental data shown in Fig. 5.7. The inhomogeneous broadening is incorporated according to Eq. (5.17), such that:

$$P_{d,s} = d_{12}\sum_j F(\Delta_j)p_{j,d,s},, \tag{5.42}$$

where in this case, however, $F(\Delta)$ is modeled as a Lorentzian distribution with a FWHM of 5.9 meV, as extracted from experimental data. The dipole matrix elements are assumed to be distributed according to a Gaussian function $\tilde{G}(\delta\mu_d)$, leading to a macroscopic polarization that is averaged over randomly distributed dipole moments:

$$P_s = \sum_d \tilde{G}(\delta\mu_d)(1-\delta\mu_d)P_{d,s}. \tag{5.43}$$

Finally, the spatial averaging is included as in Eq. (5.19), leading to:

$$P_{\mathrm{averaged}} = 2\pi\sum_s r_s\Delta r A_s^{\mathrm{ref}}P_s, \tag{5.44}$$

where we assume $A_s^{\text{ref}} = A_s^1$. Since the experimental data is used for the spatial profiles, they are not radial symmetric anymore. However, we consider a radial slice of the 2D spatial profiles and assume radial symmetry for the remaining spot, since it is a reasonable approximation and saves computation time. As before, P_{Signal} is then obtained from Eq. (5.20). Note that we did not consider any T_1 or T_2 times in the equations of motion. To also include the excitation-induced dephasing, which is characterized by a T_2 time that depends on the impinged pulse area, we multiply a factor of $\exp(-2\tau/T_2(A_2))$, where $T_2(A_2)$ is obtained from a linear fit of the experimental data. This mechanism, however, is found to be negligible.

While the spatial distribution and the inhomogeneous broadening are fixed, we consider both, the distribution of dipole moments and the phonon spectral density as fitting parameters to obtain a good agreement with the experimental data. This optimization procedure leads to $A = 0.012$ ps^2, $\omega_c = 3.6$ THz, and a FWHM of 21% for the dipole distribution $\tilde{G}(\delta\mu_d)$. Eqs. (5.38) to (5.41) are solved with the Runge-Kutta method of fourth-order, where a timestep of $dt = 0.02$ ps was used. For the excitation scheme, the electric fields are divided into $M = 501$ rectangles, that are sampled in a duration of 20 ps around the pulse. We use $N = 800$ TLS and consider detunings from −15 meV to 15 meV.

5.4.2 Simulation Results and Discussion

Fig. 5.8 shows both, results from measurements and from numerical simulations.

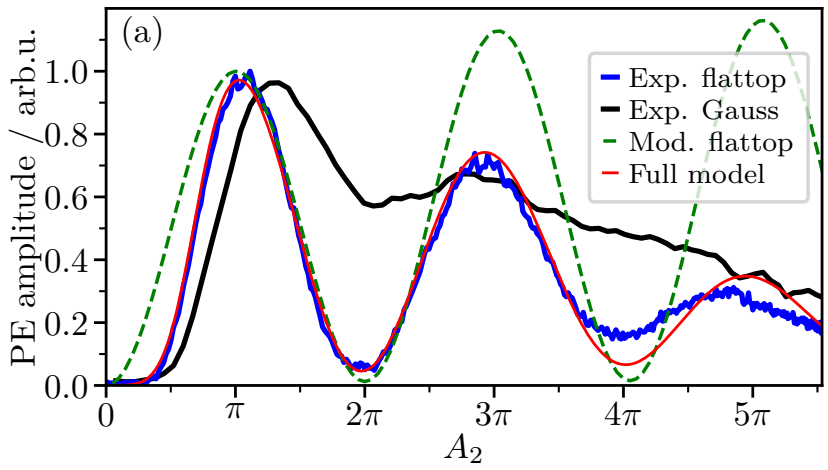

Figure 5.8: PE amplitude in dependence on the pulse area of the second pulse from a two-pulse FWM setup. Experimental data is shown for the case that the first pulse has a Gaussian spatial distribution and the second pulse a spatially flat distribution (solid blue line) or a Gaussian spatial profile (solid black line). Results of numerical simulations are shown for the case that only the spatial averaging is incorporated (dashed green line) and for the case that all damping mechanisms are included, i.e., spatial averaging, dipole averaging, and interaction with LA phonons (solid red line). Taken from [123].

All curves present the PE amplitude at $t = 2\tau$, whose dependence on the pulse area of the second pulse is shown. The solid blue and solid black lines are experimental results from our colleagues, obtained by using a Gaussian spatial profile for the first pulse, whereas the spatial profile of the second pulse is a flat distribution (solid blue) and a Gaussian distribution (solid black). Here, it is observed that the application of a flat spatial profile leads to much clearer Rabi oscillations, which verifies the initial idea. The dashed green and the solid red curves show numerical simulations, where the former does only include the spatial averaging with the experimental data shown in Fig. 5.7, which results in flawless Rabi oscillations and therefore demonstrates that the spatial profile obtained from beam shaping is sufficient. The solid red curve includes all discussed damping mechanisms, i.e., the spatial averaging with the data from Fig. 5.7, the dipole averaging, and the interaction with LA phonons. We see that experimental result and the simulated result are in a very good agreement, with a slight difference at higher pulse areas, from which we conclude that we identified all relevant damping mechanisms. We note that the damping by the dipole averaging is considerably weaker as compared to the damping by the LA phonons, which is not explicitly shown here. We conclude, the main damping mechanism that we identify in absence of the spatial averaging is the interaction with LA phonons during the excitation with a laser pulse.

5.5 Conclusions

We analyzed FWM experiments with a semiclassical theory for the light-matter interaction. We demonstrated that the emitted PE can be precisely controlled, which is promising for quantum memory protocols, where PEs play an important role. We furthermore demonstrated that the main damping mechanism, which is the spatial averaging, can be removed. We conclude that the new main damping mechanism are the interaction with LA phonons.

Altogether, the presented results demonstrate that FWM spectroscopy is a useful technique, since PEs that are candidates for quantum memory protocols can be precisely controlled and losses can be reduced. The connection between wave mixing and quantum light is a highly promising field, since the combination of both these fields can give rise to new methods and techniques. Therefore, the next chapter will give an insight into the highly promising field of quantum wave mixing.

Quantum Wave Mixing 6

This chapter discusses the combination of a fully-quantized description of light-matter interaction and wave-mixing protocols, resulting in quantum wave mixing. The goal of this chapter is to give an idea of the current state and open problems as well as presenting results obtained from approximations. The considered approximations strongly simplify the involved processes, while more complete models are currently being developed. Here, we will consider both homogeneously and inhomogeneously broadened systems, where the former does cover semiconductor quantum wells and the latter does include semiconductor quantum dot systems. The comparison between semiclassical and quantum-optical approaches for the analysis of quantum emitters is a current topic [143] and there have been approaches to simplify the dynamics from a Tavis-Cummings model with a frequency distribution by formulating mean-field equations [144]. There are, however, proposed approaches for the simulation of quantum wave mixing where the photon statistics is taken into account [145, 146], which are promising and will be subject of the present chapter.

6.1 Theoretical Model

The Hamiltonian that describes an inhomogeneously broadened ensemble of QDs is given by

$$H = \hbar\nu\left(b^\dagger b + \frac{1}{2}\right) + \sum_{j=1}^{N_{\mathrm{TLS}}} \hbar\omega_j a_j^\dagger a_j + \sum_{j=1}^{N_{\mathrm{TLS}}} g_j (b^\dagger a_j + b a_j^\dagger), \tag{6.1}$$

where ω_i are the transition frequencies of the TLS in the inhomogeneously broadened ensemble and N_{TLS} is the number of TLS. Here, a_j and $a_j^\dagger$ correspond to the transition operator σ_- and σ_+ from Section 2.4.3 for the j-th QD. Note that this Hamiltonian is similar to the Hamiltonian for the two-band model Eq. (4.1), which is why the treatment is conceptually the same. Here, however, we do not consider a single excitation that is applied initially, but rather a pulse sequence. In the following, we will explain the theoretical framework for such a description, which is based on Ref. [146].

6.1.1 Coupling Light into the Cavity

The first step is to consider the process of coupling light into the cavity. While it is possible to describe the cavity feeding by exciting with a quantum state of light externally, and

computing the quantum state of light that enters the cavity, this is an extensive task and is known as input-output theory, which mostly is formulated for special cases [147–150]. Instead, we consider a short classical electric field $\boldsymbol{E}_c$ that creates cavity photons that follow a certain quantum statistic. This interaction takes the form [145]

$$V_c(t) = \boldsymbol{d}_c \cdot \boldsymbol{E}_c b^\dagger + \text{H.c.}, \tag{6.2}$$

where $\boldsymbol{d}_c$ is the effective dipole moment of the cavity mode. Assuming that the electric fields are shorter than all other timescales, it is feasible to rewrite it as a sequence of delta pulses:

$$\boldsymbol{E}_c = \sum_j \boldsymbol{E}_c^j \delta(t - t_j). \tag{6.3}$$

Defining the pulse area Θ_j of the j-th pulse as:

$$\Theta_j = \frac{2\boldsymbol{d}_c \cdot \boldsymbol{E}_c^j}{\hbar}, \tag{6.4}$$

allows to rewrite Eq. (6.2) as

$$V_c = \sum_j \hbar \frac{\Theta_j}{2} b^\dagger \delta(t - t_j) + \text{H.c.} = \sum_j V_j \delta(t - t_j). \tag{6.5}$$

We can describe the effect of V_j by considering the DM before the pulse (ρ_{before}) and after the pulse (ρ_{after}) that acts at $t = t_j$, which are connected in the following way

$$\rho_{\text{after}}(t_j) = e^{-\frac{i}{\hbar}V_j} \rho_{\text{before}}(t_j) e^{\frac{i}{\hbar}V_j}. \tag{6.6}$$

With the identification $\alpha_j = -i\Theta_j/2$, one can rewrite $-\frac{i}{\hbar}V_j = \alpha_j b^\dagger - \alpha_j^* b$, such that Eq. (6.6) can be written in terms of the displacement operator Eq. (2.29):

$$\rho_{\text{after}}(t_j) = D(\alpha_j) \rho_{\text{before}}(t_j) D^\dagger(\alpha_j). \tag{6.7}$$

Thus, the excitation with an external classical electric field $\boldsymbol{E}_c^j$ can be expressed by a matrix multiplication at $t = t_j$, where the pulse area is determined by:

$$\Theta_j = 2|\alpha_j| = 2\sqrt{N}. \tag{6.8}$$

E.g., a 2π pulse is obtained with a mean photon number of $N \approx 10$. Without explicitly treating other interactions than Eq. (6.2), we generalize Eqs. (6.7) and (6.8) by exchanging the displacement operator with other operators, e.g. the squeezing operator Eq. (2.38) or combinations thereof, while the pulse area of this excitation is still determined by the mean photon number of the excitation according to $\Theta_j = 2\sqrt{N}$. If one would derive such a relation from an interaction Hamiltonian, one would be required to include a spontaneous parametric down-conversion type Hamiltonian, where the exact form of the Hamiltonian

would depend on the setup, i.e., how the cavity and the nonlinear medium are arranged. Also note that the identification of $2\sqrt{N}$ as pulse area not necessarily needs to be true, as this needs to be concluded from the interaction Hamiltonian. Here, however, we proceed with this approximation to get a general idea of the behavior, whereas a proper treatment is a subject of further research.

Eq. (6.7) can be rewritten and approximated by the use of the Baker–Campbell–Hausdorff (BCH) formula [151]:

$$e^{X}Ye^{-X} = \sum_{m=0}^{\infty} \frac{1}{m!} [X,Y]_m \quad \text{with} \quad [X,Y]_m = [X,[X,Y]_{m-1}] \quad \text{and} \quad [X,Y]_0 = Y. \tag{6.9}$$

This allows to rewrite Eq. (6.7) in terms of contributions up to first-order in α_j:

$$D(\alpha_j)\rho D^{\dagger}(\alpha_j) \approx \rho + \alpha_j[b^{\dagger},\rho] - \alpha_j^{*}[b,\rho]. \tag{6.10}$$

Similarly, this can be done for the squeezing operator Eq. (2.38) for terms up to the first order of ξ:

$$S(\xi)\rho S^{\dagger}(\xi) \approx \rho + \frac{1}{2}\xi^{*}[b^2,\rho] - \frac{1}{2}\xi[b^{\dagger 2},\rho]. \tag{6.11}$$

It becomes evident that weak coherent states $|\alpha| \ll 1$ are suitably described by single-photon excitation processes, given by the commutators $[b^{\dagger},\rho]$ and $[b,\rho]$. In contrast, squeezed states at least contribute with two-photon processes, as can already be seen from the squeezing operator. This, however, is a relevant conclusion when moving towards FWM with quantum states of light, as will become clear throughout this chapter.

6.1.2 Extracting the Four-Wave-Mixing Signal

In semiclassical treatments, FWM signals are often extracted by including the directional information of the electric fields, where one considers the $2\boldsymbol{k}_2 - \boldsymbol{k}_1$ direction for the FWM signal, which can either be obtained by a perturbative treatment for weak electric fields [152] or by spatial Fourier expansion [153]. Note that this was skipped in the previous chapter, since the PE is the dominant signal at $t = 2\tau$, so that this extraction process is not required. Another approach is phase cycling, where the electric fields $\boldsymbol{E}_1$ and $\boldsymbol{E}_2$ are assumed to have the phases φ_1 and φ_2, such that the FWM signal must carry the phase $2\varphi_2 - \varphi_1$ [154]. Phase cycling is usually applied when a single QD is considered, since an effective 0D structure does not have an emission direction. It is, however, more straightforward to use phase cycling rather than including directional information when considering the excitation with quantum states of light, since the designated phase φ_j directly translates into the quantum number:

$$\boldsymbol{E}_c^j \to \boldsymbol{E}_c^j \exp(-i\varphi_j) \quad \Leftrightarrow \quad \alpha_j \to \alpha_j \exp(-i\varphi_j) \quad \text{or} \quad \xi_j \to \xi_j \exp(-i\varphi_j). \tag{6.12}$$

Note that in the case of squeezed vacuum, the excitation of lowest possible order is a two-photon excitation, which is why the FWM phase in this case reads $\varphi_2 - \varphi_1$. The methodology is now to assign phases φ_1, φ_2, and φ_3 to the quantum numbers α_1, α_2, and α_3, such that after each excitation, one can filter elements that carry the respective phase, so that the considered elements have the phase $\varphi_3 + \varphi_2 - \varphi_1$ in a three-pulse setup, or $2\varphi_2 - \varphi_1$ in a two-pulse setup. This filtering is realized by deleting all elements from the DM that do not carry the designated phase, resulting in the matrix ρ_{FWM}. This, however, means that ρ_{FWM} formally is not a DM anymore, since it does not fulfill the required properties. Therefore, the application of phase cycling on the one hand allows to extract the FWM signal, but on the other hand prevents to obtain information that requires the full DM. The FWM signal is then obtained by computing the expectation value of the photon annihilation operator b with the phase-cycled DM ρ_{FWM}:

$$\langle b \rangle_{\mathrm{FWM}} = \mathrm{Tr}[b\rho_{\mathrm{FWM}}]. \tag{6.13}$$

6.2 Homogeneous Systems

To get a first idea of quantum FWM dynamics, we start with the consideration of homogeneous systems, which corresponds to a number of transitions with a uniform frequency distribution. For simplicity, the homogeneous system that we consider is a single TLS. Note that the consideration of a single TLS with band-gap frequency ω or the consideration of many TLS with band-gap frequencies ω and averaging over their optical properties does not make a difference in a semiclassical theory, since the presence of a TLS does not change the light field. This, however, does not hold true for the quantum-optical regime, which is why it is required to make this specification.

6.2.1 Analytical Treatment

In the following, we will calculate the FWM signal from a single TLS analytically excited by coherent states which are approximated using the BCH formula Eq. (6.10). For simplicity, we do not consider any optical detuning, i.e., $\nu = \omega$. For better readability, the DM gets and index that indicates how many pulses already excited. Applying the phase cycling to Eq. (6.10) with respect to the first pulse only allows for the term proportional to α_j^*, such that the transformation reads:

$$\rho_1(t = 0) = -\alpha_1^*[b, \rho_0]. \tag{6.14}$$

Starting from the ground state initially, i.e. $\rho_0 = |-, 0\rangle \langle -, 0|$ leads to

$$\rho_1(t = 0) = \alpha_1^* |-, 0\rangle \langle -, 1| \tag{6.15}$$

The time evolution from $t = 0$ to $t = \tau$ leads to

$$\rho_1(t = \tau) = \exp(iv\tau)\alpha_1^* \Big[\cos(g\tau) \left|-, 0\right\rangle \left\langle -, 1\right| + i \sin(g\tau) \left|-, 0\right\rangle \left\langle +, 0\right| \Big]. \tag{6.16}$$

Note that the phase factor $\exp(iv\tau)$ arises from the time evolution of the operator $\left|-, 0\right\rangle \left\langle -, 1\right|$ from $t = 0$ to $t = \tau$. The excitation of the second and third pulse with the proper phase cycling is achieved by:

$$\begin{aligned} \rho_3(t = \tau) &= [\alpha_3 b^\dagger, [\alpha_2 b^\dagger, \rho_1(t = \tau)]] \qquad (6.17) \\ &= \exp(iv\tau)\alpha_1^* \alpha_2 \alpha_3 \Big[\sqrt{2} \cos(g\tau) \left|-, 2\right\rangle \left\langle -, 1\right| - 2 \cos(g\tau) \left|-, 1\right\rangle \left\langle -, 0\right| \\ &\quad + \sqrt{2} i \sin(g\tau) \left|-, 2\right\rangle \left\langle +, 0\right| \Big]. \qquad (6.18) \end{aligned}$$

Considering the appearing operators $\left|-, 2\right\rangle \left\langle -, 1\right|$, $\left|-, 1\right\rangle \left\langle -, 0\right|$, and $\left|-, 2\right\rangle \left\langle +, 0\right|$, it is evident that the time evolution from $t = \tau$ to $t = t$ gives rise to an additional phase factor of $\exp(-iv(t - \tau))$, resulting in a global phase factor of $\exp(-iv(t - 2\tau))$. The full solution of the expectation value of b, i.e., the FWM signal, then reads

$$\begin{aligned} \langle b \rangle_{\mathrm{FWM}}(t) =& \mathrm{Tr}[b\rho_3(t)] \\ =& e^{-iv(t-2\tau)} \alpha_1^* \alpha_2 \alpha_3 \Big\{ 2 \cos(g\tau) \cos\Big(\sqrt{2} gt\Big) \cos(gt) - 2 \sin(g\tau) \cos\Big(\sqrt{2} gt\Big) \sin(gt) \\ &+ \sqrt{2} \cos(g\tau) \sin\Big(\sqrt{2} gt\Big) \sin(gt) + \sqrt{2} \sin(g\tau) \sin\Big(\sqrt{2} gt\Big) \cos(gt) \\ &- 2 \cos(g\tau) \cos(gt) \Big\}. \end{aligned} \tag{6.19}$$

This solution corresponds to an approximation for low excitation, as it only includes the process at the lowest rung of the JC ladder. It shows similarities with the solution obtained from a semiclassical theory [155] as e.g. the product of the displacements $\alpha_1^* \alpha_2 \alpha_3$, which correspond to the electric field amplitudes $E_1^* E_2 E_3$ in the semiclassical theory. Furthermore, the solutions from both theories show a phase factor of the form $\exp(-iv(t - 2\tau))$, which is responsible for the formation of PEs. Thus, we conclude that a FWM signal obtained from a fully quantized theory carries the phase factor $\exp(-iv(t - 2\tau))$, which predicts the formation of a PE obtained from the excitation with quantum states of light.

6.2.2 Numerical Simulations

After the analytical treatment for weak excitations, we move towards a numerical treatment of the full excitation. For this, we consider a similar pulse setup as in Chapter 5, i.e., we consider two pulses with phases φ_1 and φ_2 and a positive delay $\tau > 0$, such that the first pulse excites the system before the second pulse. We fix the first pulse as a coherent state with variable pulse area Θ_1 and consider different photon statistics for the second pulse,

but fix its pulse area to $\Theta_2 = \pi$, which translates to its mean photon number according to Eq. (6.8). We take into account losses in the same way as in Ref. [146] by including Lindblad terms Eq. (2.58) for the operators $L = \sqrt{\kappa}b$ and $L = \sqrt{\gamma}a$, with $\kappa = 50$ μeV and $\gamma = 2$ μeV. The coupling constant g that determines the time scale of the interaction is set to $g = 35$ μeV, which is a realistic value for QDs. Fig. 6.1 shows simulations of the FWM signal $\langle b \rangle_{\mathrm{FWM}}$ for different pulse areas Θ_1 on the y-axis, where in Fig. 6.1(a) a coherent state is used as second pulse, so that the phase cycling is done with respect to the phase $2\varphi_2 - \varphi_1$, while in (b) the second pulse is a squeezed vacuum state, such that the phase cycling is done according to $\varphi_2 - \varphi_1$ to describe the FWM response. It can be seen that merely changing the photon statistics of the incoming photons has a visible impact on the FWM dynamics.

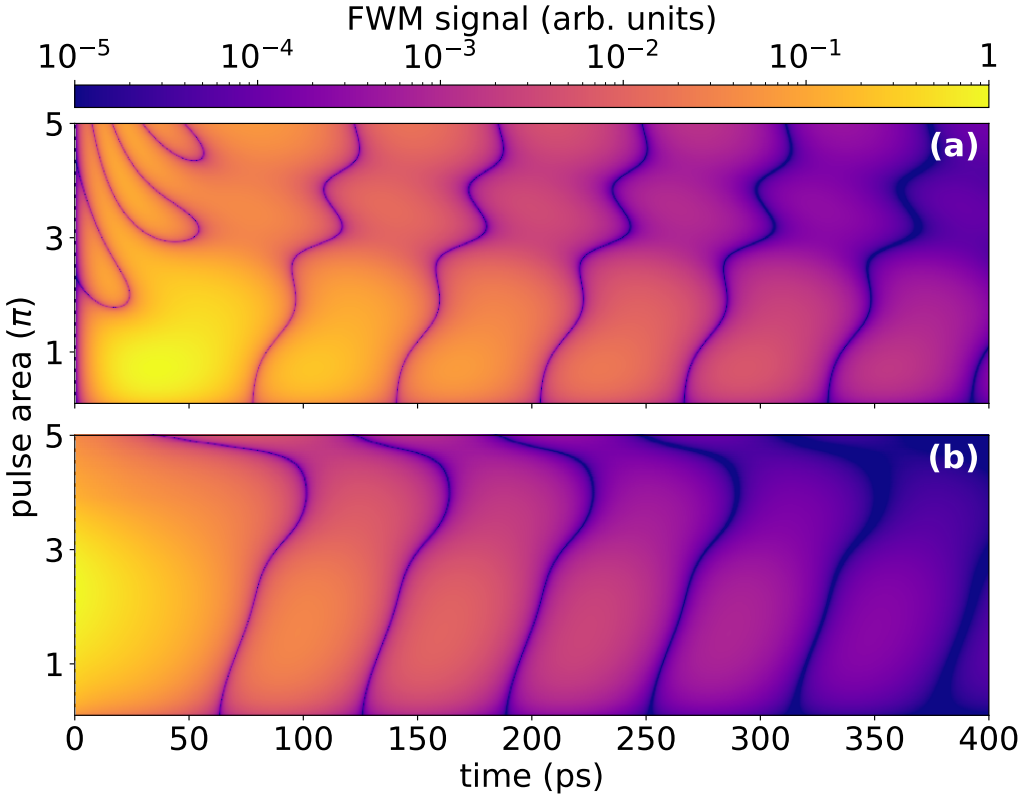

Figure 6.1: The FWM dynamics computed according to Eq. (6.13) is shown for different pulse setups, where the absolute value is shown. The first pulse is a coherent state and its pulse area is shown on the y-axis. The second pulse has an area of $\Theta_2 = \pi$ and is a (a) coherent state, (b) squeezed vacuum state. The FWM signal is shown on a logarithmic scale such that the dynamics at later times is more clearly visible.

6.3 Inhomogeneous Systems

As pointed out in Section 6.1, the Hamiltonian Eq. (6.1) that describes an inhomogeneously broadened system of QDs is similar to the Hamiltonian Eq. (4.1) for a two-band model. Thus, the number of states will increase exponentially with the number of Hilbert space dimensions according to Eq. (4.15). Here, however, we are especially interested in the behavior of different photon statistics, which makes the consideration of single-photon or two-photon excitations not feasible. Therefore, we will not compute the full problem of N_{TLS} QDs in a cavity interacting with a single quantum state of light, but rather, consider a single QD in a cavity interacting with a single quantum state of light ($N_{\mathrm{TLS}} = 1$), which we compute N times for different transition frequencies, leading to different optical detunings Δ. For this, we feed the cavity with two pulses at $t = 0$ ps and $t = 80$ ps according to Eq. (6.7), which leads to N different expectation values $\langle b \rangle_i$, with $i = 1, 2, ..., N$. Here, we do not perform phase cycling since the PE is assumed to be the dominant signal in this setup. The FWM signal is then obtained similar as in Eq. (5.17) by the sum of the single contributions weighted with a weighting function F, which is modeled by a Gaussian function. Here, however, we consider the expectation value of the material operator $\langle a \rangle_i$ to obtain a closer correspondence to the semiclassical case, such that the FWM signal is modeled as:

$$\langle a \rangle_{\mathrm{full}} = \sum_{i=1}^{N} F(\Delta_i) \langle a \rangle_i \, \mathrm{d}\Delta, \tag{6.20}$$

$$F(\Delta_i) = \frac{1}{\sqrt{2\pi\sigma^2}} \exp\left(-\frac{1}{2} \left(\frac{\Delta}{\sigma} \right)^2 \right). \tag{6.21}$$

This approximation overestimates the strength of the light, since not all photons can be absorbed. Furthermore, this approximation neglects certain processes, e.g., squeezed vacuum states can only lead to two-photon processes on a single QD, while they could lead to two single-photon processes when exciting several QDs. For future studies it is relevant to find a better approximation that overcomes the abovementioned disadvantages. Here, however, we use this approximation for a conceptual demonstration of the optical properties of inhomogeneous systems in the presence of quantum states of light.

Fig. 6.2 shows the PE amplitude simulated according to Eq. (6.20), where the first pulse is a coherent state whose pulse area is varied on the y-axis, while the second pulse is chosen as a coherent state in Fig. 6.2(a) and as a squeezed vacuum state in Fig. 6.2(b), with a pulse area of π in the respective cases. Here, the parameters are chosen the same as before except for the cavity loss, which is increased to $\kappa = 200$ μeV. The inhomogeneous broadening is modeled with $N = 1000$ and $\sigma = 1$ meV, where the frequency range from -3 meV to 3 meV is sampled. The PE amplitude shows a Rabi rotation as a function of the pulse area Θ_1, which is well known from a semiclassical treatment, see Chapter 5. Therefore, this is a direct demonstration that the behavior known from a semiclassical theory is included in a fully quantized description. It furthermore demonstrates that the application of different

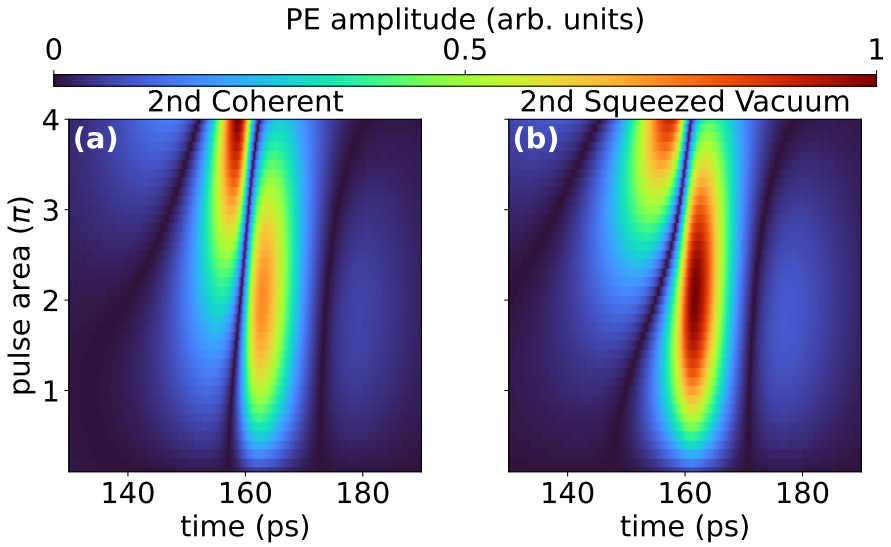

Figure 6.2: Numerical simulation of absolute value of the PE amplitude obtained from Eq. (6.20), where the first pulse is a coherent state with a pulse area Θ_1 that is depicted on the y-axis. The second state has a pulse area of $\Theta_2 = \pi$ and is chosen as (a) coherent state and (b) squeezed vacuum state.

quantum states of light as second pulse leads to a distinctly different behavior, as the shape and amplitude changes. We note that the introduced definition of the pulse area, which is motivated by the interaction picture and an identification of the displacement operator, does not match to the position of the maxima. Here, however, one needs to note that the temporal Rabi oscillations take a more complicated form and, e.g., result in a collapse and revival rather than in clear oscillations, see Fig. 2.8, which makes the comparison problematic. The mismatch has to be further analyzed to make a clearer conclusion.

6.4 Conclusions

We simulate FWM with quantum states of light and study the behavior of homogeneous and inhomogeneous systems, as well as the dependence on different quantum states of light. We demonstrate a distinct behavior when applying squeezed vacuum states for a FWM pulse sequence when compared to coherent states.

We demonstrate that inhomogeneously broadened systems lead to the formation of a PE, which can be seen analytically by approximating the expressions with the BCH formula and also results from a numerical treatment with arbitrary photon statistics. We conclude that different photon statistics lead to different PE amplitudes.

Altogether, these results are a first step towards a proper description of FWM with quantum states of light, where non-classical light and inhomogeneously broadened system are taken

into account. We mentioned a few points that can be improved for future studies, including a proper description of a single quantum state of light interacting with N QDs, where the complexity can be truncated with the cluster expansion [156], as well as a proper description of the coupling process of the light into the cavity.

Summary and Outlook 7

In this thesis, we model and analyze the interaction between semiconductor nanostructures and quantum light inside of optical microcavities. In the first half of this thesis, we consider the dynamics of material systems initially in their electronic ground state that are excited by single quantum field, while we focus on the excitation with multiple pulses in the second half of this thesis.

The first material system that we consider are Λ-type three-level systems, which are suited for the approximate description of charged or optically pumped excitonic resonances. We formulate a theoretical description that allows us to efficiently treat quantum states of light with high mean photon numbers and demonstrate electromagnetically induced transparency with quantum light, where we conclude that squeezed light enhances the effect, when used as probe field. We proceed with the formulation of a quantum polarization, which is a quantity that is always present in quantum excitations. We show its advantages over the classical polarization and use it to study the absorptive and dispersive behavior for coherent and squeezed light. Finally, we consider Λ-type three-level systems in lossy cavities and demonstrate that these losses can be used an advantage in order to achieve certain steady states in the electronic population. We explain this effect from the equations of motion and demonstrate it for different photon statistics.

The second material system that we treat are two-band models, which we describe as a collection of two-level system that follow a certain frequency distribution. This model is an established description of intrinsic semiconductor nanostructures such as semiconductor quantum wells, where the energetically highest valence and the energetically lowest conduction band are considered. We use the tight-binding approximation to model the energy dispersion in k-space and study effectively one-dimensional and two-dimensional structures, i.e., quantum wires and quantum wells. We use an approach based on the eigenvalue problem of the Hamiltonian to learn about properties of the system and obtain explicit expressions for the steady-state values of the ground-state probability. We perform numerical simulations to study the dynamics of the conduction-band occupation and consider excitations that are not resonant with respect to the band-gap energy, where we demonstrate special steady-state configurations. For future studies, the inclusion of the many-body Coulomb interaction is of high interest, which leads to the formation of bound electron-hole pair states, which are known as excitons. The study of excitons that form in response to quantum-optical excitations within a microcsopic description of the semiconductor nanostructure will give new insights into this topic.

The second half of this thesis concentrates on the description of wave-mixing experiments, that is to say, on multiple excitations that can be performed at different times. Therefore, this is an extension of the first half, where we considered a single excitation at the initial moment

of time. To demonstrate the capability of wave-mixing experiments, we start with analyzing experimental data obtained from four-wave-mixing experiments by using a semiclassical theory, where the light is described classically. Four-wave-mixing experiments performed on semiconductor quantum dots lead to the formation of a photon echo. We show that one can control this photon echo accurately in time by applying an optical control pulse, where we obtain an agreement between experimental data and our numerical simulations. Being able to control photon echoes optically is of a high relevance, as they are important for quantum memory protocols. We identify the main damping mechanism as the spatial averaging of the electric field amplitudes due to the detector. We demonstrate that one can bypass this damping mechanism by using spatial pulse shaping and conclude that the new main damping mechanism is the interaction with longitudinal acoustic phonons during the excitation process, where we find an agreement between our numerical simulations and experimental data.

We proceed with the combination of wave-mixing experiments and quantum-optical excitations, leading to quantum wave mixing. Here, we explain how such a system can be theoretically described and show simulations for homogeneous and inhomogeneous systems, where different quantum states of light lead to different results. This chapter is rather thought to be a summary of the current state which also explains required improvements for the theoretical description. One challenge is a proper description for the process of coupling light into the cavity, as well as a proper description for the coupling of the four-wave-mixing signal out of the cavity. This is a complicated task since the quantization of the electromagnetic field works differently in free space as compared to cavities. The main challenge is to find a suitable approximation method that allows to describe many quantum dots being coupled to the same cavity mode, since the complexity of an exact treatment is known to scale exponentially. This step is necessary since the approximation that we presented, in which we average over N quantum dots that all have their own cavity, neglects processes, for example that the two-photon component of a squeezed vacuum state can lead to two single-photon excitations in two quantum dots.

Summarizing, this thesis presents theoretical investigations of the interaction between semiconductor nanostructures and quantum light, where we discuss different systems and showcase applications. It demonstrates the relevance of four-wave-mixing experiments and gives a starting point for quantum wave mixing on homogeneous and inhomogeneous systems.

For future investigations, a number of studies is planned in close cooperation between theory and experiment with the general objective to study the nonlinear exciton dynamics in semiconductor nanostructures that are embedded in microcavities by using quantum-optical spectroscopy methods. Here, the focus lays on both, generating non-classicality and exciting with non-classical states of light, which builds up on the results shown in this thesis. The planned studies can be divided in three topics.

The first topic deals with the investigation of excitons from semiconductor quantum well structures by using transient four-wave mixing and exploring the generated non-classicality. Here, different multi-level schemes such as diamond schemes for the description

exciton-biexciton systems [157, 158] or Λ-systems for the description of charged exciton complexes will be considered. In addition, control pulses can be applied to modify the response.

The second topic is on photon echoes obtained from inhomogeneous ensembles of semiconductor quantum dots. Due to their negligible radiative decay, they are a promosing candidate for quantum-state tomography methods, which will be used to study non-classicality in the emitted light. Here, we are especially interested in the weak coherent interaction between the excitons and the coupling between excitons and a microcavity mode. Both coupling processes are expected to be included in the four-wave-mixing response and should be distinguishable by using quantum-state tomography.

The third topic deals with the excitation by squeezed light in a wave-mixing protocol as one of the pulses for the four-wave mixing or as a control pulse. As already demonstrated in Chapter 6, the application of squeezed states significantly modifies the four-wave-mixing response. We are interested in the interplay between photonic correlations and matter correlations. On the one hand, this can be used to resolve excitonic interactions and on the other hand, this can allow for an information protocol by storing and retrieving the photonic correlations from the squeezed state of light. This will be combined with photon-echo protocols to explore new possibilities in quantum memories.

Altogether, we plan to exploit non-classicality generated in four-wave-mixing schemes for both, homogeneous systems such as semiconductor quantum wells and inhomogeneous systems such as quantum dot ensembles, as well as to use non-classical states of light such as squeezed light to move towards the creation of new resources for quantum devices such as quantum memories.

Bibliography

[1] M. Kira and S. W. Koch, *Semiconductor Quantum Optics* (Cambridge University Press, Cambridge, 2012).

[2] M. Bondani, A. Allevi, G. Zambra, M. G. A. Paris, and A. Andreoni, Sub-shot-noise photon-number correlation in a mesoscopic twin beam of light, Phys. Rev. A **76**, 013833 (2007).

[3] A. Allevi, S. Olivares, and M. Bondani, Measuring high-order photon-number correlations in experiments with multimode pulsed quantum states, Phys. Rev. A **85**, 063835 (2012).

[4] E. D. Lopaeva, I. Ruo Berchera, I. P. Degiovanni, S. Olivares, G. Brida, and M. Genovese, Experimental Realization of Quantum Illumination, Phys. Rev. Lett. **110**, 153603 (2013).

[5] M. O. Scully and M. S. Zubairy, *Quantum Optics* (Cambridge University Press, Cambridge, 1997).

[6] S. Mukamel et al., Roadmap on quantum light spectroscopy, J. Phys. B: At. Mol. Opt. Phys. **53**, 072002 (2020).

[7] S. W. Koch, M. Kira, G. Khitrova, and H. M. Gibbs, Semiconductor excitons in new light, Nature Mater. **5**, 523 (2006).

[8] M. Kira and S. W. Koch, Quantum-optical spectroscopy of semiconductors, Phys. Rev. A **73**, 013813 (2006).

[9] A. Carmele, A. Knorr, and M. Richter, Photon statistics as a probe for exciton correlations in coupled nanostructures, Phys. Rev. B **79**, 035316 (2009).

[10] M. Aßmann and M. Bayer, Nonlinearity sensing via photon-statistics excitation spectroscopy, Phys. Rev. A **84**, 053806 (2011).

[11] M. Kira, S. W. Koch, R. P. Smith, A. E. Hunter, and S. T. Cundiff, Quantum spectroscopy with Schrödinger-cat states, Nature Phys. **7**, 799 (2011).

[12] M. Mootz, M. Kira, S. W. Koch, A. E. Almand-Hunter, and S. T. Cundiff, Characterizing biexciton coherences with quantum spectroscopy, Phys. Rev. B **89**, 155301 (2014).

[13] K. E. Dorfman, F. Schlawin, and S. Mukamel, Nonlinear optical signals and spectroscopy with quantum light, Rev. Mod. Phys. **88**, 045008 (2016).

[14] F. Schlawin, Entangled photon spectroscopy, J. Phys. B: At. Mol. Opt. Phys. **50**, 203001 (2017).

[15] K. E. Dorfman and S. Mukamel, Multidimensional photon correlation spectroscopy of cavity polaritons, Proc. Natl. Acad. Sci. U.S.A. **115**, 1451 (2018).

[16] C. S. Muñoz and F. Schlawin, Photon Correlation Spectroscopy as a Witness for Quantum Coherence, Phys. Rev. Lett. **124**, 203601 (2020).

[17] J. J. Hopfield, Theory of the Contribution of Excitons to the Complex Dielectric Constant of Crystals, Phys. Rev. **112**, 1555 (1958).

[18] A. H. Zewail, *Femtochemistry: Ultrafast Dynamics of the Chemical Bond* (World Scientific, Singapore, 1994), Vols. I and II.

[19] U. Höfer, I. L. Shumay, C. Reuß, U. Thomann, W. Wallauer, and T. Fauster, Time-Resolved Coherent Photoelectron Spectroscopy of Quantized Electronic States on Metal Surfaces, Science **277**, 1480 (1997).

[20] D. G. Lidzey, D. D. C. Bradley, M. S. Skolnick, T. Virgili, S. Walker, and D. M. Whittaker, Strong exciton–photon coupling in an organic semiconductor microcavity, Nature **395**, 53 (1998).

[21] A. M. van Oijen, M. Ketelaars, J. Kohler, T. J. Aartsma, and J. Schmidt, Unraveling the Electronic Structure of Individual Photosynthetic Pigment-Protein Complexes, Science **285**, 400 (1999).

[22] G. Khitrova, H. M. Gibbs, F. Jahnke, M. Kira, and S. W. Koch, Nonlinear optics of normal-mode-coupling semiconductor microcavities, Rev. Mod. Phys. **71**, 1591 (1999).

[23] H. Haug and S. W. Koch, *Quantum Theory of the Optical and Electronic Properties of Semiconductors*, 5th ed. (World Scientific, Singapore, 2009).

[24] F. Wang, G. Dukovic, L. E. Brus, and T. F. Heinz, The Optical Resonances in Carbon Nanotubes Arise from Excitons, Science **308**, 838 (2005).

[25] N. E. Holt, D. Zigmantas, L. Valkunas, X.-P. Li, K. K. Niyogi, and G. R. Fleming, Carotenoid Cation Formation and the Regulation of Photosynthetic Light Harvesting, Science **307**, 433 (2005).

[26] S. Bellafiore, F. Bameche, G. Peltier, and J.-D. Rochaix, State transitions and light adaptation require chloroplast thylakoid protein kinase STN7, Nature **433**, 892 (2005).

[27] P. Ye and Y. R. Shen, Transient four-wave mixing and coherent transient optical phenomena, Phys. Rev. A **25**, 2183 (1982).

[28] Y. R. Shen, *The Principles of Nonlinear Optics* (Wiley, New York, 1984).

[29] R. W. Boyd, *Nonlinear Optics*, 3rd ed. (Academic Press, San Diego, 2008).

[30] S. Mukamel, *Principles of Nonlinear Optical Spectroscopy* (Oxford Univ. Press, New York, 1995).

[31] M. Wegener, *Extreme Nonlinear Optics* (Springer, Berlin, 2005).

[32] J. Hegarty, M. D. Sturge, A. C. Gossard, and W. Wiegmann, Resonant degenerate four-wave mixing in GaAs multiquantum well structures, Appl. Phys. Lett. **40**, 132 (1982).

[33] D. A. B. Miller, D. S. Chemla, D. J. Eilenberger, P. W. Smith, A. C. Gossard, and W. Wiegmann, Degenerate four-wave mixing in room-temperature GaAs/GaAlAs multiple quantum well structures, Appl. Phys. Lett. **42**, 925 (1983).

[34] L. Schultheis, J. Kuhl, A. Honold, and C. W. Tu, Picosecond Phase Coherence and Orientational Relaxation of Excitons in GaAs, Phys. Rev. Lett. **57**, 1797 (1986).

[35] L. Schultheis, A. Honold, J. Kuhl, K. Köhler, and C. W. Tu, Optical dephasing of homogeneously broadened two-dimensional exciton transitions in GaAs quantum wells, Phys. Rev. B **34**, 9027(R) (1986).

[36] A. Honold, L. Schultheis, J. Kuhl, and C. W. Tu, Collision broadening of two-dimensional excitons in a GaAs single quantum well, Phys. Rev. B **40**, 6442(R) (1989).

[37] K. Leo, M. Wegener, J. Shah, D. S. Chemla, E. O. Göbel, T. C. Damen, S. Schmitt-Rink, and W. Schäfer, Effects of coherent polarization interactions on time-resolved degenerate four-wave mixing, Phys. Rev. Lett. **65**, 1340 (1990).

[38] M. Wegener, D. S. Chemla, S. Schmitt-Rink, and W. Schäfer, Line shape of time-resolved four-wave mixing, Phys. Rev. A **42**, 5675 (1990).

[39] M. Koch, J. Feldmann, G. von Plessen, E. O. Göbel, P. Thomas, and K. Köhler, Quantum beats versus polarization interference: An experimental distinction, Phys. Rev. Lett. **69**, 3631 (1992).

[40] J. Feldmann, T. Meier, G. von Plessen, M. Koch, E. O. Göbel, P. Thomas, G. Bacher, C. Hartmann, H. Schweizer, W. Schäfer, and H. Nickel, Coherent dynamics of excitonic wave packets, Phys. Rev. Lett. **70**, 3027 (1993).

[41] V. G. Lyssenko, J. Erland, I. Balslev, K.-H. Pantke, B. S. Razbirin, and J. M. Hvam, Nature of nonlinear four-wave-mixing beats in semiconductors, Phys. Rev. B **48**, 5720(R) (1993).

[42] A. Leitenstorfer, A. Lohner, K. Rick, P. Leisching, T. Elsaesser, T. Kuhn, F. Rossi, W. Stolz, and K. Ploog, Excitonic and free-carrier polarizations of bulk GaAs studied by femtosecond coherent spectroscopy, Phys. Rev. B **49**, 16372 (1994).

[43] M. Koch, R. Hellmann, G. Bastian, J. Feldmann, E. O. Göbel, and P. Dawson, Enhanced energy and phase relaxation of excitons in the presence of bare electrons, Phys. Rev. B **51**, 13887(R) (1995).

[44] S. T. Cundiff, M. Koch, W. H. Knox, J. Shah, and W. Stolz, Optical Coherence in Semiconductors: Strong Emission Mediated by Nondegenerate Interactions, Phys. Rev. Lett. **77**, 1107 (1996).

[45] X. Chen, W. J. Walecki, O. Buccafusca, D. N. Fittinghoff, and A. L. Smirl, Temporally and spectrally resolved amplitude and phase of coherent four-wave-mixing emission from GaAs quantum wells, Phys. Rev. B **56**, 9738 (1997).

[46] K. B. Ferrio and D. G. Steel, Raman Quantum Beats of Interacting Excitons, Phys. Rev. Lett. **80**, 786 (1998).

[47] M. Phillips and H. Wang, Coherent oscillation in four-wave mixing of interacting excitons, Solid State Commun. **111**, 317 (1999).

[48] A. L. Smirl, M. J. Stevens, X. Chen, and O. Buccafusca, Heavy-hole and light-hole oscillations in the coherent emission from quantum wells: Evidence for exciton-exciton correlations, Phys. Rev. B **60**, 8267 (1999).

[49] J. M. Shacklette and S. T. Cundiff, Role of excitation-induced shift in the coherent optical response of semiconductors, Phys. Rev. B **66**, 045309 (2002).

[50] S. T. Cundiff, Coherent spectroscopy of semiconductors, Opt. Express **16**, 4639 (2008).

[51] P. A. M. Dirac, The quantum theory of the emission and absorption of radiation, Proc. R. Soc. Lond. A **114**, 243 (1927).

[52] E. Fermi, Quantum Theory of Radiation, Rev. Mod. Phys. **4**, 87 (1932).

[53] R. Loudon *The Theory of Quantum Light*, 3rd edition (Oxford University Press, Oxford, 2000).

[54] P. Meystre and M. Sargent III, *Elements of Quantum Optics*, 4th edition (Springer, Berlin, 2007).

[55] D. F. Walls and G. J. Milburn, *Quantum Optics*, 2nd edition (Springer, Berlin, 2008).

[56] G. Grynberg, A. Aspect, and C. Fabre, *Introduction to Quantum Optics: From the Semi-classical Approach to Quantized Light*, (Cambridge University Press, Cambridge, 2010).

[57] R. J. Glauber, Coherent and Incoherent States of the Radiation Field, Phys. Rev. **131**, 2766 (1963).

[58] E. Wigner, On the Quantum Correction For Thermodynamic Equilibrium, Phys. Rev. **40**, 794 (1932).

[59] L. Barsotti, J. Harms, and R. Schnabel, Squeezed vacuum states of light for gravitational wave detectors, Rep. Prog. Phys. **82**, 016905 (2019).

[60] L.-A. Wu, H. J. Kimble, J. L. Hall, and H. Wu, Generation of Squeezed States by Parametric Down Conversion, Phys. Rev. Lett. **57**, 2520 (1986).

[61] T. Sh. Iskhakov, A. M. Pérez, K. Yu. Spasibko, M. V. Chekhova, and G. Leuchs, Super-bunched bright squeezed vacuum state, Opt. Lett. **37**, 1919 (2012).

[62] A. M. Pérez, T. Sh. Iskhakov, P. R. Sharapova, S. Lemieux, O. V. Tikhonova, M. V. Chekhova, and G. Leuchs, Bright squeezed-vacuum source with 1.1 spatial mode, Opt. Lett. **39**, 2403 (2014).

[63] U. L. Andersen, T. Gehring, C. Marquardt, and G. Leuchs, 30 years of squeezed light generation, Phys. Scr. **91**, 053001 (2016).

[64] R. E. Slusher, L. W. Hollberg, B. Yurke, J. C. Mertz, and J. F. Valley, Observation of Squeezed States Generated by Four-Wave Mixing in an Optical Cavity, Phys. Rev. Lett. **55**, 2409 (1985).

[65] S. F. Pereira, M. Xiao, H. J. Kimble, and J. L. Hall, Generation of squeezed light by intracavity frequency doubling, Phys. Rev. A **38**, 4931 (1988).

[66] M. Bohmann and E. Agudelo, Phase-Space Inequalities Beyond Negativities, Phys. Rev. Lett. **124**, 133601 (2020).

[67] N. Biagi, M. Bohmann, E. Agudelo, M. Bellini, and A. Zavatta, Experimental Certification of Nonclassicality via Phase-Space Inequalities, Phys. Rev. Lett. **126**, 023605 (2021).

[68] G. Lindblad, On the generators of quantum dynamical semigroups, Commun. Math. Phys. **48**, 119 (1976).

[69] E. T. Jaynes and F. W. Cummings, Comparison of quantum and semiclassical radiation theories with application to the beam maser, Proc. IEEE **51**, 89 (1963).

[70] P. Meystre and M. S. Zubairy, Squeezed states in the Jaynes-Cummings model, Phys. Lett. A **89**, 390 (1982).

[71] B. W. Shore and P. L. Knight, The Jaynes-Cummings Model, J. Mod. Opt. **40**, 1195 (1993).

[72] J. H. Eberly, N. B. Narozhny, and J. J. Sanchez-Mondragon, Periodic Spontaneous Collapse and Revival in a Simple Quantum Model, Phys. Rev. Lett. **44**, 1323 (1980).

[73] G. Rempe, H. Walther, and N. Klein, Observation of quantum collapse and revival in a one-atom maser, Phys. Rev. Lett. **58**, 353 (1987).

[74] M. Fleischhauer and W. P. Schleich, Revivals made simple: Poisson summation formula as a key to the revivals in the Jaynes-Cummings model, Phys. Rev. A **47**, 4258 (1993).

[75] J. L. Tomaino, A. D. Jameson, Y.-S. Lee, G. Khitrova, H. M. Gibbs, A. C. Klettke, M. Kira, and S. W. Koch, Terahertz Excitation of a Coherent Λ-Type Three-Level System of Exciton-Polariton Modes in a Quantum-Well Microcavity, Phys. Rev. Lett. **108**, 267402 (2012).

[76] A. C. Klettke, M. Kira, S. W. Koch, J. L. Tomaino, A. D. Jameson, Y.-S. Lee, G. Khitrova, and H. M. Gibbs, Terahertz excitations of lambda systems in a semiconductor microcavity, Phys. Status Solidi C **10**, 1222 (2013).

[77] X. Xu, B. Sun, P. R. Berman, D. G. Steel, A. S. Bracker, D. Gammon, and L. J. Sham, Coherent population trapping of an electron spin in a single negatively charged quantum dot, Nature Phys. **4**, 692 (2008).

[78] K. G. Lagoudakis, K. A. Fischer, T. Sarmiento, P. L. McMahon, M. Radulaski, J. L. Zhang, Y. Kelaita, C. Dory, K. Müller, and J. Vučković, Observation of Mollow Triplets with Tunable Interactions in Double Lambda Systems of Individual Hole Spins, Phys. Rev. Lett. **118**, 013602 (2017).

[79] A. I. Lvovsky, B. Sanders, and W. Tittel, Optical quantum memory, Nat. Photonics **3**, 706 (2009).

[80] C. Simon, M. Afzelius, J. Appel, A. Boyer de la Giroday, S. J. Dewhurst, N. Gisin, C. Y. Hu, F. Jelezko, S. Kröll, J. H. Müller et al., Quantum memories, Eur. Phys. J. D **58**, 1 (2010).

[81] X.-L. Pang, A.-L. Yang, J.-P. Dou, H. Li, C.-N. Zhang, E. Poem, D. J. Saunders, H. Tang, J. Nunn, I. A. Walmsley, and X.-M. Jin, A hybrid quantum memory-enabled network at room temperature, Sci. Adv. **6**, eaax1425 (2020).

[82] N. Sangouard, C. Simon, H. Riedmatten, and N. Gisin, Quantum repeaters based on atomic ensembles and linear optics, Rev. Mod. Phys. **83**, 33 (2011).

[83] Y. Zuo, B. Li, Y. Zhao, Y. Jiang, Y.-C. Chen, P. Chen, G.-B. Jo, J. Liu, and S. Du, All-optical neural network with nonlinear activation functions, Optica **6**, 1132 (2019).

[84] S. E. Harris, J. E. Field, and A. Imamoğlu, Nonlinear optical processes using electromagnetically induced transparency, Phys. Rev. Lett. **64**, 1107 (1990).

[85] K.-J. Boller, A. Imamoğlu, and S. E. Harris, Observation of electromagnetically induced transparency, Phys. Rev. Lett. **66**, 2593 (1991).

[86] M. Fleischhauer, A. Imamoglu, and J. P. Marangos, Electromagnetically induced transparency: Optics in coherent media, Rev. Mod. Phys. **77**, 633 (2005).

[87] A. H. Safavi-Naeini, T. P. Mayer Alegre, J. Chan, M. Eichenfield, M. Winger, Q. Lin, J. T. Hill, D. E. Chang, and O. Painter, Electromagnetically induced transparency and slow light with optomechanics, Nature **472**, 69 (2011).

[88] I. Novikova, R. L. Walsworth, Y. Xiao, Electromagnetically induced transparency-based slow and stored light in warm atoms, Laser Photon. Rev. **6**, 333 (2012).

[89] P. M. Radmore and P. L. Knight, Population trapping and dispersion in a three-level system, J. Phys. B **15**, 561 (1982).

[90] K. Bergmann, H. Theuer, and B. W. Shore, Coherent population transfer among quantum states of atoms and molecules, Rev. Mod. Phys. **70**, 1003 (1998).

[91] H. Rose, D. V. Popolitova, O. V. Tikhonova, T. Meier, and P. R. Sharapova, Dark-state and loss-induced phenomena in the quantum-optical regime of Λ-type three-level systems, Phys. Rev. A **103**, 013702 (2021).

[92] H. Rose, O. V. Tikhonova, T. Meier, and P. R. Sharapova, Steady states of Λ-type three level systems excited by quantum light with various photon statistics in lossy cavities, New J. Phys. **24**, 063020 (2022).

[93] H. Rose, O. V. Tikhonova, T. Meier, and P. R. Sharapova, Theoretical analysis of correlations between two quantum fields exciting a three-level system using the cluster-expansion approach, Proc. SPIE **11999**, 1199905 (2022).

[94] S. A. Schäffer, B. T. R. Christensen, M. R. Henriksen, and J. W. Thomsen, Dynamics of bad-cavity-enhanced interaction with cold Sr atoms for laser stabilization, Phys. Rev. A **96**, 013847 (2017).

[95] B. Dayan, A. S. Parkins, T. Aok, E. P. Ostby, K. J. Vahala, and H. J. Kimble, A Photon Turnstile Dynamically Regulated by One Atom, Science **319**, 1062 (2008).

[96] J. I. Cirac, Interaction of a two-level atom with a cavity mode in the bad-cavity limit, Phys. Rev. A **46**, 4354 (1992).

[97] J. I. Cirac, M. Lewenstein, and P. Zoller, Laser cooling a trapped atom in a cavity: Bad-cavity limit, Phys. Rev. A **51**, 1650 (1995).

[98] L. Giannelli, T. Schmit, T. Calarco, C. P. Koch, S. Ritter, and G. Morigi, Optimal storage of a single photon by a single intra-cavity atom, New J. Phys. **20**, 105009 (2018).

[99] J.-H. An, M. Feng, and C. H. Oh, Quantum-information processing with a single photon by an input-output process with respect to low-Q cavities, Phys. Rev. A **79**, 032303 (2009).

[100] Q. Chen and M. Feng, Quantum-information processing in decoherence-free subspace with low-Q cavities, Phys. Rev. A **82**, 052329 (2010).

[101] S.-L. Su, Q. Guo, L. Zhu, H.-F. Wang, and S. Zhang, Atomic quantum information processing in low-Q cavity in the intermediate coupling region, J. Opt. Soc. Am. B **29**, 2827 (2012).

[102] A. S. Sørensen and K. Mølmer, Entangling atoms in bad cavities, Phys. Rev. A **66**, 022314 (2002).

[103] S. Franke, S. Hughes, M. K. Dezfouli, P. T. Kristensen, K. Busch, A. Knorr, and M. Richter, Quantization of Quasinormal Modes for Open Cavities and Plasmonic Cavity Quantum Electrodynamics, Phys. Rev. Lett. **122**, 213901 (2019).

[104] A. Karlsson, F. Francica, J. Piilo, and F. Plastina, Quantum Zeno-type effect and non-Markovianity in a three-level system, Sci. Rep. **6**, 39061 (2016).

[105] R. Lin, R. Rosa-Medina, F. Ferri, F. Finger, K. Kroeger, T. Donner, T. Esslinger, and R. Chitra, Dissipation-Engineered Family of Nearly Dark States in Many-Body Cavity-Atom Systems, Phys. Rev. Lett. **128**, 153601 (2022).

[106] V. V. Temnov and U. Woggon, Superradiance and Subradiance in an Inhomogeneously Broadened Ensemble of Two-Level Systems Coupled to a Low-Q Cavity, Phys. Rev. Lett. **95**, 243602 (2005).

[107] B. Liu, P. Rai, J. Grezmak, R. J. Twieg, and K. D. Singer, Coupling of exciton-polaritons in low-Q coupled microcavities beyond the rotating wave approximation, Phys. Rev. B **92**, 155301 (2015).

[108] H. Rose, A. N. Vasil'ev, O. V. Tikhonova, T. Meier, and P. R. Sharapova, Excitation of an electronic band structure by a single-photon Fock state, Zenodo (2021). https://doi.org/10.5281/zenodo.5774986

[109] H. Rose, A. N. Vasil'ev, O. V. Tikhonova, T. Meier, and P. R. Sharapova, Quantum-optical excitations of semiconductor nanostructures in a microcavity using a two-band model and a single-mode quantum field (submitted to Phys. Rev. A)

[110] M. Tavis and F. W. Cummings, Exact Solution for an N-Molecule—Radiation-Field Hamiltonian, Phys. Rev. **170**, 379 (1968).

[111] K. J. Blow, R. Loudon, S. J. D. Phoenix, and T. J. Shepherd, Continuum fields in quantum optics, Phys. Rev. A **42**, 4102 (1990).

[112] O. Tsyplyatyev and D. Loss, Dynamics of the inhomogeneous Dicke model for a single-boson mode coupled to a bath of nonidentical spin-1/2 systems, Phys. Rev. A **80**, 023803 (2009).

[113] O. Tsyplyatyev and D. Loss, Classical and quantum regimes of the inhomogeneous Dicke model and its Ehrenfest time, Phys. Rev. B **82**, 024305 (2010).

[114] S. Bochner and K. Chandrasekharan, *Fourier Transforms* (Princeton University Press, Princeton, 1949).

[115] D. S. Dovzhenko, S. V. Ryabchuk, Y. P. Rakovich, and I. R. Nabiev, Light-matter interaction in the strong coupling regime: configurations, conditions, and applications, Nanoscale **10**, 3589 (2018).

[116] *Handbook of Mathematical Functions with Formulas, Graphs, and Mathematical Tables*, edited by M. Abramowitz and I. A. Stegun, (Dover, New York, 1972).

[117] R. M. Corless, G. H. Gonnet, D. E. G. Hare, D. J. Jeffrey, and D. E. Knuth, On the Lambert W function, Adv. Comput. Math. **5**, 329 (1996).

[118] P. Lodahl, S. Mahmoodian, and S. Stobbe, Interfacing single photons and single quantum dots with photonic nanostructures, Rev. Mod. Phys. **87**, 347 (2015).

[119] M. Bayer, Bridging Two Worlds: Colloidal versus Epitaxial Quantum Dots, Ann. Phys. **531**, 1900039 (2019).

[120] T. Meier, P. Thomas, and S. W. Koch, *Coherent Semiconductor Optics: From Basic Concepts to Nanostructure Applications* (Springer, New York, 2007).

[121] A. N. Kosarev, H. Rose, S. V. Poltavtsev, M. Reichelt, C. Schneider, M. Kamp, S. Höfling, M. Bayer, T. Meier, and I. A. Akimov, Accurate photon echo timing by optical freezing of exciton dephasing and rephasing in quantum dots, Commun. Phys. **3**, 228 (2020).

[122] M. Reichelt, H. Rose, A. N. Kosarev, S. V. Poltavtsev, M. Bayer, I. A. Akimov, C. Schneider, M. Kamp, S. Höfling, and T. Meier, Controlling the emission time of photon echoes by optical freezing of exciton dephasing and rephasing in quantum-dot ensembles, Proc. SPIE **11684**, 116840X (2021).

[123] S. Grisard, H. Rose, A. V. Trifonov, R. Reichhardt, D. E. Reiter, M. Reichelt, C. Schneider, M. Kamp, S. Höfling, M. Bayer, T. Meier, and I. A. Akimov, Multiple Rabi rotations of trions in InGaAs quantum dots observed by photon echo spectroscopy with spatially shaped laser pulses, arXiv:2205.07771

[124] L. Allen and J. H. Eberly, *Optical Resonance and Two-Level Atoms* (Wiley, New York, 1975).

[125] P. Borri, W. Langbein, S. Schneider, U. Woggon, R. L. Sellin, D. Ouyang, and D. Bimberg, Ultralong Dephasing Time in InGaAs Quantum Dots, Phys. Rev. Lett. **87**, 157401 (2001).

[126] S. V. Poltavtsev, M. Salewski, Y. V. Kapitonov, I. A. Yugova, I. A. Akimov, C. Schneider, M. Kamp, S. Höfling, D. R. Yakovlev, A. V. Kavokin, and M. Bayer, Photon echo transients from an inhomogeneous ensemble of semiconductor quantum dots, Phys. Rev. B **93**, 121304(R) (2016).

[127] W. Tittel, M. Afzelius, T. Chaneliére, R. Cone, S. Kröll, S. Moiseev, and M. Sellars, Photon-echo quantum memory in solid state systems, Laser Photon. Rev. **4**, 244 (2009).

[128] V. Damon, M. Bonarota, A. Louchet-Chauvet, T. Chanelière, and J.-L. Le Gouët, Revival of silenced echo and quantum memory for light, New J. Phys. **13**, 093031 (2011).

[129] D. L. McAuslan, P. M. Ledingham, W. R. Naylor, S. E. Beavan, M. P. Hedges, M. J. Sellars, and J. J. Longdell, Photon-echo quantum memories in inhomogeneously broadened two-level atoms, Phys. Rev. A **84**, 022309 (2011).

[130] F. Bussières, N. Sangouard, M. Afzelius, H. de Riedmatten, C. Simon, and W. Tittel, Prospective applications of optical quantum memories, J. Mod. Opt. **60**, 1519 (2013).

[131] M. R. Klaßen and D. E. Reiter, Optical Signals to Monitor the Dynamics of Phonon-Modified Rabi Oscillations in a Quantum Dot, Ann. Phys. **533** 2100086, (2021).

[132] J. Förstner, C. Weber, J. Danckwerts, and A. Knorr, Phonon-Assisted Damping of Rabi Oscillations in Semiconductor Quantum Dots, Phys. Rev. Lett. **91**, 127401 (2003).

[133] M. Glässl, A. Vagov, S. Lüker, D. E. Reiter, M. D. Croitoru, P. Machnikowski, V. M. Axt, and T. Kuhn, Long-time dynamics and stationary nonequilibrium of an optically driven strongly confined quantum dot coupled to phonons, Phys. Rev. B **84**, 195311 (2011).

[134] D. E. Reiter, Time-resolved pump-probe signals of a continuously driven quantum dot affected by phonons, Phys. Rev. B **95**, 125308 (2017).

[135] C. Roy and S. Hughes, Influence of Electron–Acoustic-Phonon Scattering on Intensity Power Broadening in a Coherently Driven Quantum-Dot–Cavity System, Phys. Rev. X **1**, 021009 (2011).

[136] P. Kaer, T. R. Nielsen, P. Lodahl, A.-P. Jauho, and J. Mørk, Microscopic theory of phonon-induced effects on semiconductor quantum dot decay dynamics in cavity QED, Phys. Rev. B **86**, 085302 (2012).

[137] A. Nazir and D. P. S. McCutcheon, Modelling exciton–phonon interactions in optically driven quantum dots, J. Phys.: Condens. Matter **28**, 103002 (2016).

[138] P. Karwat and P. Machnikowski, Decay and persistence of spatial coherence during phonon-assisted relaxation in double quantum dots, Phys. Rev. B **91**, 125428 (2015).

[139] J. Iles-Smith and A. Nazir, Quantum correlations of light and matter through environmental transitions, Optica **3**, 207 (2016).

[140] M. Glässl and V. M. Axt, Polarization dependence of phonon influences in exciton-biexciton quantum dot systems, Phys. Rev. B **86**, 245306 (2012).

[141] M. Cygorek, A. M. Barth, F. Ungar, A. Vagov, and V. M. Axt, Nonlinear cavity feeding and unconventional photon statistics in solid-state cavity QED revealed by many-level real-time path-integral calculations, Phys. Rev. B **96**, 201201(R) (2017).

[142] P. Borri, W. Langbein, S. Schneider, U. Woggon, R. L. Sellin, D. Ouyang, and D. Bimberg, Rabi oscillations in the excitonic ground-state transition of InGaAs quantum dots, Phys. Rev. B **66**, 081306(R), (2002).

[143] K. Jürgens, F. Lengers, D. Groll, D. E. Reiter, D. Wigger, and T. Kuhn, Comparison of the semiclassical and quantum optical field dynamics in a pulse-excited optical cavity with a finite number of quantum emitters, Phys. Rev. B **104**, 205308 (2021).

[144] S. Weichselbaumer, M. Zens, C. W. Zollitsch, M. S. Brandt, S. Rotter, R Gross, and H. Huebl, Echo Trains in Pulsed Electron Spin Resonance of a Strongly Coupled Spin Ensemble, Phys. Rev. Lett. **125**, 137701 (2020).

[145] J. Kasprzak, S. Reitzenstein, E. A. Muljarov, C. Kistner, C. Schneider, M. Strauss, S. Höfling, A. Forchel, and W. Langbein, Up on the Jaynes–Cummings ladder of a quantum-dot/microcavity system, Nature Mater. **9**, 304 (2010).

[146] D. Groll, D. Wigger, K. Jürgens, T. Hahn, C. Schneider, M. Kamp, S. Höfling, J. Kasprzak, and T. Kuhn, Four-wave mixing dynamics of a strongly coupled quantum-dot–microcavity system driven by up to 20 photons, Phys. Rev. B **101**, 245301 (2020).

[147] M. Khanbekyan, L. Knöll, D.-G. Welsch, A. A. Semenov, and W. Vogel QED of lossy cavities: Operator and quantum-state input-output relations, Phys. Rev. A **72**, 053813 (2005).

[148] M. G. Raymer and C. J. McKinstrie, Quantum input-output theory for optical cavities with arbitrary coupling strength: Application to two-photon wave-packet shaping, Phys. Rev. A **88**, 043819 (2013).

[149] S. Xu and S. Fan, Input-output formalism for few-photon transport: A systematic treatment beyond two photons, Phys. Rev. A **91**, 043845 (2015).

[150] A. H. Kiilerich and K. Mølmer, Input-Output Theory with Quantum Pulses, Phys. Rev. Lett. **123**, 123604 (2019).

[151] R. Achilles and A. Bonfiglioli, The early proofs of the theorem of Campbell, Baker, Hausdorff, and Dynkin, Arch. Hist. Exact Sci. **66**, 295 (2012).

[152] T. Yajima and Y. Taira, Spatial Optical Parametric Coupling of Picosecond Light Pulses and Transverse Relaxation Effect in Resonant Media, J. Phys. Soc. Jpn. **47**, 1620 (1979).

[153] M. Lindberg, R. Binder, and S. W. Koch, Theory of the semiconductor photon echo, Phys. Rev. A **45**, 1865 (1992).

[154] D. Wigger, Q. Mermillod, T. Jakubczyk, F. Fras, S. Le-Denmat, D. E. Reiter, S. Höfling, M. Kamp, G. Nogues, C. Schneider, T. Kuhn, and J. Kasprzak, Exploring coherence of individual excitons in InAs quantum dots embedded in natural photonic defects: Influence of the excitation intensity, Phys. Rev. B **96**, 165311 (2017).

[155] M. Koch, J. Shah, and T. Meier, Coupled absorber-cavity system: Observation of a characteristic nonlinear response, Phys. Rev. B **57**, R2049(R) (1998).

[156] M. Kira and S. W. Koch, Cluster-expansion representation in quantum optics, Phys. Rev. A **78**, 022102 (2008).

[157] S. Schumacher, J. Förstner, A. Zrenner, M. Florian, C. Gies, P. Gartner, and F. Jahnke, Cavity-assisted emission of polarization-entangled photons from biexcitons in quantum dots with fine-structure splitting Optics Express **20**, 5335 (2012).

[158] D. Bauch, D. Heinze, J. Förstner, K. D. Jöns, and S. Schumacher, Ultrafast electric control of cavity mediated single-photon and photon-pair generation with semiconductor quantum dots, Phys. Rev. B **104**, 085308 (2021).

Danksagung

An erster Stelle möchte ich mich herzlich bei **Prof. Dr. Torsten Meier** bedanken, da er sein Vertrauen in mich gesetzt hat und mir eine Fast-Track-Promotion zu diesem sehr interessanten und forschungsrelevanten Thema ermöglicht hat. Das ist alles andere als selbstverständlich und ich weiß diese große Chance sehr zu schätzen. Ich möchte mich aber nicht nur für die Chance bedanken, sondern auch für die hervorragende Betreuung während der Promotion. Seine Einschätzungen und Ideen zu physikalischen Problemen aller Art haben mir immer sehr geholfen und oft den Antoß für neue Ansätze gegeben.

Ich möchte mich zudem sehr herzlich bei **J.-Prof. Dr. Polina Sharapova** bedanken. Mit ihr habe ich sehr viele Diskussionen über Quantenoptik geführt und unabhängig von der vorliegenden Problematik hatte sie immer eine gute Idee, was im Prozess meiner Promotion sehr hilfreich war. Eine bessere Betreuung meiner Promotion hätte ich mir gar nicht vorstellen können.

Ich möchte mich bei **Prof. Dr. Olga Tikhonova** und ihrer Arbeitsgruppe für die aufschlussreiche Zusammenarbeit bedanken. Ich danke **apl. Prof. Dr. Ilya Akimov** und seiner Arbeitsgruppe für die angenehme Zusammenarbeit.

Ich möchte mich außerdem bei den Mitgliedern meiner Promotionskomission bedanken.

Ein weiterer Dank gilt allen die mich während der Zeit meiner Promotion direkt oder indirekt unterstützt haben. Hierzu zählen meine langjährigen Bürokollegen, die Mitglieder der Arbeitsgruppen von **Prof. Dr. Torsten Meier**, **J.-Prof. Dr. Polina Sharapova** und **Prof. Dr. Stefan Schumacher** und meine Kommilitonen aus dem Physik-Studium.

Zuletzt danke ich meinen Freunden und meiner Familie.